L-Università ta' Malta
Faculty of Engineering

MASTER OF SCIENCE IN ENGINEERING DISSERTATION

Performance Analysis of Hovering UAVs for Wind Monitoring Applications

LEO SCICLUNA

Supervised by:

PROF. INĠ. TONIO SANT

Co-supervised by:

DR INĠ. ROBERT N. FARRUGIA

A dissertation submitted in partial fulfilment of the requirements for the degree of Master of Science in Engineering

by the

Faculty of Engineering

December 2020

The research work disclosed in this publication is funded by the
ENDEAVOUR Scholarship Scheme (Malta). The scholarship is part-financed
by the European Union – European Social Fund (ESF)
under Operational Programme II – Cohesion Policy 2014-2020,
"Investing in human capital to create more opportunities and promote the wellbeing of society."

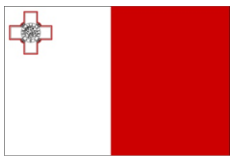

European Union – European Structural and Investment Funds
Operational Programme II – Cohesion Policy 2014-2020
"Investing in human capital to create more opportunities and promote the well-being of society"
Scholarships are part financed by the European Union - European Social Funds (ESF)
Co-financing rate: 80% EU Funds; 20% National Funds

L-Università ta' Malta
Faculty of Engineering

Copyright Notice

1) Copyright in text of this dissertation rests with the Author. Copies (by any process) either in full, or of extracts may be made only in accordance with regulations held by the Library of the University of Malta. Details may be obtained from the Librarian. This page must form part of any such copies made. Further copies (by any process) made in accordance with such instructions may not be made without the permission (in writing) of the Author.

2) Ownership of the right over any original intellectual property which may be contained in or derived from this dissertation is vested in the University of Malta and may not be made available for use by third parties without the written permission of the University, which will prescribe the terms and conditions of any such agreement.

3) Publication rights over the academic and/or research results presented in this dissertation are vested jointly in both the Author and his/her academic Supervisor(s), and unless such rights are explicitly waived in writing, both parties must be listed among the authors in any academic publication that is derived substantially from this work. Furthermore, any other public communication / disclosure of any form that focuses on the project must acknowledge that this work has been carried out by the Author and the Supervisor(s) (named explicitly) through the University of Malta.

Dedicated to my parents for their

inspiration, encouragement, and lifelong support

Abstract

The aim of this research was to analyse the performance of hovering multirotor Unmanned Aerial Vehicles (UAVs) for wind monitoring applications, whilst operating in the inherently highly stochastic nature of open field atmospheric conditions. The two custom built UAVs, a quadcopter and a hexacopter used for the purposes of this research, were each equipped with sensor suites specifically developed for this study. The sensor suites measured and recorded UAV platform and flight parametric data, as well as environmental data, including wind speed and direction by means of an onboard ultrasonic wind sensor. Experimental data were collected during open field hovering flights in different ambient conditions at wind speeds of up to 12 m/s. Data collection flights were conducted at different altitudes above ground and in close proximity to a Light Detection and Ranging (LiDAR) wind measurement unit.

A wind data comparison between the UAV-based measurements and the ground-based LiDAR unit wind measurements indicated that there is a strong correlation in measurements of both wind speed and wind direction across all the altitudes at which UAV operations were conducted.

The study also focused on the effect of increasing wind speed on the power consumption of hovering UAVs, which in turn effects the flight endurance of the systems under study. The impact of the wind conditions, and to a lesser extent the atmospheric air density at the time of UAV operations, were analysed. It was found that, for both tested UAVs, the power demand to maintain stable hovering flight decreased for higher wind speeds due to a higher air mass flow rate passing through the UAV rotors as a result of the higher incident wind speeds. For the hexacopter UAV, following a drop in power demand as the wind speed increased, the power demand stabilized at its minimum value at an incident wind speed of 8.0 m/s, beyond which power demand started to increase with an increase in wind speed. When operating in undisturbed hovering conditions, UAV power demand was observed to increase with a decrease in atmospheric air density, yet the overall effect of air density on the power demand of both test UAVs was found to be marginal.

Acknowledgements

An undertaking of this magnitude would not have been possible without the support of a number of people. Nonetheless I would like to express my appreciation for the support these people have provided during different stages of the research.

I would like to first and foremost wholeheartedly thank my supervisor Prof. Inġ. Tonio Sant and co-supervisor Dr Inġ. Robert N. Farrugia for their unwavering continuous support and timely guidance throughout the full duration of my studies.

I would also like to address my thanks to Dr Charles Galdies from the Institute of Earth Systems at the University of Malta, for loaning an environmental data sensor for the collection of atmospheric variables during the course of the study.

Capt. Charles Pace, Director General, Civil Aviation Directorate at Transport Malta was instrumental in offering the necessary support and guidance in the granting of the necessary permits for the conduction of open field UAV operations in connection with this research.

Thanks are also due to Mr. Jesmond Fenech, Operations Manager at Water Services Corporation, Ċirkewwa Reverse Osmosis Plant, for hosting the LiDAR unit and for granting access to the site for the execution of test flights and data collection flights.

I would also like to thank Mr. Ray Polidano at the Malta Aviation Museum, for making available one of the museum's hangars for the execution of the UAV indoor data collection flights in connection with this research.

Further thanks are also due to Rev. Eucharist Zammit, Archpriest at St. Sebastian Parish in Qormi, for making available the courtyard at St Sebastian's Pastoral Centre for the execution of sheltered UAV data collection flights in connection with this research.

I would also like to thank the ENDEAVOUR Scholarships Scheme Board for the financial support throughout the project. Furthermore, the LiDAR system used in this study was purchased through the European Regional Development Fund (Grant No.: ERDF 335: Solar Research Lab), partially financed by the European Union.

Last but not least, I would also like to say a huge thank you to my family for their support and encouragement, throughout the duration of my studies.

Table of Contents

List of Figures

List of Tables

List of Abbreviations

2D	2-Dimensional
3D	3-Dimensional
AOA	Angle of Attack
AUW	All Up Weight
BLDC	Brushless Direct Current (motor)
CFRP	Carbon Fibre Reinforced Polymer
CIPM	Comité International des Poids et Mesures
CoG	Centre of Gravity
DC	Direct Current
DWD	Deutscher Wetterdienst
ECMWF	European Centre for Medium-Range Weather Forecasts
ESC	Electronic Speed Controller
FAA	Federal Aviation Administration
FM	Figure of Merit
GFS	Global Forecast System
GNSS	Global Navigation Satellite System
GPS	Global Positioning System
GVI	General Visual Inspection
ICON-EU	ICOsahedral Nonhydrostatic-EU
IGRF	International Geomagnetic Reference Field
IMU	Inertial Measurement Unit
LCTF	Liquid Crystal Tuneable Filter
LiDAR	Light Detection and Ranging
LiPo	Lithium Polymer
MAV	Micro Aerial Vehicle
MEMS	Micro-Electromechanical System
NDT	Non-Destructive Testing
NMEA	National Marine Electronics Association
NOAA	National Oceanic and Atmospheric Administration
PMU	Power Management Unit
PV	Photovoltaic

PWM	Pulse Width Modulation
RMSE	Root Mean Square Error
RO	Reverse Osmosis
RPM	Revolutions Per Minute
Rx	Radio Receiver
SAR	Search and Rescue
SBUS	Serial BUS
SPI	Serial Peripheral Interface
SoH	State of Health
TM-CAD	Transport Malta – Civil Aviation Directorate
Tx	Radio Transmitter
UART	Universal Asynchronous Receiver-Transmitter
UAS	Unmanned Aerial System
UAV	Unmanned Aerial Vehicle
VTOL	Vertical Take-off and Landing
WRT	With Reference To
WSC	Water Services Corporation

Nomenclature

A	Rotor Disk Area	(m^2)
A_∞	Slipstream Cross sectional area far downstream of rotor disk	(m^2)
C_D	UAV Drag Coefficient	
C_{d_0}	Rotor blade profile Drag Coefficient	
C_P	Rotor Power Coefficient	
C_{P_i}	UAV Power Model Coefficient for Induced Power term	(kg^2/s^4)
C_{P_0}	UAV Power Model Coefficient for Blade Profile Power term	(m^5/s^3)
C_{P_p}	UAV Power Model Coefficient for Parasitic Power term	(m^2)
C_T	Rotor Thrust Coefficient	
c	Blade chord	(m)
F	Generated Force	(N)
I	Electrical Current	(A)
K	Numerical constant – Translational profile drag	
M_a	Molar mass of dry air	(g/mol)
M_v	Molar mass of water	(g/mol)
$\dot{m}$	Mass flow rate of air through rotor	(kg/s)
N_b	Number of rotor blades	
N_r	Number of rotors powering UAV	
P	Rotor Power	(W)
P_{Diff}	Diagonal Power Differential	(W)
P_i	Rotor Induced Power	(W)
P_{ideal}	Ideal Rotor Induced Power	(W)
P_0	Blade Profile Power	(W)
P_p	Parasitic Power	(W)
p	Atmospheric Pressure	(Pa)
Q	Output Torque of Electrical motor	(N m)
R	Molar Gas Constant	(J/mol K)
RH	Relative Humidity	(%)
r	Rotor radius	(m)
S	Surface area of rotor control volume	(m^2)

S_{ref}	Reference Area for the calculation of parasitic power	(m^2)
T	Rotor Thrust	(N)
T_a	Air Temperature	(K)
t	Air Temperature	(°C)
U	Resultant Velocity at the Rotor disk in translational flight	(m/s)
V	Fluid velocity	(m/s)
V_{bat}	UAV Power pack Voltage	(V)
V_{EO}	Voltage at the ESC Output	(V)
V_{LID}	Wind Speed measured by LiDAR unit	(m/s)
V_{UAV}	Wind Speed measured by UAV mounted wind sensor	(m/s)
V_∞	Wind Speed	(m/s)
v_h	Rotor induced velocity at rotor disk in hover conditions	(m/s)
v_i	Rotor induced velocity at rotor disk	(m/s)
W	Work done	(J)
W_{UAV}	Weight of UAV	(N)
w	Induced velocity far downstream of rotor disk	(m/s)
x_v	Mole fraction of water vapour	
Z	Compressibility Factor for calculation of Air Density	

Greek Symbols

α	Multirotor UAV tilt (inclination) angle	(°)
κ	Induced Power Factor	
η	Motor-ESC Electrical Efficiency	
θ	Wind Direction	(°)
θ_{LID}	Wind Direction measured by LiDAR unit	(°)
θ_{UAV}	Wind Direction measured by UAV mounted wind sensor	(°)
ρ	Density of Air	(kg/m^3)
σ	Rotor Solidity	
Ω	Rotor Angular velocity	(rad/s)
μ	Advance ratio	

1 Introduction

The introduction of this dissertation outlines the main sectors within which Unmanned Aerial Vehicles (UAVs) are deployed, together with the main reasons driving the increasing use of UAVs. The importance of UAV performance and subsequently their flight endurance is also highlighted. The motivation behind the work presented in this dissertation and the associated research objectives are underlined at the end of this Chapter.

People at large have always wondered at the capabilities of birds to apparently overcome the force of gravity and gracefully take to the air. Over the centuries there have been numerous attempts by humans to achieve controlled flight. Documented designs of machinery capable of lifting off date back to the middle ages attributed to Leonardo Da Vinci. Nonetheless, evidence of attempts at building flying machines pre-date the documented designs of Da Vinci [1, 2, 3]. Closer to our times the Wright brothers have been credited with being the first to achieve powered, controlled flight at Kitty Hawk, North Carolina, USA, on 17 December 1903.

1.1 UAV Applications

Over the past decades the use of UAVs and Micro Aerial Vehicles (MAVs) has increased substantially, whilst the areas of deployment of such vehicles have diversified extensively. This is in part due to the rapid rate at which UAV technologies are evolving. Although unmanned aircraft were initially developed by military organizations predominantly for use in the military sector, nowadays these vehicles can be found taking on a civilian role. Amongst the different sectors in which UAVs are being deployed one may find environmental surveying, mapping and monitoring [4], inspections and logistics. UAVs are nowadays also being utilized in the fields of Search and Rescue (SAR) [5], aiding first responders in the aftermath of natural disasters [6]. Work is also underway for the purposes of emergency delivery of life saving goods such as blood products [7] and devices such as life rings for individuals in difficulty at sea [8].

1.1.1 Inspections

The field of UAV-based inspections is rapidly gaining popularity due to a number of advantages that UAV-based technologies offer. UAVs are nowadays also being used

for the General Visual Inspection (GVI) of aircraft, predominantly large transport category aircraft, with some UAVs being specifically developed for such dedicated tasks [9]. Another field in which UAVs are being increasingly deployed is the inspection of civil structures [10, 11], especially structures with challenging accessibility conditions such as bridges and tall buildings [12, 13]. The key advantage of using UAVs for such deployments is that inspections can be carried out whilst keeping such structures operational and open to the public, and concurrently minimizing the exposure of human personnel to the inherent risks associated with carrying out such inspections. Further UAV deployment may be found in the fields of large scale photovoltaic (PV) field inspection [14, 15], and for the purposes of vegetation classification using an onboard Liquid Crystal Tuneable Filter (LCTF) - based hyperspectral imaging system for the latter application [16].

1.1.1.1 Inspection of Wind Turbine Installations

As wind turbine technology develops further it is evident that wind turbine diameters continue increasing in size, consequently the length of the turbine blades increases. Furthermore, wind turbines are nowadays commonly installed offshore, occasionally at a substantial distance from the nearest coast. Leading wind turbine manufacturers are developing wind turbines of a substantial size typically upwards of a 160 m diameter [17] and sometimes reaching a diameter of 220 m [18]. Wind turbine hub heights could attain elevations in excess of 105 m with the blade tips reaching even higher. The operation of such large-scale wind turbines brings about the need of wind resource monitoring as well as wind turbine machinery maintenance.

Wind turbines require regular inspection, especially the wind turbine blades and towers. The frequency of such inspections is dependent on a number of factors including the wind farm site, material of the turbine blades as well as the typical atmospheric conditions at the site of operations.

As UAV deployment becomes more widespread within the civilian sector, their deployment in the wind turbine inspection sector is also on the rise. Research in this specific field is also being undertaken for the purposes of autonomous visual navigation in the wind turbine approach phase and for the proper positioning of the UAV, prior to the commencement of the inspection task [19]. Further research has also

been conducted in the field of algorithm-controlled remote inspection solutions, for maintaining a constant UAV distance from the blade during the inspection task [20].

UAV-based inspections at offshore sites offer great benefits as well as a wide range of associated onboard inspection technologies. Utilizing such technologies for such inspections minimizes substantially the exposure of human personnel to the risks associated with inspection operations at such remote locations and the associated high altitudes. It also permits certain emergency operations to be conducted in unfavourable weather conditions which are normally considered as high-risk for human intervention. Furthermore, UAV platforms may be fitted with an array of Non-Destructive Testing (NDT) inspection technologies, apart from technologies used for visual inspection. UAVs may also be fitted with thermographic scanning technologies, commonly used for the sub-surface inspection of composite structures; materials which are commonly used for wind turbine blades [21].

1.1.2 Logistics and Aerial Displays

More recently UAVs are also being utilized in the logistics sector for the express delivery of commercial goods. DHL had started a UAV delivery service back in 2014, carrying out deliveries over the open sea to the island of Juist in the North Sea [22]. It has continued expanding this service ever since, utilizing an array of different types of aircraft aptly named Parcelcopters.

In October 2019, UPS Forward Flight acquired a Federal Aviation Administration (FAA) full approval to operate a fleet of drones operating beyond the operator's sight as well as at night [23]. Amazon achieved a similar milestone in August 2020 under the name of Prime Air [24], whilst FedEx commenced delivery drone trials with Wing Aviation in October 2019 [25].

Swarms of UAV aircraft are also becoming a popular tool for aerial displays. Such displays have already been put up with a number of UAVs being operated in unison to form various impressions in the night sky. Amongst other locations around the globe, such displays have been organized in Guiyang, Southwest China [26], in Singapore for the 2020 New Year celebrations [27], in Seoul, South Korea [28] and at other mass public gatherings.

1.1.3 Wind Monitoring Applications

The deployment of UAVs for monitoring of atmospheric conditions is not a novelty. Ever since humankind started studying and observing weather developments, free flying and tethered weather balloons have been regularly utilized. It is evident that using balloon technology is fraught with disadvantages. To name a few, untethered weather balloons are uncontrolled devices, very much dependent on the wind conditions at the time of flight and at the different altitudes which the balloon rises to, whilst their payload is also occasionally lost. Tethered versions are difficult to control particularly as the tether becomes longer. Furthermore, weather balloons do not offer the possibility of taking weather measurements at a fixed location for an established duration of time. Meteorological masts and towers are also in common use, although these present a number of difficulties as the tower grows taller.

As with UAV-based inspection operations, the use of UAV technology for wind monitoring operations as well as wind turbine wake profile studies benefits greatly from the advantages that UAV platforms and associated onboard measuring technologies offer. Their advantages are more fully appreciated at remotely located onshore wind farm sites and to a greater extent at offshore wind turbine installations. Unlike weather balloons and more recently fixed wing aircraft, multirotor UAV platforms offer a stable platform for mounting of measuring equipment, whilst being capable of maintaining a stable hover at a fixed point in three-dimensional space. Multirotor UAVs also offer unparalleled flexibility for the purposes of measurement site selection. The measurement location may be at any altitude without restrictions associated with ground-based accessibility or the limitations of a meteorological mast or tower. This is particularly more relevant for carrying out wind monitoring exercises in conjunction with the installation and use of ever larger offshore wind turbines. Furthermore, UAV operations may be easily launched from the relative safety of a ship at sea, with the possibility of conducting such measurement operations even in less-than-ideal weather conditions.

1.2 UAV Platform Versatility

One other key advantage of multirotor UAVs is their relative adaptability to different types of operations quickly. This is of particular interest when different airborne tasks need to be conducted, especially in remote locations such as offshore wind farms. A

multirotor UAV may easily be converted from a configuration for an offshore wind monitoring application to an offshore turbine blade inspection task. This can be easily achieved by replacing its sensor suite payload with an inspection payload suitable for the operation to be undertaken, such as a high-resolution inspection camera. This versatility may be extended to various types of operations, by utilizing modular payloads for the different types of operations.

The uptake of such UAV technologies in the sector of wind farm operations is further driven by the continuous improvement in performance and capabilities of UAVs. Several commercial organizations have already become actively involved and offer such UAV-based inspection operations [29, 30, 31] (see Figure 1.1). Other commercial organizations have also developed atmospheric data sensors specifically intended for mounting onto UAV platforms [32, 33, 34].

1.3 UAV Flight Endurance

Inevitably, UAV deployments at such remote locations are technologically demanding thus raising a number of key issues. One such determining factor is UAV flight endurance as this has a substantial impact on the wind monitoring or inspection operations undertaken. It is also of greater importance especially in cases of wind monitoring operations conducted in less-than-ideal wind conditions. In view of this, the impact of wind conditions on UAV operations needs to be properly investigated.

Figure 1.1: *The Arachnocopter drone from Iberdrola used for the detection of damage on wind turbine blades* [29].

Furthermore, UAV vehicles may be operated either remotely, autonomously, or semi-autonomously. As autonomous technology for UAVs continues to advance and becomes more reliable, UAVs are taking a more autonomous role, especially in SAR scenarios [35]. Autonomous vehicles have the advantage of conducting operations even in conditions of restricted visibility or during the night. In such instances it is imperative that the capabilities and endurance of the UAV can be accurately estimated based on the various real-time conditions at the operations site.

Watkins et al. identified the flight endurance of UAVs as one of the major drawbacks of using UAVs for Atmospheric Wind Measurements [36]. The flight endurance of UAVs is a function of a number of influencing factors, including the overall weight of the UAV, sometimes also referred to as the All Up Weight (AUW), its payload and its power unit status. Other factors affecting UAV endurance include distance to target, hovering duration at the operations site and atmospheric conditions, amongst others. The most common UAV power systems are those powered by fossil fuels or electrical battery power packs. The battery power pack is a popular power unit for UAVs, especially those operated in the civilian sector. A significant characteristic of the battery power pack is its substantial weight. With the current energy densities of Lithium Polymer (LiPo) batteries, the weight of the battery as a fraction of the overall weight of the UAV is substantial. Although the battery weight fraction varies depending on the overall size and weight of the UAV, battery power packs typically account for approximately 20 % of the aircraft weight. In some instances, typically for aircraft below a gross weight of 1 kg, this may rise to as much as 50 % [37]. This results in a notable impact on the flight endurance of the UAV, potentially leading to a trade-off between UAV flight endurance in terms of battery capacity, and the UAV's payload capacity. Although larger capacity batteries may be perceived as increasing a UAV's endurance, their weight increases accordingly, consequently having an adverse impact on the flight endurance of the UAV.

In the quest for increased aircraft flight endurance, research has also been conducted in the field of alternative power technologies such as the use of PVs [38], as well as the use of hybrid power systems to extend flight endurance [39, 40].

1.4 Motivation

As detailed earlier in this chapter the utilization of airborne craft, such as multirotor UAVs, for a myriad of applications including the measurement of wind data, is increasing in popularity for a variety of reasons. Most notably UAV operations are predominantly conducted at locations which are remote and having limited accessibility. The deployment of such mobile platforms for wind data measurements may give rise to measurement uncertainties, mainly due to UAV motion during the data collection window, which could in turn influence the validity of the onboard wind sensor's measured data.

The reliability of wind data measurements is also affected by the duration of the data collection window, which is dependent on the flight endurance of the UAV platform. Maximizing the flight endurance of the UAV platform is therefore very desirable, yet the prevalent wind conditions during data collection operations may influence the propellers' power demand and hence the UAV flight time.

Such operational uncertainties served as a strong motivation for undertaking this research with the aim of evaluating the performance of a multirotor UAV for wind monitoring applications.

1.4.1 Project Objectives

Based on the primary motivations of this research, the main project objectives may be defined as to:

- conduct a literature review about the use of UAVs for:
  - wind measurement applications and
  - the influence of wind conditions on UAV power performance.
- design and develop a reliable multirotor UAV suitable for open field operations in windy conditions with an onboard wind measurement sensor and data logging capabilities.
- design and setup a telemetry system with onboard sensors for the monitoring and logging of UAV flight performance and environmental data.
- evaluate the viability of a UAV-mounted wind measurement sensor as an accurate means of wind measurement by comparing measurements against

those obtained from a ground-based Light Detection and Ranging (LiDAR) wind measurement system.

- analyse the influence of open field wind conditions on the performance of multirotor UAVs, with a particular focus on the power demand.

1.5 Research and Dissertation Outline

A methodical approach was utilized for conducting the research being documented in this dissertation. The workflow of the various stages is being presented in Figure 1.2.

The first stage of the research involved a detailed review of the literature available in order to establish the level of development in the sector, as well as identify the main knowledge gaps. The development phase was characterized by the design, development, assembly and flight testing of the prototype UAVs. This stage was followed by a series of flights for data collection purposes under different environmental conditions, namely in the open field, indoors and in sheltered locations as outlined in Figure 1.2. The next stage of the project was characterized by the

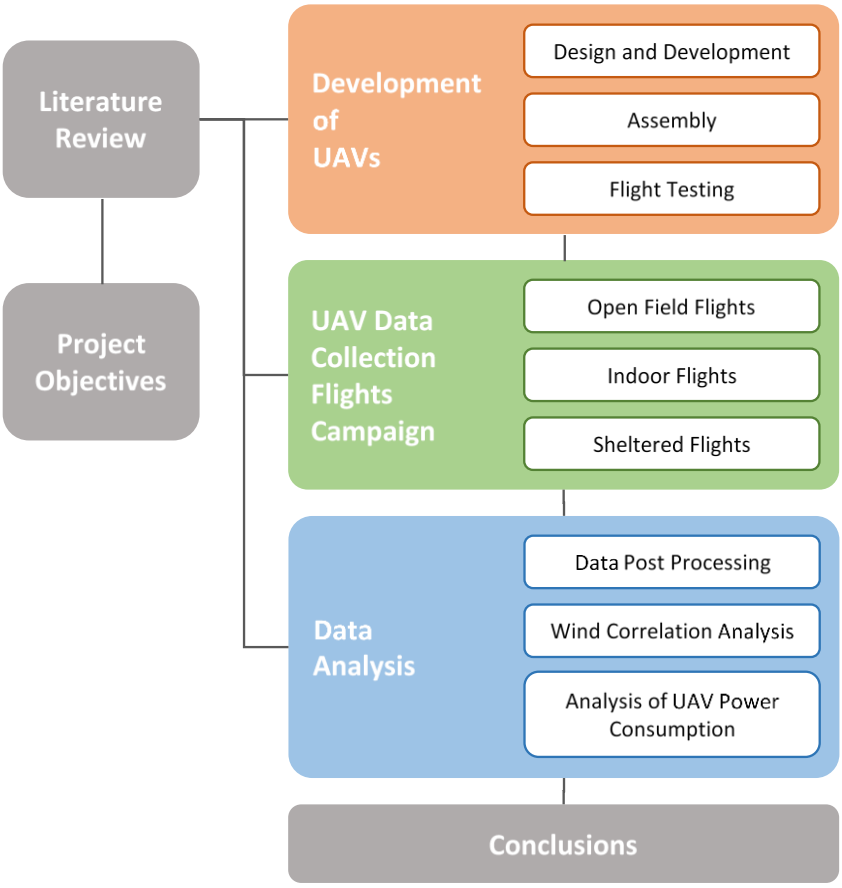

Figure 1.2: *Workflow organization of the different stages of the research project.*

analysis of the collected measurement data, which involved the data post-processing, a wind correlation analysis and a UAV power consumption analysis. The final stage of this research project involved a discussion of the findings and the drawing of conclusions based on the results obtained following the respective analyses.

1.5.1 Dissertation Overview

The first chapter of the dissertation introduced the development of drones over the past decades and the transition from predominantly military applications to a wide range of civilian deployments. This will now be followed by a general literature overview in Chapter 2 of the research conducted to date in the field.

Chapter 3 addresses the theoretical background of the aerodynamic operation of a multirotor UAV based on the work carried out by the scientific community in the past. A detailed description of the design and development process of the multirotor UAVs used in this current research is presented in Chapter 4. This is followed by Chapter 5 which details the methodology used to maximize the validity of the data gathered, whilst maintaining the highest levels of safety and mitigating any risks involved in such research operations.

Chapter 6 focuses on the analysis of the collected measurement data and includes a compilation of the results drawn from this analysis. A discussion based on the interpretation of the obtained results follows in Chapter 7.

In Chapter 8, the main conclusions drawn from this research have been outlined. This chapter also includes a number of areas which have been identified as beneficial to the field and considered suitable for potential further research.

2 Literature Review

Throughout the duration of the project, a review of the available literature was conducted to remain abreast of the latest developments and work being conducted in the field of UAV technologies. This chapter presents a compilation of the main works carried out predominantly in the field of multirotor UAVs, with a particular focus on their deployment for atmospheric and wind monitoring applications. The main topics discussed are UAV-based to ground-based wind data correlation studies, wind data estimation studies based on UAV parametric data and work on power consumption and estimation of the endurance of UAVs. The chapter concludes with the presentation of some work on UAV controllability.

As interest in the use of UAVs across a wide range of applications increases, it is evident that more research into the factors affecting UAV technologies is necessary. Over recent years, work on the development of UAVs for civilian applications has moved from the hobbyists' realm into the consumer and commercial realm, with the standard quadcopter platform powered by a battery power pack emerging as the most popular UAV option for civilian deployment. Consequently, research on UAV technologies is catching up and work related to the use of quadcopter UAVs was found to be on the rise. Unsurprisingly, work on quadcopter UAVs is more common than hexacopter UAVs, potentially because quadcopters come with a lower price tag and are therefore substantially more popular. Nonetheless, throughout the duration of this study, one observes that the popularity of the hexacopter UAV has been gaining ground at a substantial rate. Potentially, this is driven by the relative advantages of a hexacopter UAV; predominantly its inherent stability and basic rotor redundancy, together with a concurrent drop in the purchase price of a hexacopter UAV.

2.1 UAV-based Wind Field Measurements

The use of UAVs for atmospheric data measurements and wind sensing is an area of active research. Studies on the use of fixed wing UAVs for such purposes have already been conducted in the past [41, 42]. Main drivers for the utilization of UAVs for such measurements are the advantages that UAV platforms offer when compared to the impracticalities and limitations of other current meteorological vehicles in use, such as balloon-based measurement systems. Wolf et al. explored different methods for

obtaining wind data, including the use of onboard anemometers and UAV parameters for wind estimation purposes [43]. De Boisblanc et al. embarked on the development of a dedicated hexacopter UAV design purposely built for the collection of atmospheric flow data [44]. Further work on the hexacopter project was carried out with the aim of developing a system which is pre-programmable and autonomous [45].

Other studies conducted by Yeo et al. [46] and [47], utilized onboard pressure probes for the purposes of airflow measurements along each of a quadcopter's fixed axes. The objective of the work detailed in these studies was for estimating the lateral and vertical wind speeds for the purposes of the development of disturbance tolerant flight control strategies, for UAVs operating in external airflows.

Marino et al. studied the viability of utilizing quadcopter UAVs for the measurement of atmospheric flow measurements [48]. In this study, the possibility of using such vehicles for wind data sensing around tall buildings was examined. After extensive wind tunnel testing for studying the power consumption differential between the fore and aft motor pairs, they concluded that an accurate mapping is only possible over a limited region of the measurement space. They also identified that when UAVs operate on the windward side of a building, UAVs may also benefit from the wind generated updrafts resulting in an improvement in UAVs' endurance.

Prudden et al. [49] carried out a flow mapping study using smoke flow visualization and multi-hole pressure probes in a wind tunnel using a quadcopter UAV. The study replicated a UAV in steady state hover and forward flight conditions. It was established that an onboard wind sensor would need to be mounted at a distance of more than seven rotor radii forward of the UAV centre hub. This was necessary for the wind sensor measurements to remain unaffected by the rotors' induced flow. In a subsequent study, Prudden et al. demonstrated that measurements of mean wind velocity as well as turbulence intensity conducted from an airborne platform such as a quadcopter using a multi hole pressure probe were feasible [50].

2.1.1 Airborne Sensor Wind Field Measurements

UAV-based wind sensor measurements are a very attractive development in the field of atmospheric wind data collection. Until a number of years ago such data could only be collected using wind measuring devices installed on meteorological masts or towers, or attached to weather balloons. The acceptance by meteorologists of wind

data measured by a UAV mounted wind sensor is dependent on the consistency of such wind data with wind measurements collected using accepted conventional means. A number of studies on the correlation between UAV-based wind measurements and ground-based wind sensor measurements have already been conducted in the past. Some of the studies undertaken are discussed hereunder.

Shimura et al. [51] mounted an ultrasonic anemometer onto a hexacopter UAV platform at a height of 47 cm above the centre hub of the aircraft. The study covered five UAV flights with a range of open field wind speeds of up to 11 m/s. The acquired data were compared with wind readings measured at a frequency of 1 Hz, against a meteorological mast equipped with propeller-vane anemometers installed at heights of 40 m and 55 m above ground. The results obtained were satisfactory with a 0.5 m/s positive wind speed bias and a 9° negative wind direction bias. Shimura et al. attributed the wind speed bias to the rotor-induced airflow. They also concluded that the UAV tilt angle caused by the increase in ambient wind speed does not affect the wind correlation. The study also compares UAV-based wind measurements with two Doppler LiDAR wind data sets measured at sites 4 km and 5 km from the UAV operations site at altitudes ranging from 50 m to 1000 m above ground. The LiDAR locations were on opposite sides of a 900 m volcanic peak. The subsequent correlation indicated that the UAV-based measurements can be used as an estimate for a qualitative wind vector profile, although a number of discrepancies between the UAV-based data set and the LiDAR data sets were predominantly attributed to the location's topography.

Palomaki et al. [52], measured wind data using both a direct method, using an onboard wind sensor, and an indirect method using the UAVs inertial data, in light to moderate wind speeds of up to 5 m/s. The objective of their study was to establish whether a UAV could be used as a replacement for a tethered weather balloon. The direct wind measurements were collected at a frequency of 1 Hz using a hexacopter UAV, with an onboard two-dimensional (2D) sonic anemometer. The sensor was mounted atop a 30 cm pole above the UAV centre hub. The indirect method wind estimates were obtained using a quadcopter UAV. Open field flights were conducted in close proximity to a three-dimensional (3D) sonic anemometer at an altitude of 10 m above ground for the direct method. For the indirect method, open field flights were conducted in the vicinity of three ground-based sonic anemometers at an altitude of

10 m above ground, against which the collected data were eventually compared. After conducting comparisons with an identical mast-mounted anemometer in an indoor environment, the study indicated that the mean wind speed bias for the direct method was of 0.5 m/s, as found in the study by Shimura et al. [51]. It was also established that during open field testing, a further positive wind speed bias of 0.1 m/s was observed, whilst on some occasions the onboard wind sensor overestimated the wind speed by 1 m/s.

Bruschi et al. performed full-scale wind tunnel experiments for a Micro-Electromechanical System (MEMS) based, 2D anemometer mounted at a height of 22 cm, approximately one rotor diameter, above the operating rotors of a quadcopter [53]. Their objective was to investigate the effect of the quadcopter propellers' induced downwash flow on the anemometer response. The resulting measurements indicated that at tunnel wind speeds of below 10 m/s, the measured wind speed was affected by the rotor induced flow such that the onboard anemometer measured a higher wind speed than the tunnel wind speed, as graphically shown in Figure 2.1. On the other hand, the UAV-based wind direction measurement was found to be practically unaffected.

2.1.2 Wind Field Estimation Methods

Work on estimating wind parameters such as wind speed based on a UAV's flight performance is also very much active. The attractiveness of this approach is predominantly due to the fact that it does not require the use of an expensive onboard dedicated wind measurement sensor. Consequently, a smaller, less expensive UAV platform may be utilized due to the reduced AUW of the UAV. Prior to the estimation

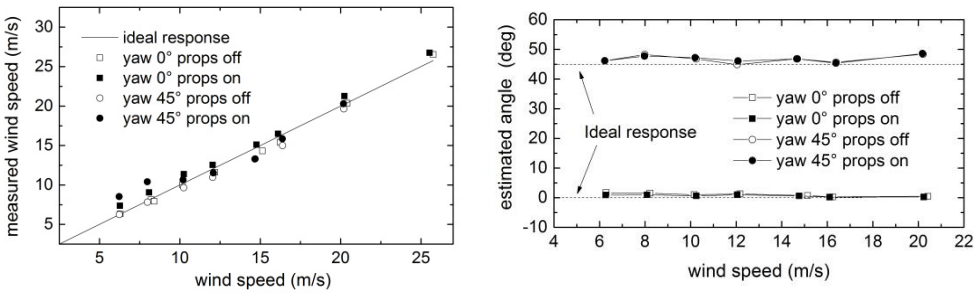

Figure 2.1: *Measured wind speed (left) and wind direction (right) as a function of the reference wind speed for a sensor mounted on a quadcopter during wind tunnel testing by Bruschi et al.* [53].

of wind parameters, it is necessary that a wind response model is developed for the UAV being used for this function. Various such models have been developed to date using different modelling techniques, with the results achieved being of a mixed nature.

Schiano et al. [54], developed a model based on the Newton-Euler approach for the estimation of the wind effect on a quadcopter UAV and eventually corrected for the bespoke impact. It was also established that the drag force acting on the UAV is dependent on the relative wind direction acting on the UAV. This is also evidenced by the wind tunnel tests carried out as part of this study, whereby it was noticed that the lowest drag force acting on the UAV was achieved when the wind direction was incident midway between two adjacent propulsion arms. The wind tunnel tests also indicate that the drag force is also affected by the non-uniform UAV centre hub.

An analytical study for wind estimation from the observed position information of a hovering quadcopter UAV was researched by Qu et al. [55]. The quadcopter response in a windy environment was modelled based on the Newton-Euler approach whilst also analysing the aerodynamic characteristics of a propeller. Based on the developed model, a wind estimating algorithm was used to estimate the wind parameters. Following a simulation-based validation exercise the research established that the wind speed and wind direction estimation obtained were acceptable.

Song et al. [56], focused on the development of a correction method to be used for quadcopter inclination-angle measurement-based wind estimation. The work was intended to improve wind data estimated from the measurements of a quadcopter's Inertial Measurement Unit (IMU) by applying an acceleration correction method. The simulation-based research found that the applied correction method was effective in improving the accuracy of the estimated wind data.

2.1.2.1 Open Field Experimentally Validated Wind Field Estimation

Although some wind estimation studies have been validated by means of simulation runs, a number of other wind estimation studies have been experimentally validated. A portion of these have been validated in the open field and their accuracy has been compared with concurrent data from conventional wind measuring devices.

Gonzalez-Rocha et al. focused on two aircraft motion models, namely a kinematic particle model and a dynamic particle model, to establish wind parameters using a model-based wind estimation [57]. As part of this study, wind tunnel tests were conducted to characterize the aerodynamic forces and moments acting on the UAV's propeller. The UAV was also flown at steady speeds at constant altitude in near still atmospheric conditions to develop an azimuthal model for the tilt angle response and quadcopter drag parameters for various lateral airflows caused by the translational movement. The model-based wind estimation for the quadcopter vehicle used in the study was eventually validated by comparison to a mast mounted 3D ultrasonic wind sensor and a propeller sensor. It was established that when the wind speed varied slowly the wind speed estimation matched, but significant disagreement was found when the wind speed varied abruptly, concluding that the models did not provide for an accurate wind speed estimate.

Subsequent studies by Gonzalez-Rocha et al. using a rigid body model established that wind velocity model-based estimates from quadcopter motion may also be obtained for steady ascent flight speeds of up to 2 m/s [58, 59]. However, it was highlighted that the accuracy of the model-based wind estimates is highly dependent on the motion model accuracy.

A drag-force enhanced quadcopter model wind estimation study was conducted by Sikkel et al. [60]. During wind tunnel experiments to study the accuracy of the wind estimation, it was found that the standard deviation of the wind speed estimate was considerable, and this increased as speed increased. The authors attributed this result to the performance of a low-cost IMU operating in the presence of strong vibrations.

Neumann et al. also worked on wind estimation techniques based on UAV measurement data from the UAV's onboard sensors [61]. The proposed wind estimation technique used for a UAV in translational flight was based on the wind triangle method. A second approach using a UAV's pitch and roll angles was used for wind estimation purposes for a UAV in a stable hover. The drag coefficient for the quadcopter used in the study was established during wind tunnel tests. Similar to the findings in the study by Schiano et al. [54], it was found that the drag coefficient changes as the UAV yaw angle changes, although for the quadcopter used in this study it was established that the variations were negligible. The estimation techniques were

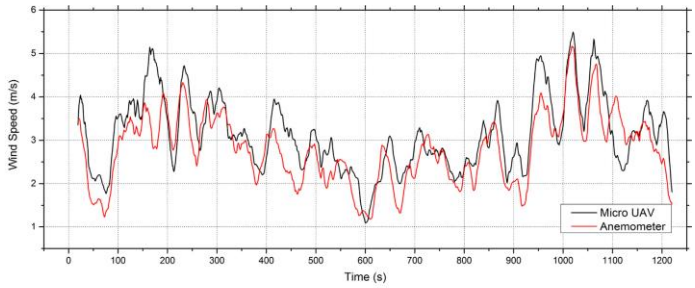

(a) Wind speed

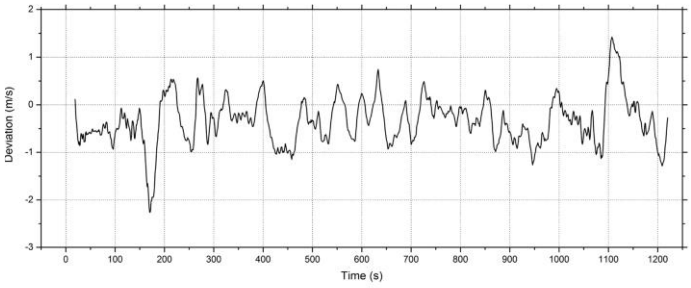

(b) Deviation of the wind speed

Figure 2.2: *Validation of (a) the wind speed estimation and (b) the respective deviations of the mast mounted anemometer to the microUAV estimate, based on data averaged over the last 20 s using a sliding window* [61].

then subsequently validated in the open field against a mast-mounted 3D ultrasonic anemometer, in wind speeds of up to 6 m/s. The results for 20 s moving average wind data for the UAV in a stable hover, reproduced in Figure 2.2 and Figure 2.3, resulted in a wind speed root mean square error (RMSE) of 0.60 m/s and wind direction RMSE of 14.02°. The authors concluded that these results were in general a good match.

Wang et al. carried out a wind estimation study based on the extended state observer method utilizing the aircraft's acceleration and position [62]. To establish the relevant UAV specific parameters necessary to accurately estimate the relevant wind parameters, experiments were performed in a windless indoor environment. The wind estimation technique was validated through a series of simulations and indoor flight tests using a modified industrial fan to generate the required airflow. Based on the results obtained during the validation tests, the authors concluded that the wind estimation technique used generally satisfies the requirements for environmental monitoring.

Tomić et al. used two complementary methods for wind field estimation [63]. They proposed that the horizontal wind velocity may be estimated from the external wrench

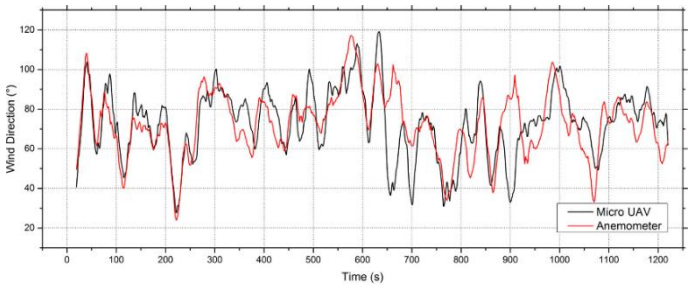

(a) Wind direction

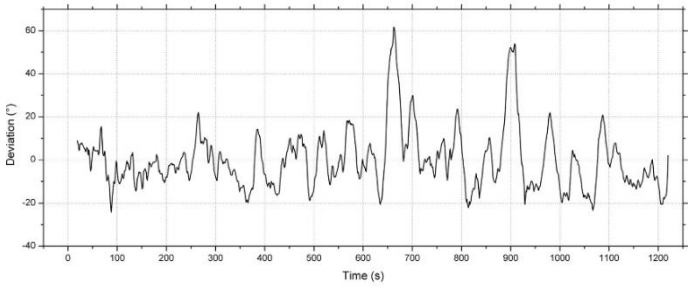

(b) Deviation of the wind direction

Figure 2.3: *Validation of (a) the wind direction estimation and (b) the respective deviations of the mast mounted anemometer to the microUAV estimate, based on data averaged over the last 20 s using a sliding window* [61].

model. Based on this estimation the aerodynamic power model may be used to establish the vertical wind speed component. The models that were developed were eventually validated in wind tunnel experiments using a coaxial hexacopter, concluding that the results obtained were of good accuracy.

The estimation of wind parameters based on UAV motion parameters is a very interesting and innovative approach. The technique benefits from the advantage of not requiring a dedicated onboard wind sensor, as highlighted by most of the studies discussed in this section. Nonetheless, the wind estimates obtained are highly dependent on the accuracy of the deployed UAVs' motion models, for all possible operating circumstances. This implies that any changes to the vehicle itself, such as during maintenance or repairs and which are not subsequently updated in the motion model, potentially have an adverse effect on the accuracy of the estimated wind measurements.

Furthermore, as highlighted in some of the above studies, such wind estimation techniques based on IMU data, many times require the experimental determination of a number of parameters to properly match the wind parameters to the wind-induced

UAV behaviour. Such calibration procedures, or algorithm learning as they are sometimes referred to, are typically carried out in a wind tunnel, to establish the relevant parameters, most notably the drag coefficient of the vehicle to be utilized. It should also be observed that for multirotor UAVs as the aircraft yaws, the respective aerodynamic profile changes, affecting the respective drag coefficient, as highlighted by a number of the above studies. It therefore transpires that the drag coefficient for such vehicles is dependent on the relative angle of the incident airflow.

When comparing the above studies to the research subsequently detailed in this dissertation, it is evident that there are a substantial number of parameters that have an effect on such research. A number of characteristics of the research carried out as part of this project may be found in one or another of the studies outlined. Nonetheless, to the author's knowledge these were not concurrently present in any research done to date. The conditions under which this project was conducted may be summarized as an analysis of UAV-based ultrasonic wind measurements, covering a wind speed range of up to 12 m/s. These measurements were collected in open field conditions and in close proximity to a dedicated LiDAR wind measurement unit at a range of altitudes between 40 m and 100 m above the LiDAR unit's reference window.

2.2 UAV Flight Endurance

The extended endurance of UAVs is a desirable characteristic of any UAV deployed across a wide range of applications. It therefore transpires that reliably estimating the flight endurance of UAVs enhances the efficient and effective deployment of such aircraft. Endurance estimates are especially desirable when operating such vehicles in non-ideal ambient conditions. Open field operating conditions, including atmospheric wind conditions, are characteristically highly stochastic in nature, rendering the accurate prediction of a UAV's energy consumption and flight endurance, substantially challenging. For an accurate estimate of the UAV endurance, it is therefore vital to properly understand the demands placed on the UAV system by the conditions within which the UAV is operating. The lack of such proper understanding proves to be a major drawback for UAV operations, hindering the deployment of UAVs and MAVs in more demanding operations.

Naturally, there is a very strong relationship between UAV endurance and its power consumption. A number of studies addressing overall flight endurance focus primarily

on the power consumption of a UAV. Some studies also focus on a better understanding of the energy consumed by the propulsion system for the purposes of improving its efficiency, with less attention being afforded to the ambient operating conditions. Research in this area utilizing different approaches includes work on increasing the efficiency of UAVs by using improved aerodynamic designs, the maximization of electrical efficiency [64], as well as the effects of utilizing different power technologies to drive such vehicles.

Studies have also been conducted on non-conventional UAV designs, with one such study investigating the effects of atmospheric turbulence on a fixed wing aircraft [65], whilst another study focused on a quadcopter tilt frame [66]. Work has also been done on the enhancement of UAV endurance by the exploitation of regions of lift on the windward side of a geographical ridge [67].

Novel ways to increase a UAV's flight endurance have also been investigated. One such concept was studied by Abdilla et al. [68], whereby the conventional concept of using a monolithic on-board battery was replaced with the use of multiple smaller batteries which were released by the aircraft once depleted. This concept was also investigated in a study by Chang et al. [69], in which the authors concluded that UAV endurance improvement is achieved over a limited number of battery dumps. It was found that as the number of individual batteries increases, the UAV endurance gain due to reduced AUW was offset by the weight of the increased number of dumping mechanisms installed.

Citroni et al. identified drone movement, weight and incident wind as the three main factors that affect a UAV's power consumption and subsequently the UAV's mission duration [70]. The study proposed a novel in-flight nanoarray energy harvester based on plasmonics nano-antenna technology. Theoretical and simulation results for the harvester model resulted in significant increases in the UAV's mission duration.

Prasetia et al. proposed a mission-based black box model of a hexacopter UAV's energy consumption prediction [71]. The authors concluded that the results obtained are satisfactory, but they also stated that there was a significant error in the prediction model when the UAV operated in windy conditions. This was expected as the model did not cater for situations when the UAV was operating in conditions other than calm weather.

Traub [72], developed relationships to estimate the range and endurance of battery powered aircraft. Although the work seems to have focused on fixed wing aircraft, Traub established that the so-called Peukert effect, may increase the range and endurance of a battery powered aircraft provided that the battery capacity is large with respect to the current drawn. This is attributed to the characteristic of the Peukert effect that the delivered capacity of a battery power pack decreases as the current draw from the battery increases.

Gatti et al. developed a function to estimate the endurance of a six rotor UAV in hovering flight [73]. The development of the analytical function was then validated by numerical simulations and subsequently by a number of test flights. The study focused on estimating the hovering time, thereby indicating that external disturbances typical of open field conditions were not factored in. The authors went on to conclude that validation results for the analytical model were satisfactory, although the study did not specify the conditions under which the test flights were carried out.

In a similar study, Abdilla et al. [74] developed a rotorcraft endurance model for LiPo battery powered aircraft. The study is based on a simple rotorcraft power model based on Momentum Theory, with a constant propulsion system efficiency.

Hwang et al. [75] also developed an iterative numerical estimation method for hovering and steady-level flight conditions. The estimation method is subsequently validated by means of a series of hexacopter flights in good weather conditions. The authors caution that any external effects such as external winds, will impact the estimation technique used and consequently affect the accuracy of the endurance estimate. Nonetheless, their analysis shows that the lowest power demand coincides with a forward wind speed of approximately 6 m/s to 9 m/s, for UAV drag coefficients between 0.4 and 1.4, as shown in Figure 2.5.

2.2.1 Power Consumption Modelling

Studies on UAV power consumption modelling constitute a considerable part of in-flight power consumption studies of UAVs. Two main factors affecting the performance of UAVs in the open field are the wind characteristics and the air temperature, as outlined by Thibbotuwawa et al. [76]. The effect of these two parameters on the energy consumption of UAVs is also highlighted in Figure 2.4. In this study an attempt was made at modelling the power consumption of a UAV in

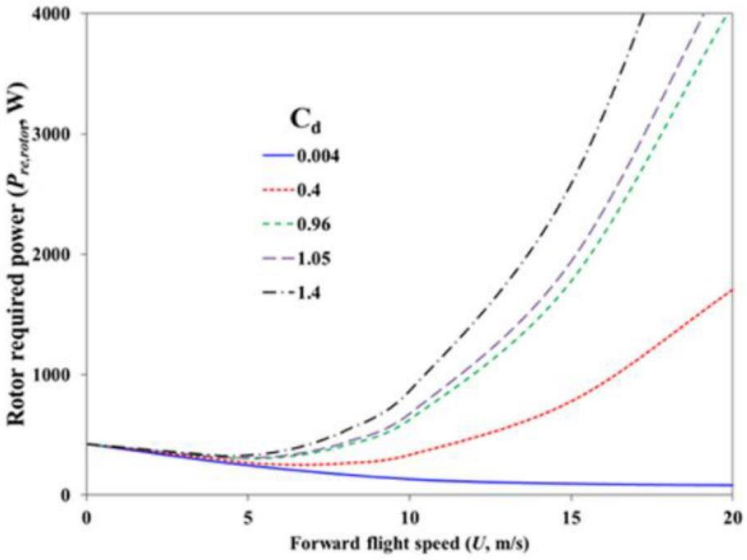

Figure 2.5: *UAV rotor required power* [75].

flight, although the components of the model are limited only to the induced power and the parasite power required to overcome the drag resulting from the UAV's movement relative to the air flow. They also established that as wind speed increases, the benefits of translational lift in forward flight are offset by the increasing power needed to overcome aerodynamic drag.

Abeywickrama et al. developed a comprehensive energy consumption model based on empirical studies of battery performance [77, 78]. For the compiling of a comprehensive energy model, the study considered the different phases of flight for a quadcopter UAV, as well as the impact of the operational conditions and the various mission specific requirements. Although it is generally accepted that the energy consumption for a hovering UAV is altitude independent (assuming constant air

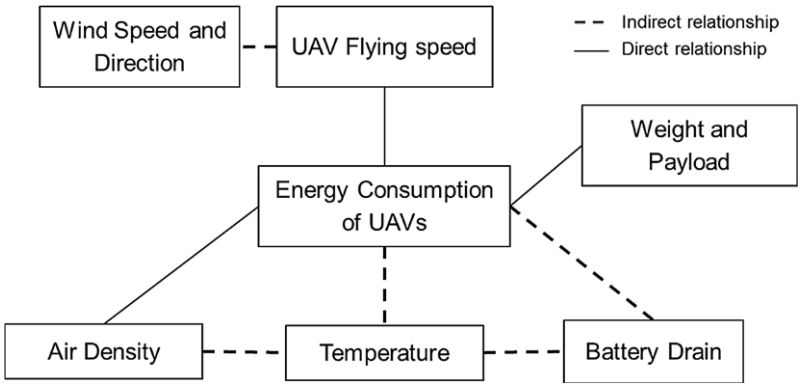

Figure 2.4: *Factors that affect energy consumption of UAVs* [76].

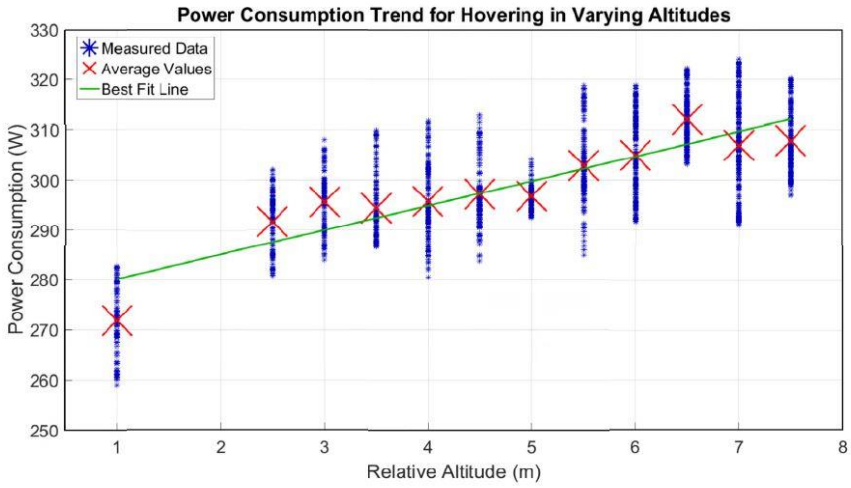

Figure 2.6: *UAV power consumption for hovering at different altitudes* [77].

density), the hover model portion takes into account the relative hovering height [77]. The authors acknowledge that the hovering power consumption should remain constant irrespective of the hovering altitude, whilst assuming that the air density remains constant over the different hovering altitudes. Nonetheless, the authors cite *'UAV efforts in retaining stability against the changing environmental conditions with the altitude'*, as a reason for the increase in power consumption as the altitude increases. Another contributing factor towards this increase in hovering power could also be the diminishing 'ground effect' as a result of the increasing altitude of the UAV with respect to the ground. The data points shown in Figure 2.6, also seem to indicate that as the altitude increases the relationship starts to flatten out as the altitude at hover increases beyond the zone affected by ground proximity.

The authors' study of the wind impact was limited to two flights operated on the same day with the same wind conditions, without considering the effects of humidity and thermal factors. Nonetheless they identified that when the UAV flew into a headwind it consumed considerably less power than when it flew in tailwind conditions, which they attributed to translational lift.

Liu et al. [79] also developed a power consumption model. The model is split into three main power components, namely the induced power, profile power and parasite power. During the experimental phase of this study using an IRIS+ quadcopter UAV, it was established from the experimental data that the power consumption decreases marginally as the relative airspeed increases up to 10 m/s, at which point the power

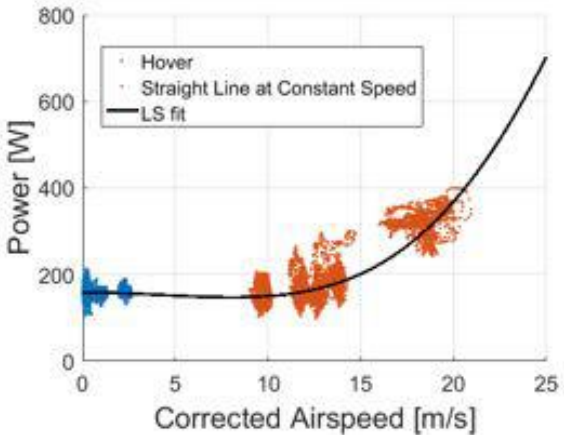

Figure 2.7: *Power consumption for IRIS+ quadcopter* [79].

consumption increases at a relatively steep gradient. From the graph reproduced in Figure 2.7, the lowest power consumption seems to occur at a relative airspeed of approximately 8 m/s. It should be observed that the experimental data collected are not continuous across the full range of airspeeds and one can identify a few gaps especially in the 3 m/s to 8 m/s airspeed range.

2.3 Multirotor Controllability

Dongjie et al. [80] established the level of controllability of various multirotor configurations with evenly distributed and coplanar rotors. In this study it was established that the degree of controllability of a multirotor in hover with all rotors operational increases as the number of rotors increases from four to six to eight. In their work they also established the controllability of different multirotors when they experienced rotor failures. It is considered that for a multirotor to be under full control, the operator would have control over the pitch, roll and yaw of the aircraft. When a quadcopter experiences a motor failure, the UAV is uncontrollable as all of the pitch, roll and yaw channels become uncontrollable, making it impossible to execute a safe landing. In the case of a hexacopter, when the UAV experiences a motor failure, the yaw channel becomes uncontrollable, but the pitch and roll channels remain controllable. Potentially this indicates that the UAV will enter a spin around its vertical axis. Nevertheless, as was concluded in the study, the UAV may still execute a safe landing. The study also establishes that a hexacopter can potentially execute a safe landing even in the eventuality of two motor failures, as long as the motors are on

adjacent propulsion arms and the total thrust capability of the remaining operational rotors is larger than the AUW of the multirotor.

Whilst acknowledging the loss of controllability of the yaw axis in the event of a rotor failure on a hexacopter UAV, recent studies by Pose et al. [81, 82] propose a reconfiguration of the remaining operational rotors to regain control and recover. The experimental setup used consists of a hexacopter with its rotors set permanently tilted towards the UAV centre hub. In case of a rotor failure, control is restored by reconfiguring one rotor to also tilt tangentially, thereby providing the necessary torque correction and hence restoring yaw control.

2.4 Conclusions

The use of the multirotor as a wind monitoring platform is evident from the diverse number of related studies encountered during the review exercise. Research has been conducted in the further development of such platforms as well as on the reliability of the measurements obtained using multirotor UAVs. Below is a list of key points identified during the review of the available literature:

1. The majority of these studies used data measured by conventional wind sensors mounted on meteorological masts in close proximity to the test site as a reference. One particular study compared data to LiDAR units located at a substantial distance from the test site.
2. Ultrasonic wind sensors emerge as the preferred sensor type for wind monitoring applications using multirotor UAVs as a measurement platform.
3. Research indicates that wind speed measurements acquired by UAV-mounted wind sensors are commonly logged at a frequency of 1 Hz. In general, such measurements have a positive wind speed bias in the range of 0.5 m/s to 1 m/s. As for the measured wind direction, studies seemingly indicate that such readings remain relatively unaffected.
4. Wind estimation techniques based on UAV parametric data, depend heavily on the accuracy of the estimation model and usually require calibration procedures to establish UAV-dependent wind response parameters. Such procedures are normally carried out in wind tunnel environments.

5. For multirotor UAVs the acting drag force is dependent on the respective incident direction of the relative wind due to the non-uniform aerodynamic profile of the aircraft.
6. UAV flight endurance models address the different phases of flight, namely take-off, climb, hovering flight, translational flight, descent and landing independently.
7. A number of UAV flight endurance estimation models have been developed for UAV flights in ideal weather conditions, with the majority of studies cautioning about the impact on the accuracy of such models due to open field flight conditions.

The literature available to date spans a wide variety of UAV fields relevant to wind monitoring applications and UAV flight endurance, with a substantial number of such studies being rather application specific. Nonetheless due to the large number of distinct operating scenarios, some areas have been afforded less attention than others. Two areas which apparently warrant further research are:

1. UAV based wind measurement correlation against a dedicated LiDAR wind measurement unit for different measuring altitudes above the ground, and
2. Flight performance of UAVs at different altitudes based on extensive open field empirical data. It is understandable that such data are very much UAV model dependent. Nonetheless, such data may be very useful in validating both existing and future UAV models, thus improving the overall reliability of models for performance prediction.

3 Rotor Aircraft Theory

This chapter introduces the theoretical background that governs the operation of a multirotor. It discusses the equilibrium of forces to which the UAV is subjected during hovering flight, followed by the Momentum Theory used to develop an expression for the Thrust generated and Power consumed by a UAV in hovering flight. Typical approximations used in practice for these bespoke parameters are also highlighted. This is followed by the proposal of approximation models for the rotor thrust and induced power at wind speeds close to the rotor-induced velocity. Towards the end of this chapter an equation for calculating the density of air is presented, together with a suitable approximation of this parameter for use in this study.

Aircraft operate under various aerodynamic conditions. The interaction of an aircraft with the different conditions it operates in is very much dependent on the type, shape and configuration of the aircraft itself. One such type of aircraft is the multirotor vertical-axis UAV, which has been developed in a range of configurations. The configuration used during this study is the coplanar symmetric configuration, whereby the coplanar rotors are mounted at the end of propulsion arms equally spaced around the central multirotor hub. Multirotors are usually not equipped with control surfaces commonly found on other types of aircraft and used to accomplish manoeuvres whilst in the air. Instead, multirotors accomplish all the desired movements by adjusting the individually controlled rotor speeds at the end of each propulsion arm.

The three predominant operating scenarios of Vertical Take-off and Landing (VTOL) multirotor aircraft with a quasi-symmetrical configuration are:

1. Hovering Flight,
2. Axial Climb or Descent – Flight under the influence of an External Axial Airflow, and
3. Translational Flight – Flight under the influence of an External Coplanar Airflow.

3.1 Forces acting on a Multirotor UAV in Flight

The rotors of a multirotor operating in a state of hover with no external disturbances generate a combined thrust equivalent to the overall weight of the vehicle. When the

same aircraft operates in hovering conditions in the presence of an external disturbance, typically a lateral wind, the UAV experiences a horizontal force imbalance. This causes the UAV to drift along with the incident wind. The accelerometer within the IMU, forming part of the Flight Controller, detects such lateral movement and adjusts the UAV to tilt into the wind to compensate for the wind disturbance. The tilt angle of the UAV causes the rotors to generate a horizontal component from the thrust generated, in the opposite direction of the incident wind. This component balances out the wind-generated drag force acting on the multirotor aircraft, as graphically demonstrated in Figure 3.1. Thus, when the UAV is hovering in equilibrium in the presence of a lateral wind, the forces acting on the UAV are given by

$$UAV\ Weight = T\cos\alpha \tag{3.1}$$

and

$$Wind\ (Drag)\ Force = T\sin\alpha \tag{3.2}$$

Naturally, in order to maintain a vertical component of lift equivalent to the weight of the aircraft, the multirotor UAV is required to generate more thrust than in the undisturbed hover scenario. Otherwise, the UAV will start losing altitude.

The Flight Controller achieves this UAV attitude via control signals sent to each motor's Electronic Speed Controller (ESC), which adjusts the individual rotor speeds.

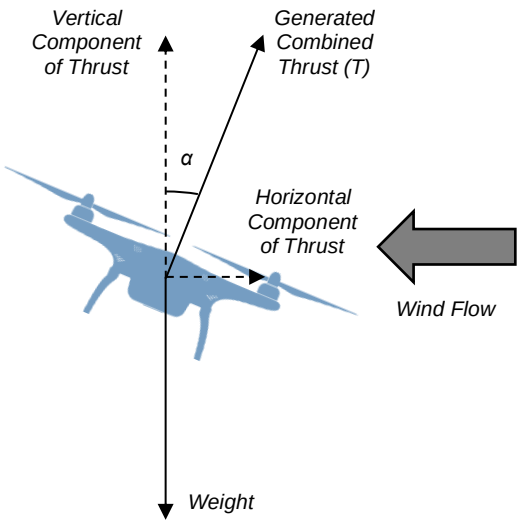

Figure 3.1: *Main forces acting on the multirotor UAV.*

The upwind rotors reduce rotational speed whilst the downwind rotors increase their rotational speed, such that the multirotor UAV tilts into the wind, whilst maintaining a vertical thrust component equal to the multirotor weight and a horizontal thrust component equivalent to the wind force acting on the aircraft.

It should be noted that when a UAV hovers in the presence of such an external coplanar airflow, typically an incident wind, the UAV may be considered as operating under Translational Flight conditions, more commonly referred to as Forward Flight.

It therefore transpires that in the case of a multirotor aircraft the combined thrust generated by the UAV rotors serves two key purposes: (1) it serves to overcome the multirotor's weight, such as in climb, descent and hovering scenarios and (2) it also serves to provide a horizontal propulsive force such as in cases of horizontal flight, or else to counteract lateral external disturbances in order to maintain a fixed stable hovering position with respect to the ground.

3.2 Rotor Aerodynamics

The rotation of the main rotor on a conventional single rotor helicopter generates a torque effect which causes the aircraft to yaw in the opposite direction to that of the main rotor spin. Single main rotor helicopters are equipped with a tail rotor that spins about a horizontal axis and generates thrust to counter the main rotor's induced yaw. When an aircraft is multirotored, the rotors do not all spin in the same direction. In the case of multirotor UAVs with an even number of rotors, the rotors are configured such that there is an equal number of rotors rotating clockwise as there are rotating anticlockwise. Generally, the rotors on multirotor UAVs are configured such that adjacent rotors spin in opposite directions as shown in Figure 3.2 and Figure 3.3, for quadcopter and hexacopter UAVs respectively. This has the effect of neutralizing the yaw effect generated by each individual rotor. Such a setup effectively makes multirotored aircraft Yaw-neutral, hence being capable of operating without the need of a horizontal axis rotor to correct for such rotor induced yaw.

As already outlined, this study focuses predominantly on the performance of multirotored aircraft in hovering flight conditions. Nevertheless, as just highlighted when it is operating in the presence of an incident horizontal wind, the rotor aerodynamics are better represented by the models of a rotor operating in translational

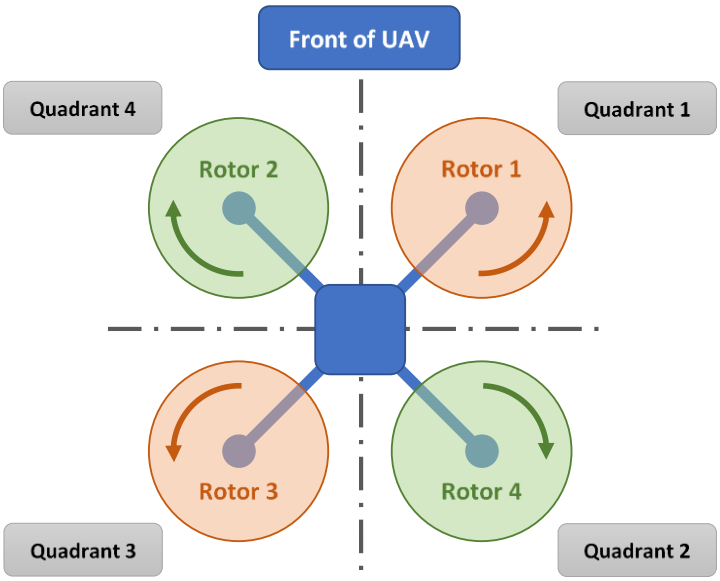

Figure 3.2: *Plan view of a quadcopter with an X-configuration showing the position of each motor in relation to the front (nose) of the aircraft, its respective direction of rotation, and the reference quadrants of the quadcopter UAV.*

flight conditions. In view of this, the analysis described in this chapter focuses on the theoretical background of rotors in hover as well as in translational flight conditions.

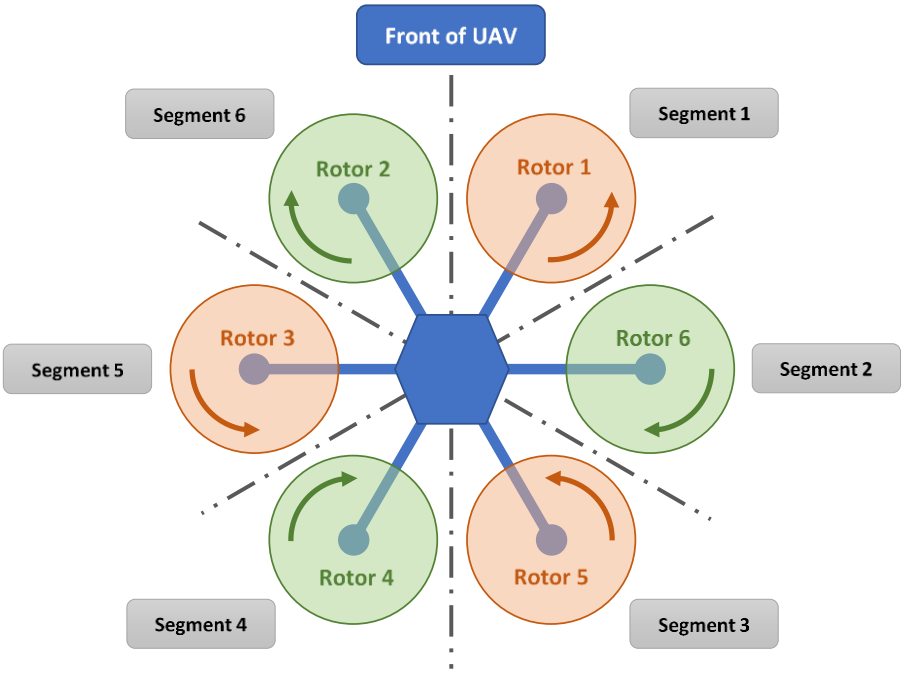

Figure 3.3: *Plan view of a hexacopter with an X-configuration showing the position of each motor in relation to the front (nose) of the aircraft, its respective direction of rotation, and the reference segments of the hexacopter UAV.*

3.2.1 Momentum Theory – Hovering Flight

The mathematical model for the operation of a rotor is developed using the three basic conservation laws, namely those of mass, momentum and energy. This is normally referred to as Momentum Theory and is based on the work carried out by Rankine and Froude who pioneered its development [83].

The theory is developed based on a number of assumptions which have been summarized hereunder:

- The rotor disk is represented by an actuator disk, with an infinite number of blades, implying uniform fluid flow through the area swept by the rotor.
- The airflow through the control volume is quasi-steady, implying that the flow properties at a point remain constant with time.
- The fluid is incompressible and inviscid, meaning that the fluid density is constant and any viscous losses are considered to be negligible.
- The flow of the fluid is one-dimensional meaning that the properties of the fluid change only in the direction normal to the actuator disk, and no rotational velocity or swirl is imparted to the air as it traverses the control volume.

Based on the above assumptions, the mathematical models for the conservation of mass, momentum and energy applied on the control volume shown in Figure 3.4 are expressed below.

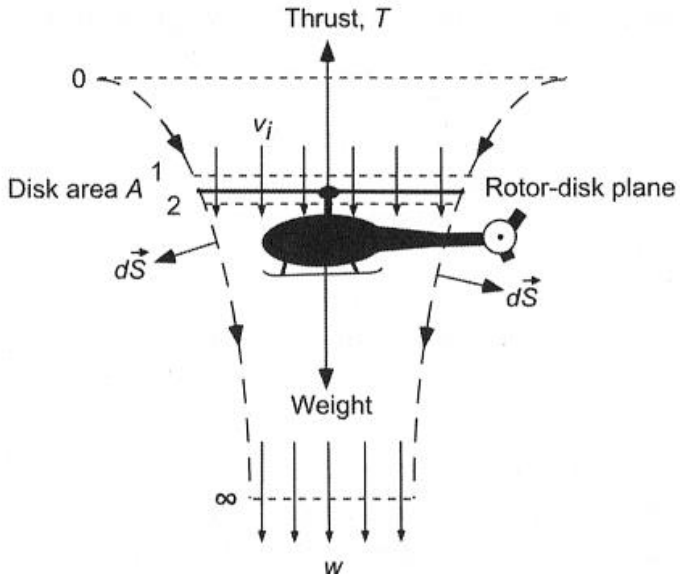

Figure 3.4: *Flow model for momentum theory analysis of a rotor in hovering flight* [83].

Conservation of Mass

$$\iint_S \rho\vec{V} \cdot d\vec{S} = 0 \tag{3.3}$$

Conservation of Momentum

$$\vec{F} = \iint_S p d\vec{S} + \iint_S (\rho\vec{V} \cdot d\vec{S})\vec{V} \tag{3.4}$$

Conservation of Energy

$$W = \iint_S \frac{1}{2}(\rho\vec{V} \cdot d\vec{S}) \left|\vec{V}\right|^2 \tag{3.5}$$

Assuming steady state conditions within the boundaries of the control volume shown in Figure 3.4, then

$$\dot{m} = \iint_\infty \rho\vec{V} \cdot d\vec{S} = \iint_2 \rho\vec{V} \cdot d\vec{S} \tag{3.6}$$

Therefore, for 1-D incompressible flow, the mass flow rate can be expressed by

$$\dot{m} = \rho A_\infty w = \rho A_2 v_i = \rho A v_i \tag{3.7}$$

According to Newton's second law of motion, the thrust generated is equal to the net rate-of-change of fluid momentum across the upper and lower boundaries of the control volume. Therefore, the Thrust generated is expressed as

$$-\vec{F} = T = \iint_\infty \rho(\vec{V} \cdot d\vec{S})\vec{V} - \iint_0 \rho(\vec{V} \cdot d\vec{S})\vec{V} \tag{3.8}$$

Since in hovering flight the velocity at the upper bounds of the control volume is considered to be quiescent, the second term in Eq. (3.8) is nil and the thrust expression reduces to

$$T = \iint_\infty \rho(\vec{V} \cdot d\vec{S})\vec{V} = \dot{m}w \tag{3.9}$$

Applying the Principle of Conservation of Energy, the kinetic energy acquired by the fluid as it passes through the control volume is equal to the work done, W, on the fluid per unit time, which can be expressed as

$$W = Tv_i = \iint_{\infty} \frac{1}{2}\left(\rho\vec{V}\cdot d\vec{S}\right)\vec{V}^2 - \iint_{0} \frac{1}{2}\left(\rho\vec{V}\cdot d\vec{S}\right)\vec{V}^2 \tag{3.10}$$

Once again, since in the hovering state the velocity at the upper bounds of the control volume is considered to be quiescent, the second term in Eq. (3.10) is nil and the expression reduces to

$$Tv_i = \iint_{\infty} \frac{1}{2}\left(\rho\vec{V}\cdot d\vec{S}\right)\vec{V}^2 = \frac{1}{2}\dot{m}w^2 \tag{3.11}$$

Combining Eqs. (3.9) and (3.11), the induced velocity, v_i, may be expressed by

$$v_i = \frac{1}{2}w \tag{3.12}$$

Assuming incompressible flow, whilst applying the Principle of Conservation of Mass between the rotor disk and the lower bound of the control volume, the mass flow rate may be expressed as

$$\dot{m} = \rho A_{\infty} w = \rho A_{\infty} 2v_i = 2\rho A_{\infty} v_i \tag{3.13}$$

From this expression the ratio of the cross-sectional area of the control volume as the rotor wake fully develops below the rotor, and the rotor disk area, is given by

$$\frac{A_{\infty}}{A} = \frac{1}{2} \tag{3.14}$$

3.2.1.1 Induced Velocity and Rotor Power

From Eq. (3.9), the Thrust generated can be expressed in terms of the induced velocity at the rotor disk by the following expression:

$$T = \dot{m}w = \dot{m}(2v_i) = 2(\rho A v_i)v_i = 2\rho A v_i^2 \tag{3.15}$$

Rearranging the above expression, v_i, the induced velocity at the rotor disk, can be expressed in terms of the Thrust generated as follows:

$$v_h \equiv v_i = \sqrt{\frac{T}{2\rho A}} = \sqrt{\left(\frac{T}{A}\right)\frac{1}{2\rho}} \tag{3.16}$$

Therefore, the ideal power required to hover is given by

$$P_{ideal} = Tv_i \equiv Tv_h = T\sqrt{\frac{T}{2\rho A}} = \frac{T^{3/2}}{\sqrt{2\rho A}} \tag{3.17}$$

or by

$$P_{ideal} = Tv_i = \dot{m}v_i^2 = 2(\rho A v_i)v_i^2 = 2\rho A v_i^3 \tag{3.18}$$

It should be emphasized that the simple momentum theory described in section 3.2.1, and used to derive the Thrust and Power for hovering flight does not account for any losses incurred. Blade drag and tip losses, the effect of a finite number of blades on the rotor and variations from the ideal wake contraction are just a few examples of phenomena not accounted for in the theory. The simple momentum theory is therefore modified so that it may better approximate the induced power required to generate the necessary hovering thrust by introducing the term κ, which is the induced power factor. Therefore, induced power according to the modified momentum theory, is given by

$$P_i = \kappa T v_i = \frac{\kappa T^{3/2}}{\sqrt{2\rho A}} \tag{3.19}$$

A typical average value of κ is 1.15 [83].

The expression for the induced power of a rotor as typically derived in literature [83] and quoted in Eq. (3.19), is suitable for single rotor aircraft. It therefore transpired that for the purposes of this study, this expression needed to be extended to include the induced power of all the rotors powering the multirotor. Hence the induced power for a multirotor may be expressed as the sum of the individual induced powers of each of the rotors, and is given by

$$P_i = \sum_{i=1}^{N_r} \frac{\kappa T_i^{3/2}}{\sqrt{2\rho A}} \tag{3.20}$$

where N_r is the number of rotors on the multirotor UAV.

3.2.2 Thrust and Power Coefficients

In rotor aerodynamics literature [83, 84, 85] Thrust and Power as well as a number of other parameters, are expressed in dimensionless form as coefficients. The Thrust coefficient for a rotor is expressed as

$$C_T = \frac{T}{\rho A \Omega^2 r^2} \tag{3.21}$$

and the Power coefficient is expressed as

$$C_P = \frac{P}{\rho A \Omega^3 r^3} \tag{3.22}$$

Therefore, the ideal power coefficient can be expressed in terms of the Thrust coefficient by

$$C_{P_{ideal}} = \frac{C_T^{3/2}}{\sqrt{2}} \tag{3.23}$$

Although rotor literature usually presents expressions in the above dimensionless coefficients, for this particular study it was deemed more appropriate to use the dimensioned power expression, as this is independent of the rotor speeds. Using the dimensionless version would have rendered the expression more complex due to the multiple rotors in use, and potentially increase errors due to the use of an increased numbered of measured variables, which invariably are prone to contain measurement errors and inaccuracies.

3.2.2.1 Rotor Blade Profile Power

All bodies exposed to a relative airflow experience a drag force. As the rotor spins, each blade on the rotor will experience a resistive aerodynamic drag force as it separates the fluid ahead of it. This resistive force is referred to as blade profile drag, and power is expended to overcome it. The power required to overcome blade profile drag when a rotor is operating in undisturbed hovering conditions is given by [83, 84]

$$P_0 = \frac{1}{8}\rho N_b \Omega^3 c C_{d_0} r^4 = \rho A (\Omega r)^3 \left(\frac{\sigma C_{d_0}}{8}\right) \tag{3.24}$$

where σ is the rotor solidity, which is the ratio of blade area to rotor disk area expressed by

$$\sigma = \frac{N_b c r}{A} \tag{3.25}$$

3.2.3 Figure of Merit

The figure of merit (FM) is a standard nondimensional measure of rotor thrust efficiency in hovering flight. It is the ideal power required to generate the thrust required during hover as calculated by Eqs. (3.17) or (3.18) using the simple momentum theory, as a ratio of the actual power consumed to generate the bespoke hovering thrust, such that

$$FM = \frac{Ideal\ Power\ for\ hovering\ thrust}{Actual\ Power\ for\ hovering\ thrust} \tag{3.26}$$

Since the momentum theory used to derive the power required for hovering does not account for any viscous losses, the value of the FM for any rotor is always less than unity. Using the modified momentum theory the FM may also be expressed as

$$FM = \frac{Ideal\ Power}{Induced\ Power + Profile\ Power} = \frac{P_{ideal}}{\kappa P_{ideal} + P_0} \tag{3.27}$$

In practice, typical values for the hovering performance of a rotor are in the range of 0.65 to 0.8, with a value of 0.8 representing a very good rotor performance [83, 84]. As the disk loading of the rotor increases, the FM increases and it should therefore be noted that the FM should only be used as a comparison with other rotors of a similar disk loading, as otherwise the rotor with the highest disk loading tends to exhibit the highest FM [83].

3.2.4 Momentum Theory – Translational Flight

In section 3.2.1 the expressions for the thrust and power for a hovering rotor were derived, using the Momentum Theory for an actuator disk. When a rotor operates in translational flight conditions it will experience an asymmetric flow, which also results in asymmetric thrust generation. This is brought about by the difference in the flow fields over the rotor blade that is advancing into the relative wind, and the rotor blade retreating away from the relative wind. In the case of single rotor aircraft this phenomenon will need to be compensated for as this will generate a roll component on the aircraft. In the case of a multirotor aircraft configured with rotors alternately rotating in opposite directions, the roll effect can be considered to cancel out and will therefore be ignored in the mathematical analysis described.

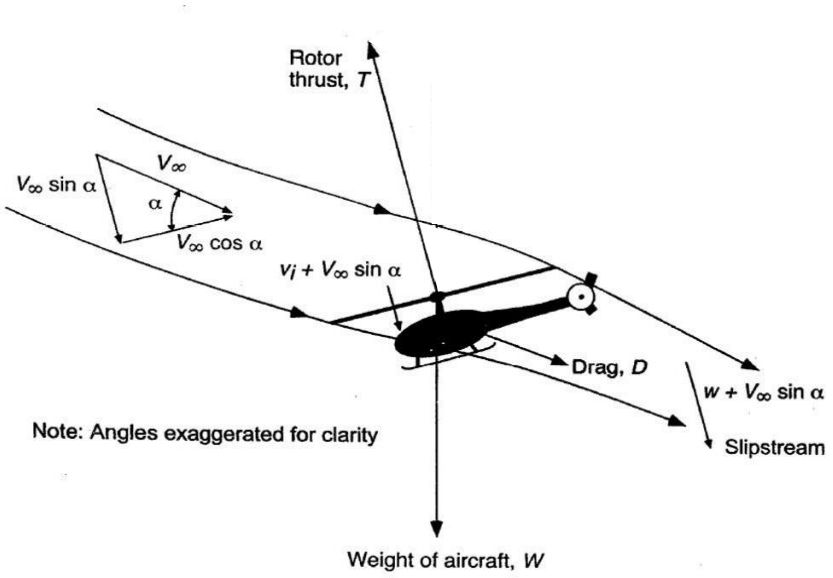

Figure 3.5: *Glauert's flow model for the momentum analysis of a rotor in forward flight* [83].

Due to the asymmetric flow properties, the derivation of the expressions for thrust and power of a rotor in translational flight is inherently more complex. Nevertheless, these can still be derived using simple momentum theory as for a hovering rotor.

The analysis using the Momentum Theory for a rotor in translational flight, as was first proposed by Glauert [83], will now be conducted with respect to an axis normal to the rotor disk. By applying the *Principle of Conservation of Mass* to the control volume in Figure 3.5, the expression for the mass flow rate through the disk is given by

$$\dot{m} = \rho A U \tag{3.28}$$

where U is the resultant velocity at the disk which is given by

$$U = \sqrt{(V_\infty \cos\alpha)^2 + (V_\infty \sin\alpha + v_i)^2} = \sqrt{V_\infty^2 + 2V_\infty v_i \sin\alpha + v_i^2} \tag{3.29}$$

Applying the *Principle of Conservation of Momentum* along the axis of rotation of the rotor

$$T = \dot{m}(w + V_\infty \sin\alpha) - \dot{m}V_\infty \sin\alpha = \dot{m}w \tag{3.30}$$

whilst applying the *Principle of Conservation of Energy*, power may be expressed as

$$P = T(v_i + V_\infty \sin\alpha) = \frac{1}{2}\dot{m}(V_\infty \sin\alpha + w)^2 - \frac{1}{2}\dot{m}V_\infty^2 \sin^2\alpha$$
$$= \frac{1}{2}\dot{m}(2V_\infty w \sin\alpha + w^2) \tag{3.31}$$

Combining Eqs. (3.30) and (3.31), the following relationship is obtained

$$\dot{m}w(v_i + V_\infty \sin\alpha) = \frac{1}{2}\dot{m}(2V_\infty w \sin\alpha + w^2) \tag{3.32}$$

which expands to

$$2wv_i + 2V_\infty w \sin\alpha = 2V_\infty w \sin\alpha + w^2 \tag{3.33}$$

and subsequently reduces to

$$w = 2v_i \tag{3.34}$$

This is equivalent to Eq. (3.12) for the momentum theory in hovering flight, implying that the relationship between the induced velocity at the rotor disk and the air velocity downstream of the rotor disk holds true for both hover and translational flight scenarios.

3.2.4.1 Induced Velocity in Translational Flight

Applying the same reasoning as for Eq. (3.15), the thrust generated can be expressed by the following expression:

$$T = 2\dot{m}v_i = 2\rho A U v_i = 2\rho A v_i \sqrt{V_\infty^2 + 2V_\infty v_i \sin\alpha + v_i^2} \tag{3.35}$$

Rearranging the above expression, v_i, the induced velocity at the rotor disk, may be expressed in terms of the Thrust generated as follows:

$$v_i = \frac{T}{2\rho A U} = \frac{T}{2\rho A\sqrt{V_\infty^2 + 2V_\infty v_i \sin\alpha + v_i^2}} \tag{3.36}$$

When the rotor operates in the hovering flight scenario and $V_\infty = 0$, Eq. (3.35) reduces to

$$T = 2\rho A v_i^2 = 2\rho A v_h^2 \tag{3.37}$$

which is equivalent to Eq. (3.15) which gives the thrust generated under undisturbed hovering conditions.

3.2.4.2 Glauert's High Speed approximation

It is observed that as relative horizontal wind speed increases such that $V_\infty \gg v_i$, the only remaining significant term under the square root in Eq. (3.35) is V_∞^2. Hence, by omitting the otherwise negligible terms under the square root, Eq. (3.35) reduces to

$$T = 2\rho A v_i V_\infty \tag{3.38}$$

This approximation is referred to as *Glauert's high speed approximation*. It therefore transpires that v_i can be approximated by

$$v_i = \frac{T}{2\rho A V_\infty} \tag{3.39}$$

3.2.4.3 Intermediate Speed approximation

When a multirotor operates in a hovering state in the presence of an incident wind, it is not uncommon for the wind speed to be approximately equal to the rotor-induced velocity, $V_\infty \approx v_i$, with the UAV tilt angle α, being minimal. Indeed, during this study, the multirotor UAVs also operated in wind speeds which were approximately equivalent to the rotor induced velocity of the UAV rotors. By its own nature, Glauert's high speed approximation is more accurate at wind speeds substantially larger than the induced velocity. Consequently, as part of this study the author developed a better approximation of the derived mathematical model for operational conditions whereby the wind speed is approximately equal to the rotor-induced velocity. The proposed approximation may be derived by replacing v_i with V_∞ under the square root in Eq. (3.35). The middle term, $2V_\infty v_i \sin\alpha$, under the square root ought to be omitted as this is rendered negligible due to $\sin\alpha$ being negligible. The expression for the rotor thrust then reduces to

$$T = 2\sqrt{2}\rho A v_i V_\infty \tag{3.40}$$

The approximation being proposed in this study will be referred to as the *Intermediate Speed approximation*. Rearranging Eq. (3.40), v_i, the induced velocity at the rotor disk at Intermediate Speed conditions, may be approximated by

$$v_i = \frac{T}{2\sqrt{2}\rho A V_\infty} \tag{3.41}$$

3.2.4.4 Rotor Induced Power Requirements in Translational Flight

In order to calculate the rotor power required in Translational Flight, then

$$P = T(V_\infty \sin\alpha + v_i) = TV_\infty \sin\alpha + Tv_i \tag{3.42}$$

The first term on the right-hand side of Eq. (3.42) is the power required to overcome the drag force exerted on the multirotor by the incident horizontal wind, whilst the second term is the induced power.

Therefore, the ideal induced power required during high speed translational flight may be approximated by

$$P_{ideal} = Tv_i = T \cdot \frac{T}{2\rho A V_\infty} = \frac{T^2}{2\rho A V_\infty} \tag{3.43}$$

or by

$$P_{ideal} = Tv_i = \dot{m}v_i^2 = 2(\rho A U)v_i^2 = 2\rho A v_i^2 V_\infty \tag{3.44}$$

Using the proposed *Intermediate Speed approximation*, the ideal induced power required during intermediate speed translational flight may be approximated by

$$P_{ideal} = Tv_i = T \cdot \frac{T}{2\sqrt{2}\rho A V_\infty} = \frac{T^2}{2\sqrt{2}\rho A V_\infty} \tag{3.45}$$

or

$$P_{ideal} = Tv_i = \dot{m}v_i^2 = 2(\rho A U)v_i^2 = 2\sqrt{2}\rho A v_i^2 V_\infty \tag{3.46}$$

Taking into consideration the induced power factor to compensate for losses not accounted for by the simple momentum theory, the induced power may be better approximated for high speed translational flight by

$$P_i = \kappa T v_i = \frac{\kappa T^2}{2\rho A V_\infty} \tag{3.47}$$

and for intermediate speed translational flight by

$$P_i = \kappa T v_i = \frac{\kappa T^2}{2\sqrt{2}\rho A V_\infty} \tag{3.48}$$

The expression for the induced power of a rotor as typically quoted in literature [83] and presented in Eq. (3.48), is suitable for single rotor aircraft. For the purposes of this

study, it was therefore necessary for this expression to be extended to include the induced power of all the rotors powering the multirotor. Hence the induced power for a multirotor in translational flight may be expressed as the sum of the individual induced powers of each of the rotors. For a multirotor under high speed flight conditions induced power is given by

$$P_i = \sum_{i=1}^{N_r} \frac{\kappa T_i^2}{2\rho A V_\infty} \tag{3.49}$$

and using the proposed *Intermediate Speed approximation*, the induced power for a multirotor under intermediate speed translational flight conditions is given by

$$P_i = \sum_{i=1}^{N_r} \frac{\kappa T_i^2}{2\sqrt{2}\rho A V_\infty} \tag{3.50}$$

3.2.4.5 Rotor Blade Profile Power

The Blade Profile power required to overcome the blade profile drag for a rotor in the hovering state was discussed in section 3.2.2.1. It has already been established that the airflow through a rotor operating under translational flight conditions is somewhat different than that operating in the hovering state. A more accurate approximation of the blade profile power expended to overcome the resistive blade profile drag in translational flight conditions was developed by Glauert and Bennett [83], and is given by

$$P_0 = \rho A(\Omega r)^3 \left(\frac{\sigma C_{d_0}}{8}\right)(1 + K\mu^2) \tag{3.51}$$

where K is a numerical value typically approximated at 4.7 [83], and μ is the Advance Ratio, which is the ratio of the relative wind parallel to the rotor plane to the rotor tip speed expressed by

$$\mu = \frac{V_\infty \cos\alpha}{\Omega r} \tag{3.52}$$

3.2.4.6 Parasitic Power

When an aircraft operates in relative horizontal airflow conditions, power is expended to overcome the drag force experienced by the aircraft. The Parasitic power is the

power required by the multirotor to overcome the bespoke parasitic drag force generated by the viscous shear effects and flow separation on the multirotor aerodynamic profile. In aerodynamics literature [83], this is normally expressed by

$$P_p = \left(\frac{1}{2}\rho V_\infty^2 S_{\text{ref}} C_D\right) V_\infty = \frac{1}{2}\rho V_\infty^3 S_{\text{ref}} C_D = T V_\infty \sin\alpha \tag{3.53}$$

3.2.5 UAV Power Requirements

Having identified the various power components involved in the operation of a multirotor UAV, the power required by a multirotor to hover with no external disturbances can therefore be estimated. The power requirements of a multirotor UAV in hovering flight is the sum of the induced power (P_i) and profile power (P_0) [83] such that

$$P = P_i + P_0 \tag{3.54}$$

The total hover power required for a multirotor can therefore be estimated by

$$P = \sum_{i=1}^{N_r}\left[\frac{\kappa T_i^{3/2}}{\sqrt{2\rho A}} + \rho A(\Omega_i r)^3\left(\frac{\sigma C_{d_0}}{8}\right)\right] \tag{3.55}$$

When a multirotor hovers in the presence of an external incident wind, the total power required is the sum of the hovering power together with the parasitic power. Therefore, the total power required is the sum of induced power (P_i), profile power (P_0) and parasitic power (P_p), mathematically given by the following expression:

$$P = P_i + P_0 + P_p \tag{3.56}$$

Therefore, the actual total power required for a multirotor in high speed translational flight can be approximated by

$$P = \sum_{i=1}^{N_r}\left[\frac{\kappa T_i^2}{2\rho A V_\infty} + \rho A(\Omega_i r)^3\left(\frac{\sigma C_{d_0}}{8}\right)(1 + K\mu^2)\right] + \frac{1}{2}\rho V_\infty^3 S_{\text{ref}} C_D \tag{3.57}$$

Consequently, using the proposed *Intermediate Speed approximation*, the actual total power required by a multirotor in intermediate speed translational flight may be approximated by

Figure 3.6: *Curve of Power required by a rotor with respect to True Airspeed* [86].

$$P = \sum_{i=1}^{N_r} \left[\frac{\kappa T_i^2}{2\sqrt{2}\rho A V_\infty} + \rho A (\Omega_i r)^3 \left(\frac{\sigma C_{d_0}}{8} \right) (1 + K\mu^2) \right] + \frac{1}{2} \rho V_\infty^3 S_{\text{ref}} C_D \quad (3.58)$$

Analysing the expressions for total power it is evident that the blade profile power exhibits a slight increase with an increase in relative wind speed [85], whilst the parasitic power which is attributed to the UAV drag is negligible at low speed. As wind speed increases the parasitic power term increases rapidly in proportion to the cube of the wind speed, as is evident from the mathematical model and as outlined by Johnson [85]. This is graphically demonstrated by the power curve in Figure 3.6.

On the other hand, a decrease in air density results in more power required in hover and at low and intermediate horizontal wind speeds. However, as wind speed increases this power increase is less pronounced, as a decrease in density also results in a relative reduction in parasitic drag which is more prominent at higher wind speeds [83].

3.3 Electrical Efficiency

The electrical efficiency of an electric motor is the ratio of shaft output power to the electrical input power. For the purposes of this study the motor ESCs will be considered to form part of the ESC-motor pair. Therefore, any losses incurred by the ESCs are incorporated into the motors' electrical efficiency. The ESCs of the UAV motors are provided with a source of electrical power in the form of a direct current (DC) at the voltage of the power pack. Nevertheless, because of inefficiencies within the ESC as well as within the motor itself, not all of the consumed power is delivered

to the motor/rotor shaft. For this particular study, it will be assumed that this inefficiency is constant over the utilized operating range of the motors. Thus

$$\eta = \frac{Q\Omega}{IV_{bat}} \tag{3.59}$$

3.4 Calculation of Air Density

The density of the air within which the UAV is operating is another parameter which influences the power consumption of the UAV in hovering flight. The formula recommended by the Comité International des Poids et Mesures (CIPM) for the calculation of the density of moist air is as presented in [87], [88] and [89] and is

$$\rho = \frac{pM_a}{ZRT_a}\left[1 - x_v\left(1 - \frac{M_v}{M_a}\right)\right] \tag{3.60}$$

A number of approximations have been developed that give a sufficiently precise value for the density of moist air but these are not as sophisticated as the CIPM-2007 equation. A comparative analysis of the various approximations by Mandal et al. [90] established that Eq. (3.61) is the best approximation, having a deviation of 0.0004 % from the CIPM-2007 equation. This is presented as

$$\rho = \frac{3.48488 \cdot p - (8.0837 + 737.4 \times 10^{-3}t + 975.25 \times 10^{-6}t^3) \times RH}{(273.15 + t) \times 10^3} \tag{3.61}$$

For the purposes of this study Eq. (3.61) for the approximation of the density of moist air is used throughout.

4 Development of Two Multirotor UAV Designs

This chapter details the design and development of the two custom-built UAVs used during this research study. A detailed explanation is given for both the UAV platforms and the integrated Sensor Suite on board the UAVs. This is followed by an outline of the various parameter subsets and their subsequent measurement and logging by each subsystem. The chapter concludes by describing the measures taken to facilitate the eventual synchronization of the various data subsets into one data set.

Understanding the effect of wind conditions on the flight endurance of a UAV required the design, development and assembly of a test vehicle rigged with an array of appropriate sensors capable of measuring and logging the parameters relevant to this investigation. Different UAV configurations have been developed over recent years, including fixed wing, tilt rotor and multirotor configurations [91]. Each of these configurations has its own technological advantages and limitations depending on how and where the UAV is deployed. Since this particular study is specifically related to hovering UAVs, the multirotor UAV platform was selected as such a vehicle is very capable of maintaining a stable hover.

4.1 Test System Design

Having established that the multirotor UAV was the most suited test platform for this study, the potential multirotor UAVs that could be used were considered in more detail. At this stage of the project three quadcopter UAV concepts were considered, each of which is further detailed in Table 4.1.

4.2 UAV Test Vehicles

As already outlined, two multirotor test vehicles were purposely developed and built for this study. During the first phase of the study a quadcopter UAV was used. Unfortunately, on 16 April 2019, the quadcopter UAV experienced an uncontrolled descent from an altitude of 80 m during one of the UAV data collection flights. The resulting abrupt descent resulted in severe damage being inflicted on the UAV itself. After a careful investigation into the cause of the incident it transpired that the UAV experienced a failure in the propulsion system on arm 3. This was evident from the flight controller data as, just prior to the rapid descent, the Pulse Width Modulated

Table 4.1: *Quadcopter setups considered.*

Setup	*Basic*	*Moderate*	*Superior*
Frame	F450	F450	Tarot Ironman 650
Rotor Pitch (mm)	455	455	680
Propulsion System	DJI E310	DJI E600	DJI E800
Propeller	DJI 9450	DJI 1242	DJI 1345
Propeller Diameter (mm)	240 mm	310 mm	345 mm
Battery	LiPo 4S1P	LiPo 6S1P	LiPo 6S1P
Recommended Take-off Weight (kg)	1.6	2.4	3.2
Maximum Combined Thrust (kg)	3.2	6.4	8.4

(PWM) signal from the Flight Controller to this propulsion arm rose abruptly to 100 %. This indicates that the flight controller sensed a loss of thrust from this propulsion arm, hence reacting by demanding maximum power from this arm, apparently without any response. This incident highlighted the lack of redundancy and consequent vulnerability of a quadcopter UAV [80]. Based on this event it was decided that a replacement UAV of the hexacopter type would be developed and built for the second phase of this study.

Hexacopters, which inherently possess a higher degree of controllability than quadcopters, are also capable of remaining airborne in the event of failure of one rotor, provided that the AUW of the UAV is still within the maximum thrust limits of the five remaining operational rotors. This makes this type of UAV safer to operate and more stable in the air.

Each of the test vehicles was equipped with an array of appropriate sensors to measure and log the relevant parameters throughout the duration of the data collection flights eventually executed using the respective UAVs.

Each multirotor UAV vehicle consisted of two main systems. Although the two systems of each UAV were physically integrated into one vehicle as shown in both Figure 4.1 and Figure 4.2, for development purposes these were considered as two separate main systems namely:

1. The Multirotor Platform, and
2. The Sensor Suite.

Each of the above-named main systems consisted of several subsystems, each of which is described in more detail hereunder.

4.3 The Multirotor Platforms

Each multirotor platform was made of a rigid frame with equally spaced arms protruding radially from its centre hub. At the end of each arm a motor-driven propeller was attached. When the propellers were operated in unison, they generated enough thrust for the UAV to lift off the support skids. Each multirotor platform was fitted with a sensor suite which monitored the flight performance parameters throughout the duration of the flight.

4.3.1 The Quadcopter UAV

A quadcopter UAV frame was used for the first phase of the study. The frame used was an off-the-shelf Tarot Ironman 650 frame [92], which was modified to better suit the purposes of this study. The rotor-to-rotor diagonal distance of the Tarot Ironman 650 frame is 650 mm. The completed Quadcopter UAV setup is shown in Figure 4.1.

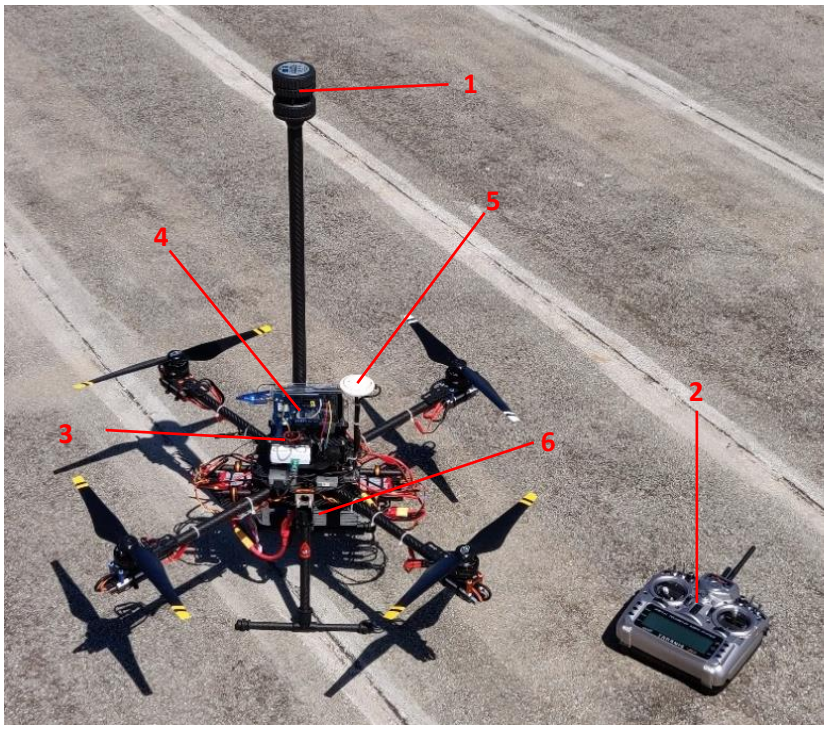

1	FT205EV Ultrasonic Wind Sensor	**4**	Arduino Data Logger
2	FrSky Taranis X9D Plus Radio Transmitter	**5**	DJI GNSS antenna
3	Atmospheric sensors mounting plate	**6**	LiPo Battery power pack

Figure 4.1: *Photo of the completed Quadcopter UAV setup.*

4.3.2 The Hexacopter UAV

Following the incident with the quadcopter UAV, a more robust and fault tolerant hexacopter UAV was eventually developed. The hexacopter frame used was a modified off-the-shelf Tarot FY680 frame [93], having a rotor-to-rotor diagonal distance of 680 mm. Similar to the quadcopter frame described in section 4.3.1, it was made of lightweight carbon fibre reinforced polymer (CFRP) and aluminium alloy fittings. The completed hexacopter UAV setup is shown in Figure 4.2.

4.3.3 Modifications

For the UAV platforms to better serve the purposes of this study, a number of modifications to the off-the-shelf frames were implemented.

4.3.3.1 Battery Mounting

Multirotor UAVs are typically assembled with the battery power pack mounted on the top of the vehicle. The main reason for this is to mount the UAV's payload, especially when the payload is of image recording capabilities, to the underside of the vehicle. In

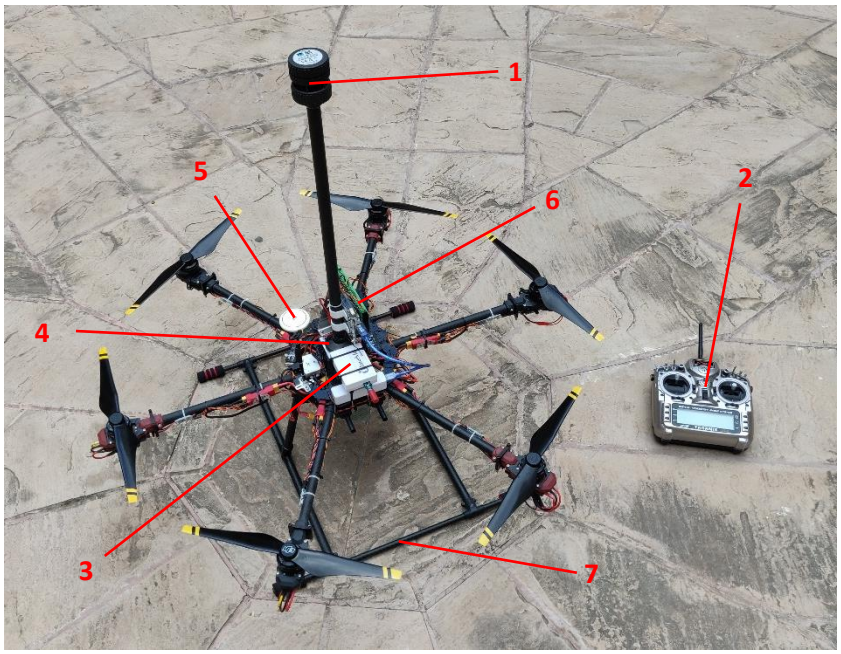

1	FT205EV Ultrasonic Wind Sensor	**5**	DJI GNSS antenna
2	FrSky Taranis X9D Plus Radio Transmitter	**6**	Arduino Data Logger
3	iMet-XQ2 Environmental Sensor	**7**	Extended Landing Support Skids
4	Atmospheric sensors mounting plate		

Figure 4.2: *Photo of the completed Hexacopter UAV setup.*

this way the imaging device can be oriented to point downwards towards the ground, without having any UAV components infringing on the device's viewing angle. The payload for these research UAVs was a Sensor Suite, parts of which needed to be mounted at a height above the UAVs' rotors. It was therefore more appropriate for the battery power pack of both the quadcopter and hexacopter UAVs to be mounted to the underside of the vehicle. This setup also improved the weight distribution of the UAV about its geometric centre along the vertical axis, and consequently improve stability during flight. A new custom battery mount, shown in Figure 4.3 was designed and fabricated to support the substantial weight of the battery pack of more than 800 g. The battery mount was also fitted with an under-battery lock plate to ensure that the battery straps did not get undone during UAV operations.

4.3.3.2 Atmospheric Sensors Mounting Plate

The original battery mounting plate was repurposed as the Atmospheric sensors mounting plate. Located on top of the UAV frame, it was modified and fitted with a base platform for a 500-mm long CFRP vertical pole onto which an ultrasonic wind sensor was mounted (see Figure 4.1 and Figure 4.2). This mounting plate was also raised upwards using elongated nuts to create space for the wind sensor cables' routing without fouling the flight controller fitted beneath it.

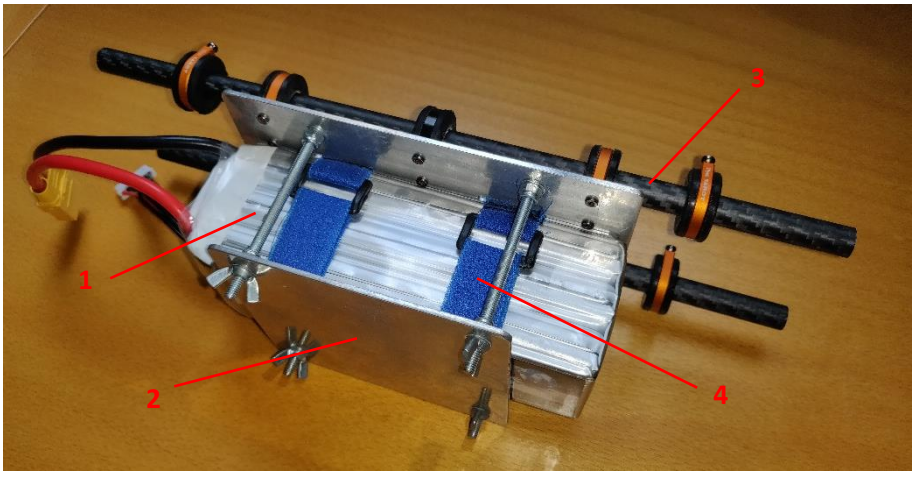

1	Battery Power pack	**3**	Battery Mount Suspension Bars
2	Battery Lock plate	**4**	Battery Straps

Figure 4.3: *Battery power pack fitted inside the battery mount developed for the attachment of the battery power pack to the underside of the UAV.*

At the front end of the atmospheric sensors mounting plate an extension was also developed and incorporated onto which the stand-alone environmental sensor was eventually mounted. Meanwhile, the rear end of the bespoke plate was fitted with a support bracket for the Arduino-based data logger and a voltage regulator used to regulate the power to the Ultrasonic wind sensor.

4.3.3.3 Landing Support Skids

The Tarot FY680 hexacopter frame was equipped with a pair of landing support skids having an overall footprint of 275 mm x 275 mm. This was deemed to be rather small for the hexacopter size. Such a small landing gear footprint could potentially lead to the tipping over of the hexacopter during landing, especially in windy conditions. To increase the UAV's stability during the landing phase and hence mitigate the risk of the UAV tipping over during landing, the landing support skids were modified to a more stable 500 mm x 500 mm square footprint, as shown in Figure 4.2.

4.3.3.4 UAV Motor Mounts

The DJI 1345 propellers measuring 345 mm in diameter used for this build, did not fit the 680 mm diagonal rotor-to-rotor distance of the standard Tarot FY680 frame without interfering with each other for a coplanar hexacopter configuration. The arms of the hexacopter frame were therefore fitted with motor mounts, shown in Figure 4.4,

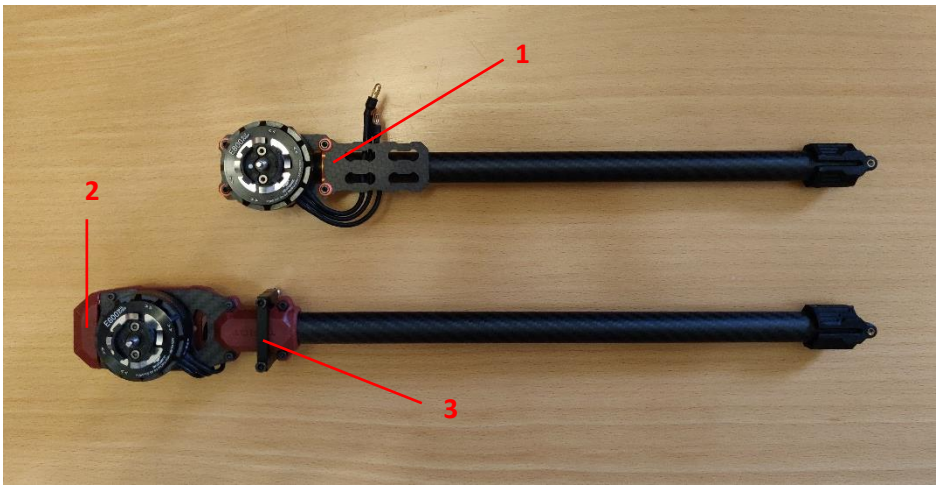

1 Standard Motor Mount

2 Tarot 680 Pro Motor Mount

3 Aluminium Alloy Pipe Clamp

Figure 4.4: *Motor mount used for the research hexacopter (bottom) compared to the standard motor mount (top).*

intended for the Tarot 680 Pro model, resulting in a rotor-to-rotor diagonal distance of 805 mm. This resulted in a rotor tip-to-tip clearance of 57.5 mm. This modification also has the added benefit, as indicated by Prudden et al. [94], that a greater separation between rotors results in a reduction in loss of thrust for the downwind rotors caused by rotor wake interference.

The new motor mounts were secured to the boom ends by screwed polymer pipe clamps. It was considered that the vibrations generated by the multirotor operations, as well as any potential aggressive corrections when operating in windy conditions, could tear the polymer clamps. Although these new mounts are specifically designed for use on multirotor frames, they were reinforced further by fitting aluminium alloy pipe clamps over them to render the assembly failsafe in the case of any tears to the polymer material.

4.3.4 UAV Configuration

Multirotor aircraft with coplanar rotors can be set up in a number of configurations. The number of possible configurations increases for an increasing number of rotors. The two most popular configurations are a multirotor having one rotor lined up with the front (nose) of the aircraft, whilst the second configuration is with two rotors at the front of the aircraft, straddling the aircraft's longitudinal axis as shown in Figure 3.2 and Figure 3.3. These configurations are commonly referred to as + configuration and × configuration respectively. The × multirotor configuration is considered to be more stable in translational flight when compared to a + configuration, whilst the + configuration is the preferred choice amongst those opting for an aerobatic aircraft capable of more aggressive manoeuvring [95]. For the purposes of this study, stability of the aircraft was of significant importance. However, since data collection was conducted with the UAV in hovering flight conditions, the choice of configuration was not critical, as there is no difference between the two configurations when the aircraft is in hover. In view of this, the configuration chosen for both the quadcopter and hexacopter platforms was the × configuration.

4.3.5 Flight Controller and Propulsion System

An integral part of any UAV is the flight controller which translates the desired manoeuvres of the UAV operator into control outputs for the various UAV rotors. The flight controller used for both multirotor platforms developed was a DJI N3 unit,

shown in Figure 4.7, which is also equipped with a data logging function for various flight parameters [96]. This feature was especially desirable for the purposes of this study. The flight controller unit is also equipped with an IMU, which comprises accelerometers, gyroscopes, and magnetometers to accurately detect and measure all translational and angular UAV movements. During the assembly stage of the multirotors, particular attention was paid to ensure that the flight controller unit was installed at the multirotors' geometric centre so as to maximize the operational accuracy of this unit. To further enhance the performance and controllability of the UAVs, the various components and onboard systems were laid out and eventually installed in such a way as to maintain the Centre of Gravity (CoG) of the aircraft in close proximity to the geometric centre of the UAVs.

The propulsion system fitted on the UAV multirotor platforms was a DJI E800 tuned propulsion system [97], whose components are shown in Figure 4.5. The DJI 3510 motors are 350 rpm/V Brushless DC (BLDC) motors of the out-runner type. These are each driven by an E-series 620S ESC. The propellers fitted onto the out-runner motors were the DJI 1345 twin-bladed fixed pitch propeller having a diameter of 345 mm (13.6 inches) and a pitch of 115 mm (4.5 inches). Each of the propeller-motor-ESC assemblies was mounted onto the end of each multirotor frame propulsion arm and is capable of generating a maximum thrust of 2100 grams at a supply voltage of 25 V at sea level.

Figure 4.5: *DJI 1345 propeller, E-series 620S ESC, and a DJI 3510 brushless DC motor, utilized for the propulsion system of the research UAVs.*

4.3.6 Battery Power Pack

There are a number of power pack technologies available for powering a UAV vehicle. However, the most widely used power pack is the LiPo type. This power pack has several advantages. Primarily it has a high energy density when compared to the actual power pack weight, and it is also capable of delivering substantially high currents. This is especially desirable when powering multiple motors from the same battery pack. Each LiPo cell has a resting voltage of 3.7 V and can be charged to 4.2 V at full charge. LiPo technology offers a relatively linear voltage drop against pack remaining capacity. This characteristic has the advantage of making it easier to estimate the remaining charge in the power pack during flight, by monitoring the power pack voltage. Based on these characteristics, the power pack selected to power the research multirotors was a 6000 mAh, 6S1P LiPo battery capable of 25.2 V at full charge. This is shown in Figure 4.6.

4.3.7 The Radio System

A UAV vehicle is controlled from a radio system. A basic radio system consists of a radio transmitter (Tx) and a radio receiver (Rx). The radio transmitter is handheld by the UAV operator and is the device which the pilot or operator manipulates to manoeuvre the UAV. The radio receiver is installed onboard the UAV vehicle and its function is to relay the wireless signals sent by the radio transmitter to the flight controller. The radio transmitter used for this study was an FrSky 8-channel

Figure 4.6: *LiPo battery power pack used to power the research UAVs.*

Taranis x9D Plus shown in Figure 4.2. This also has a telemetry logging function. The receiver used was an FrSky X8R radio receiver, shown in Figure 4.7. This was connected to the DJI N3 flight controller using a Serial BUS (SBUS) communication protocol.

SBUS is an inverted Universal Asynchronous Receiver-Transmitter (UART) communications protocol, which permits the transmission of multiple channel signals between the radio receiver onboard the UAV and the flight controller over a single signal cable. Traditionally, a signal cable needs to be routed for each radio control channel. The use of a single signal cable system was particularly desirable as it was of concern whether there would be any interference between the different onboard systems. Such a concern was primarily due to the substantial density of cabling in the relative confines of the UAV centre hub, most especially in regions where power distribution system cables were routed.

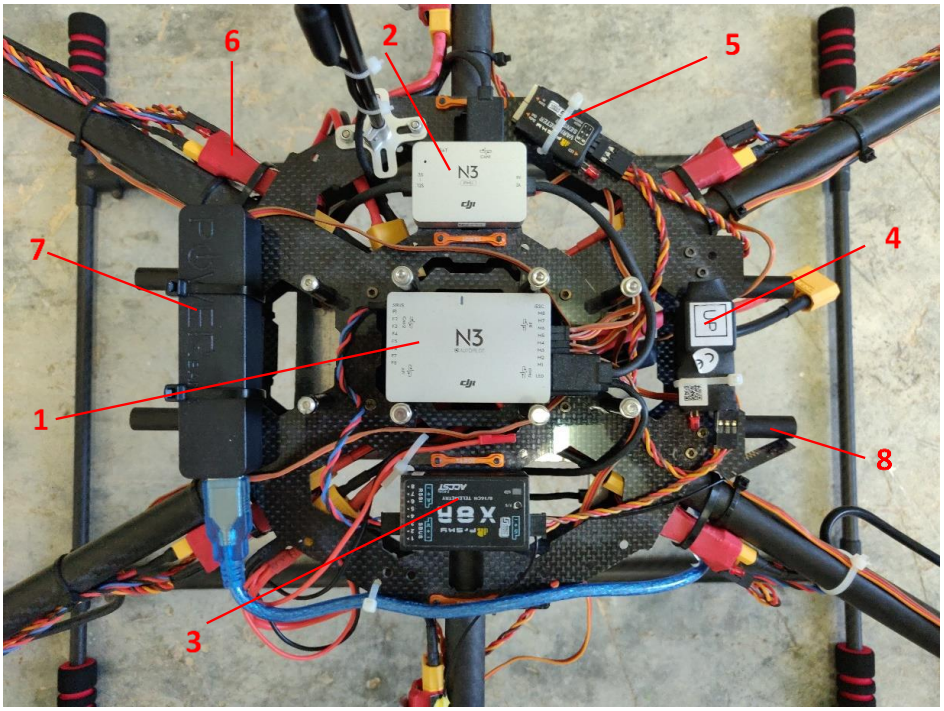

1	DJI N3 Flight Controller	**5**	FrSky Vari-H Variometer
2	DJI Power Management Unit	**6**	FrSky FAS-40S Current Sensor
3	FrSky X8R Radio receiver	**7**	Power pack for Arduino Data Logger
4	FrSky GPS Sensor	**8**	Battery Mount Suspension Bars

Figure 4.7: *Hexacopter UAV platform centre hub, with wind sensor mast assembly removed.*

In order to maintain a better control on the hovering altitude of the UAV, the throttle lever response characteristic of the radio system was modified from a linear response to an exponential response. The region of the throttle lever for the hovering position was given a smaller gradient in order to achieve fine adjustment characteristics on the throttle control. A simplified control architecture of the hexacopter UAV used for this study is graphically shown in Figure 4.8.

4.4 The Sensor Suite

The function of the integrated Sensor Suite subsystem was to measure and log an array of parameters relevant to the study. The primary objective was to collect and log data which potentially has an influence on the performance of the UAV when operated in different open field atmospheric conditions. During the design process it was also decided that other parameters relevant to the field of multirotor studies, but that were not necessarily needed for this particular study, would still be logged for the purposes of any future further research. The parameters that were being continuously monitored and recorded throughout the duration of the data collection flights have been grouped into the following parameter subsets:

1. UAV Flight Parameters;
2. UAV Platform Parameters;
3. Environmental Parameters.

The Sensor Suite subsystem incorporates a number of independent sub-subsystems, each of which is predominantly dedicated to the recording of a particular parameter subset from the above.

4.4.1 UAV Flight Parameters

The subset of flight parameters was measured and logged by the UAV Flight Controller, namely the DJI N3 controller. This particular flight controller was specifically selected for this study due to it being equipped with an integrated black box function for the logging of flight parameters. The unit recorded an extensive array of parameters including PWM signals to each of the UAV propeller motors, UAV attitude angles, horizontal and vertical velocities, linear and angular accelerations, flight time, GPS location, altitude and time, and battery voltage, together with other relevant parameters.

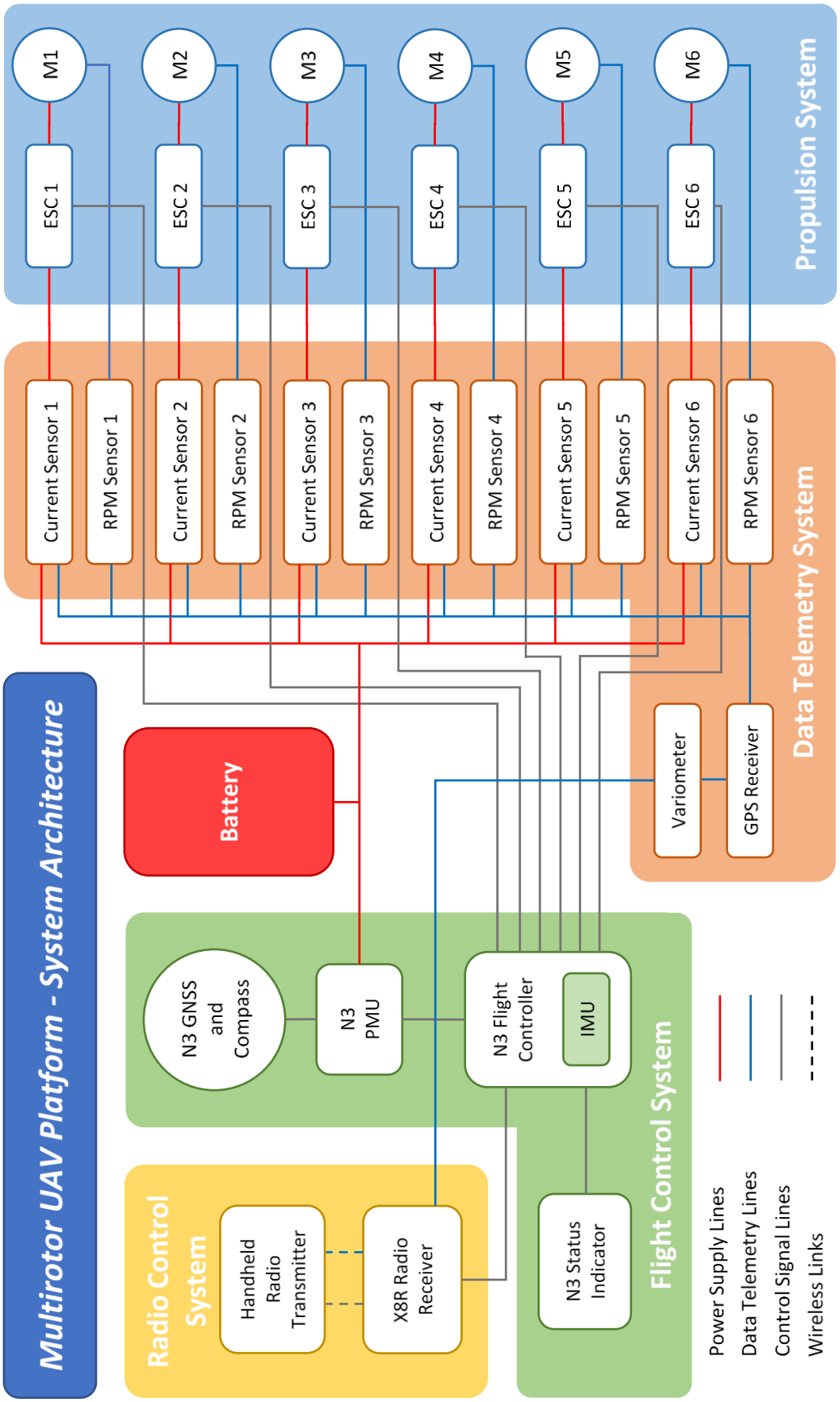

Figure 4.8: *Multirotor UAV Platform System Architecture.*

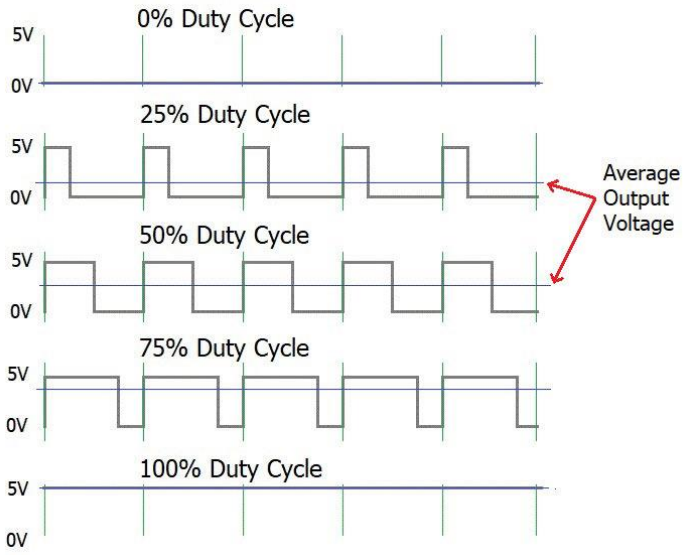

Figure 4.9: *Typical 5 V PWM signal and duty cycle [98].*

4.4.1.1 UAV motors' PWM signal

A PWM signal is computed by the flight controller for each of the UAV's motors and is communicated to the respective ESC unit. The PWM signal communicates the amount of power that needs to be delivered to the motor from the battery power pack. This is achieved by a switching signal (ON-OFF pulse per cycle of the signal), as shown in Figure 4.9. The ESC interprets this signal from the Flight Controller and regulates the voltage applied to the motor terminals. A higher PWM duty cycle means that the ON portion of the signal is longer, driving the ESC to deliver more power to the motor. This regulates the thrust that each motor generates.

4.4.2 UAV Platform Parameters

Another parameter subset includes those pertaining to the UAV platform performance. In order to properly evaluate the UAV platform performance, the current and voltage being delivered to each propulsion arm, together with the speed in Revolutions Per Minute (RPM) of each rotor and the UAV Global Positioning System (GPS) data, would be necessary. A system to measure and log the named parameters was developed using a series of sensors, shown in Figure 4.10, together with the radio system's telemetry logging function.

The UAV platform was fitted with an FrSky FAS-40S Smart Port Current Sensor for each of the motors. This monitored the battery voltage and the electric current drawn

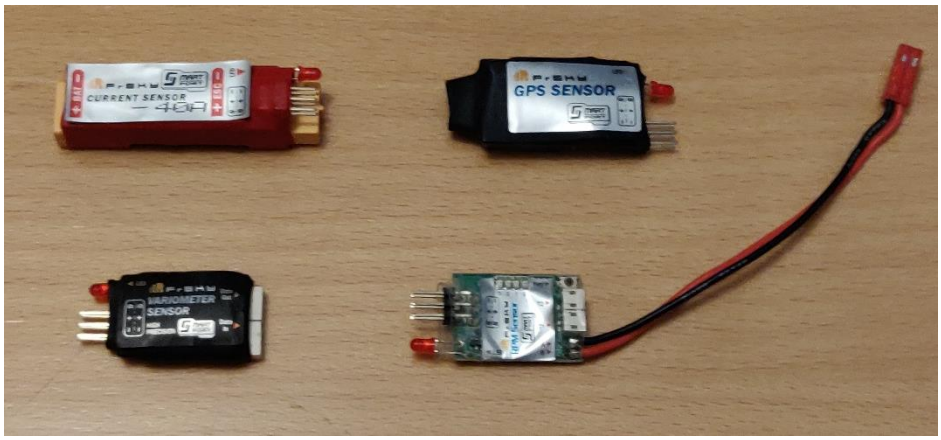

Figure 4.10: *FrSky sensors for UAV platform parameters – Clockwise from top left, Current Sensor, GPS Sensor, RPM Sensor and Variometer.*

by each of the UAV motors. The RPM of each motor was measured by FrSky brushless motor RPM sensors that detect the voltage changes at the motor cables, based upon which the RPM is computed. A cable harness was specifically developed and fabricated to connect the ESC, propeller motor and RPM sensor at every UAV propulsion arm, for the RPM sensor to read the motor RPM. The bespoke pair of sensors for each motor was fitted onto the respective propulsion arms.

An FrSky Vari-H variometer that measures UAV altitude and an FrSky GPS sensor to timestamp the respective data were also fitted to the UAV. These two sensors were installed on the UAV centre hub, as shown in Figure 4.7.

Each of the above detailed sensors were connected using a daisy chain network configuration as shown graphically in the system architecture in Figure 4.8. Furthermore, each sensor was configured with a unique channel address over which the respective measurements were sent in real time to the radio control unit. These were logged on a microSD card installed in the hand-held radio control unit at a frequency of 5 Hz.

4.4.3 Environmental Parameters

The initial hypothesis was that environmental parameters have an impact on the performance of a UAV in hovering flight. To evaluate this hypothesis, parameters including wind speed and direction, atmospheric pressure, atmospheric temperature and relative humidity were measured and logged. Two independent systems were utilized to log the full complement of environmental parameters needed.

4.4.3.1 Ultrasonic Wind Sensor

The key environmental parameters for this study were the wind speed and direction at which the UAV was operated. An ultrasonic wind sensor was used to measure these parameters. Although there are several ultrasonic wind sensors available on the market, only a handful are developed specifically for UAV applications, more precisely for mounting on UAVs. For a wind sensor to be suitable for mounting on a UAV, especially a multirotor, two very important characteristics are the overall weight of the sensor and its aerodynamic profile. Most of the ultrasonic wind sensors available are relatively heavy, in the range of 500 g, and have a substantially large aerodynamic profile, typically larger than 100 mm in diameter. These two characteristics are relatively unimportant for a wind sensor mounted on a ground-based station. However, when mounting such a sensor on a multirotor UAV and since the sensor is mounted high above the multirotor centre hub, it is of utmost importance that it is as light as possible. Otherwise, it would negatively affect the second moment of area of the vehicle, making the UAV unstable in flight. Furthermore, the aerodynamic profile of the sensor needs to be as small as possible to keep the drag force generated by the incident wind to a minimum. It should be noted that even a small drag force results in a large moment on the UAV, due to the height of the sensor above the UAV platform. This makes the UAV less tolerant to high winds and requiring more power demanding rotor corrections to maintain the UAV hovering in the correct position at the right attitude. Unsurprisingly this could potentially have a negative effect on UAV endurance. After taking into account the outlined considerations, the FT205EV Ultrasonic wind sensor from FT Technologies [32] was selected for the measurement of the wind speed and wind direction in this study. This sensor, which is shown in Figure 4.11, was specifically developed for UAV applications.

The FT205EV sensor was mounted atop a 500 mm pole fixed to the Atmospheric sensors mounting plate above the UAV, to minimize the potential effect of the airflow induced by the UAV rotors on the measurements.

4.4.3.2 Environmental Sensor

A BME280 Environmental sensor from Bosch Sensortec [99] was integrated into the Environmental Parameters logging system to measure atmospheric pressure, relative

Figure 4.11: *FT205EV wind sensor from FT Technologies* [32].

humidity and air temperature. This sensor was mounted on the base of the atmospheric sensors mounting plate.

4.4.3.2.1 Arduino-based Data Logger

An independent data logging system was developed to measure and log environmental data. The FT205EV wind sensor, the BME280 Environmental Sensor, and a GPS sensor were integrated as part of this system.

An Arduino Mega 2560 Rev 3 development board was used to assemble the data logger developed for the logging of the wind sensor and environmental sensor parameters. A GPS data logger shield incorporating a NEO-6M GPS receiver and a microSD card writer was stacked onto the Arduino Mega 2560 Rev 3 board. The FT205EV wind sensor was connected to one of the board's serial ports using UART communication, whilst the BME280 Environmental sensor, was connected using a Serial Peripheral Interface (SPI). A schematic diagram for this data logger system is shown in Figure 4.12.

A script was developed to manage the data from the various sensors using a baud rate of 9600 baud. The wind sensor was configured to communicate a standard NMEA 0183 MWV data string containing the wind speed and direction, amongst other parameters, at a frequency of 5 Hz. The availability of every new data string from the wind sensor was used as a trigger to collect the current data values from the other sensors connected to the data logger. The full string of data compiled from the readings

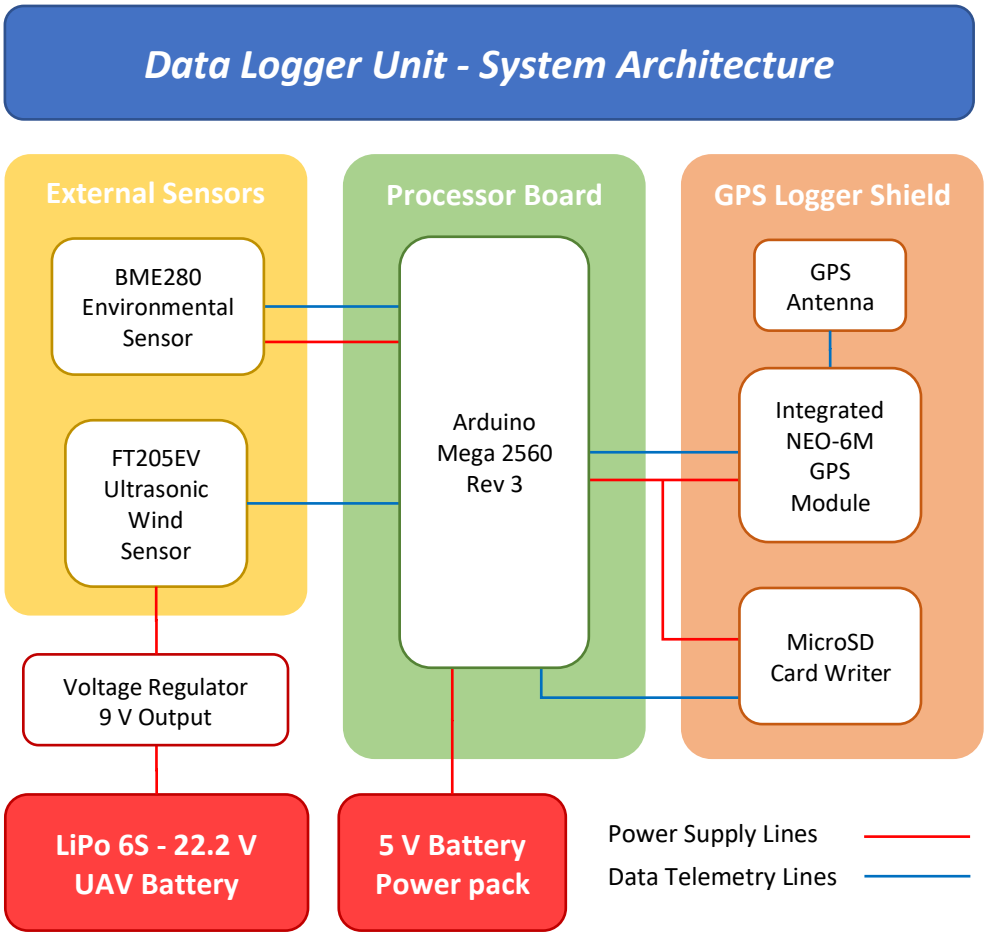

Figure 4.12: *Schematic diagram of custom developed Arduino-based data logger used for the recording of environmental parameters.*

received from the wind sensor, environmental sensor and GPS receiver, as well as the Arduino Mega board's internal clock, were eventually written to the microSD card.

4.4.3.3 Stand-alone Environmental Sensor

During the development phase of the Sensor Suite, a more suitable stand-alone environmental sensor was made available for mounting onto the UAV by the Institute of Earth Systems at the University of Malta. The self-contained iMet-XQ2 environmental sensor [34], shown in Figure 4.13, is also specifically developed for UAV applications. This sensor measured and logged atmospheric pressure, relative humidity, and air temperature, together with GPS location, altitude and time at a frequency of 1 Hz.

Figure 4.13: *iMet-XQ2 stand-alone Environmental Sensor for UAV applications.*

4.5 Assembly of the Multirotor UAVs

During the design stage of both multirotor UAVs, the aircraft were structured into modular units as much as possible. This facilitated both the initial assembly process as well as the replacement of any components should the need arise. The modular units of each UAV were predominantly the:

1. UAV centre hub;
2. Propulsion arms:
    a. Four for the quadcopter assembly;
    b. Six for the hexacopter assembly;
3. Removable Sensor assembly.

The final AUW of the research UAVs added up to 3121 grams for the quadcopter assembly and 4278 grams for the hexacopter assembly. In order to ensure proper and reliable research UAVs, during the assembly phase a number of considerations were taken into account to mitigate the risk of potential problems further into the course of the study. The considerations most specific to the assembly of the UAVs are outlined below.

4.5.1 UAV Motor Mounts Assembly

It was considered critical that the motor mounts of each propulsion arm for both the quadcopter and hexacopter builds were mounted accurately and in proper alignment such that the mounted motor's axis of rotation was normal to the plane of the UAV

centre hub. Such alignment was achieved by first mounting the propulsion arms to the centre hub via the mounting attachment at the end of each arm. This ensured that the arm did not rotate about its longitudinal axis. The motor mounts were then mounted onto the propulsion arms contemporarily, whilst the UAV frame was held flat on a surface table. Each of the motor mount bases was set in alignment with the reference surface table. Once the motor mounts were properly set these were secured in place via the securing bolts of each motor mount.

4.5.2 UAV Cabling

As described earlier in this chapter, the research UAVs were equipped with multiple onboard systems. This resulted in substantial cabling routed between the various onboard components. Furthermore, the cabling operated at different voltages and current intensities. Such a scenario could lead to potential electromagnetic interference between systems, potentially rendering some systems inoperable. To mitigate the risk of such interference, the onboard cabling was categorized into three main categories, these being:

1. Power Supply Lines;
2. Control Signal Lines;
3. Data Telemetry Lines.

Each cable category was therefore routed using the principle of protection against electromagnetic interference by separation, whereby each cable category was, wherever possible, routed via a different physical route. Although the power supply cables operated at a relatively constant DC voltage and current, thereby minimizing the potential of electromagnetic interference, it was still considered safer to route such cables separately.

4.6 LiDAR Wind Measurement Unit

It has already been stated in section 4.4.3.1, that wind data were of key importance for this study. The wind data collected by the research UAVs whilst in flight, needed to be validated by correlating the collected data with a reliable reference. The reference instrument used for this study was a ZephIR 300 LiDAR wind measurement unit [100] supplied by the Institute for Sustainable Energy of the University of Malta.

Figure 4.14: *The ZephIR 300 LiDAR unit installed on the rooftop of the WSC-RO Plant, at Ċirkewwa, l/o Mellieħa, Malta.*

The ZephIR 300 LiDAR unit is a ground based, continuous wave LiDAR system wind measurement instrument. It has the capability of measuring wind speed and direction at ten different pre-set altitudes above the measurement window. Throughout the duration of this study the measuring altitudes were set at 10 m, 20 m, 30 m, 40 m, 50 m, 60 m, 80 m, 100 m, 150 m and 200 m.

The instrument was installed on the rooftop of the Water Services Corporation (WSC) Ċirkewwa Reverse Osmosis (RO) Plant, at Ċirkewwa, l/o Mellieħa, Malta, as shown in Figure 4.14. The coordinates for its installed position were 35.985 96° N, 14.335 14° E. The measurement window of the unit was set at six metres above ground.

4.7 Measurements and Uncertainties

The equipment described in this chapter provided measurements for an array of parameters that were eventually used for the analysis of the different phenomena under study during this research. As outlined in section 4.4.1, the UAV Flight parameters logged by the DJI N3 flight controller included a series of parameters utilized for data validation purposes, whilst the GPS data and flight time were used for data

synchronization purposes, as detailed in sections 4.8 and 5.4. The PWM signals and battery voltage were utilized for UAV performance analysis with the voltage reading having a typical accuracy of $\pm$ 0.5 V.

The UAV platform parameters were measured by a series of FrSky Smart Port sensors, shown in Figure 4.10, and logged by the UAVs' radio control unit, as indicated in section 4.4.2. The FrSky FAS-40S Smart Port Current Sensor provided recorded measurements for the current drawn by each propulsion motor with an accuracy of $\pm$ 0.1 A. These current readings were used together with the battery voltage reading from the DJI N3 Flight Controller to calculate the individual power consumption of each motor as well as the total power consumption of the research UAVs. The high precision FrSky Vari-H variometer measured the UAVs' altitude with a resolution of 0.1 m and was used to establish the altitude at which the UAV was hovering during UAV operations, as well as for data validation purposes during the data post-processing stage. This reading was preferred over the GPS data altitude reading as the variometer had a better data refresh rate than the FrSky GPS sensor connected to the radio control unit.

The environmental parameters were primarily measured by the FT205EV Ultrasonic wind measurement sensor and the iMet-XQ2 standalone environmental sensor, whilst ground based measurements of the wind conditions at the time of UAV operations were measured by the ZephIR 300 LiDAR wind measurement unit, as detailed in section 4.4.3. The FT205EV ultrasonic sensor measured wind speed at an accuracy of $\pm$ 0.1 m/s and wind direction at an accuracy of 4° RMS. The iMet-XQ2 environmental sensor measured atmospheric pressure, relative humidity, and air temperature, at accuracies of $\pm$ 1.5 hPa, $\pm$ 5 % RH and $\pm$ 0.3°C respectively, whilst the ZephIR 300 LiDAR unit measured wind speed and wind direction at accuracies of $\pm$ 0.1 m/s and a direction variation of less than 0.5° respectively.

Although some of the measured parameters were used directly in the respective analyses detailed in chapter 6 of this dissertation, a number of other parameters, such as air density, power and other averaged or summated parameters were calculated based on the parameters measured by the various sensors used during the data collection campaign. Invariably such calculations introduced uncertainties beyond

those quoted for the sensor inaccuracies. An appropriate analysis of such uncertainties for such parameters has been detailed in Appendix C.

4.8 Data Synchronization

As outlined earlier, parameters were being logged by a number of independent systems onboard the UAV as well as on the ground. In studies also dealing with wind measurements from UAV-mounted sensors [51, 52], the data collection frequency of 1 Hz was used, which is typical for wind measurement applications. In order to achieve better data resolution, data for this study were predominantly logged at a frequency of 5 Hz. So as to facilitate the proper synchronization of the data from the various systems, each independent system was fitted with a GPS sensor used to GPS time stamp each record of the system. Following each data collection session and once all the data were downloaded from the various data loggers, these were to be synchronized to the common GPS timestamp.

5 Data Collection Methodology

This chapter details the methodology and procedures used to maximize the validity of the data collected, whilst mitigating any risks brought about by such UAV operations. A description of the operational sites selected and what permits were required for the research UAV operations are described. This is followed by a detailed description of the UAV preparation prior to any flights and the details of what precautions were taken and how such flights were conducted. This chapter also outlines some of the challenges encountered during the process of conducting this research.

The primary objective of the methodology is to establish the steps and measures taken to ensure high quality data are measured while ensuring that appropriate health and safety measures are in place to address risks associated with flying UAVs in an open field environment. Any external factors that could have impacted the validity of the data collected were given due consideration and where possible, mitigation measures implemented.

5.1 UAV Operations Sites

For the study to be as comprehensive as possible several sites were identified for the different stages of this study. Operational sites were identified for:

1. Open Field Data Collection Flights,
2. Sheltered Data Collection Flights, and
3. Tied Down Data Collection Flights.

Each of the selected sites is described in detail hereunder.

5.1.1 Site for Open field Data Collection Flights

The Maltese islands is a small archipelago located in the central Mediterranean basin. A number of suitable sites from where the UAV data collection flights could be conducted were carefully considered. During the selection process several factors were taken into consideration, including the site's location in relation to the local prevailing wind direction. The prevailing wind direction over the Maltese islands is the *Majjistral* (North West), as clearly indicated in a long-term climate report for the Maltese islands by Galdies [101], and studies conducted by Farrugia et al. at Wied Rini [102], as well

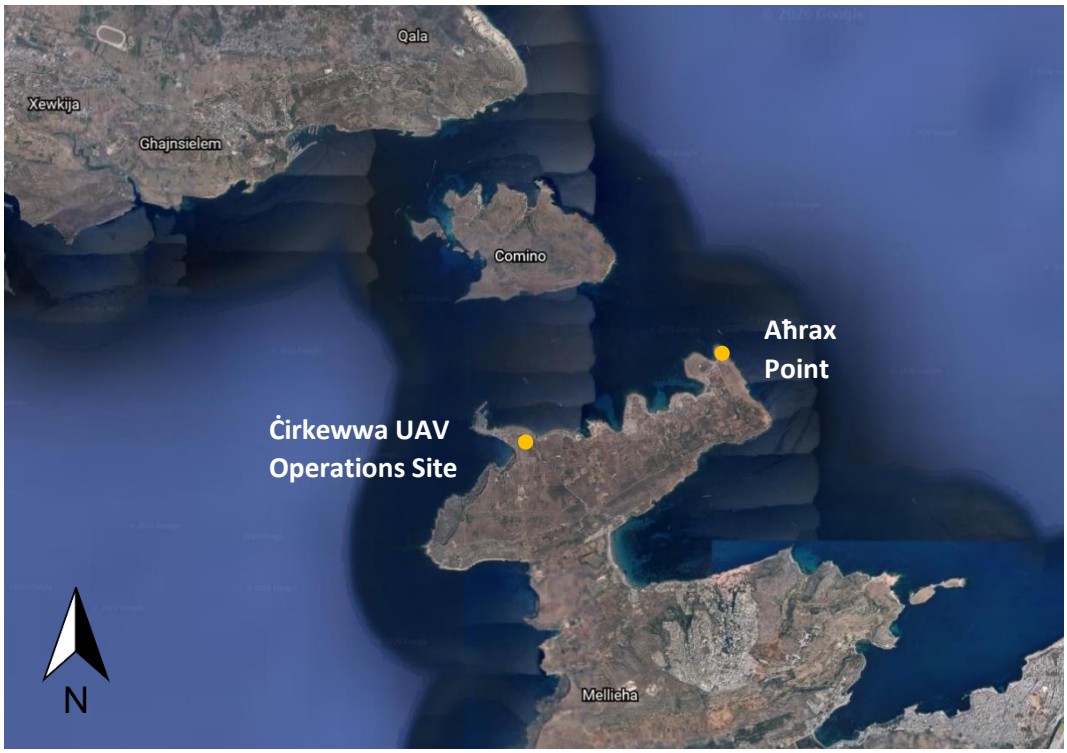

Figure 5.1: *UAV operations site at Ċirkewwa, l/o Mellieħa, Malta. – Source: Google Earth 2020.*

as at Aħrax Point [103]. The Aħrax Point site for the latter study lies approximately 3 km to the East North East (ENE) of the site eventually chosen for the UAV operations in connection with this study, as indicated in Figure 5.1.

Furthermore, it was desired that the wind conditions at which the UAV data collection flights were conducted would have a low turbulence intensity (<10 %). A coastal location at Ċirkewwa, l/o Mellieħa, that is well exposed to the north-westerly winds was thus selected. Apart from being at the north-western tip of the island of Malta and experiencing unobstructed wind flows from the prevailing *Majjistral*, the site is easily accessible by road.

It was also considered necessary that the selected hover site for the open field data collection flights was such that both the operating UAV and the UAV rotors' induced airflows did not disturb the LiDAR Wind Measurement Unit readings. In view of this it was opted that the hover site for the data collection flights be downwind of the LiDAR wind measurement unit when subject to the prevailing *Majjistral* as shown in Figure 5.2. The use of the indicated hover site ensured that, for data collection flights conducted under prevailing wind conditions, the UAV would not penetrate the LiDAR

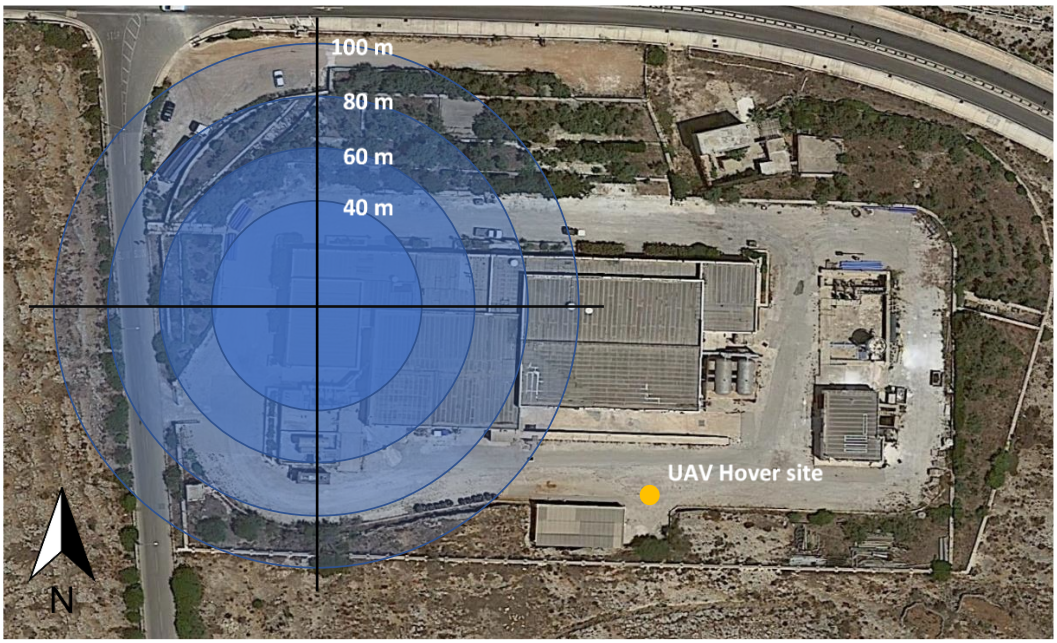

Figure 5.2: *Aerial image of the Ċirkewwa UAV operations site showing the diameter of the LiDAR unit measuring cone at altitudes of 40 m, 60 m, 80 m and 100 m above the unit's reference window, in relation to the UAV data collection hover site. – Source: Google Earth 2020.*

unit's scanning cone. The selected site was retained for all data collection flights throughout the measurement campaign, independent of the wind direction at the time of each flight. This approach was adopted since changing the hover site based on the wind direction at the time would have resulted in a different underlying terrain topography for each different site, resulting in potentially different localized wind flow fields.

5.1.2 Site for Sheltered Data Collection Flights

Further to the open field data collection flights, it was also considered necessary to conduct a number of flights without the effect of any external wind disturbances acting on the UAV. A set of indoor flights were therefore carried out at the Main Exhibition Hangar at the Malta Aviation Museum, shown in Figure 5.3, in the central Maltese location of Ta' Qali. It was anticipated that such indoor flights would be deprived of a suitable GPS signal necessary to stabilize the aircraft in hover. It also transpired that a suitable GPS signal, was necessary for the UAV flight controller to be able to compute the UAV's horizontal speed. Since the horizontal speed was not recorded during the indoor flights, and since it is a necessary parameter to validate the data points used for the analysis of this study (as explained in section 5.4.1), it was decided that a set of

Figure 5.3: *Main Exhibition Hangar – Malta Aviation Museum at Ta' Qali, Malta. – Source: Google Earth 2020.*

flights be conducted in another sheltered location where a stable GPS signal can be received by the flight controller.

Such flights were therefore carried out within the courtyard of St. Sebastian's Pastoral Centre in the central Maltese town of Qormi (Figure 5.4). The location was preferred for its highly symmetric octagonal shape with approximately 17.5 metres across

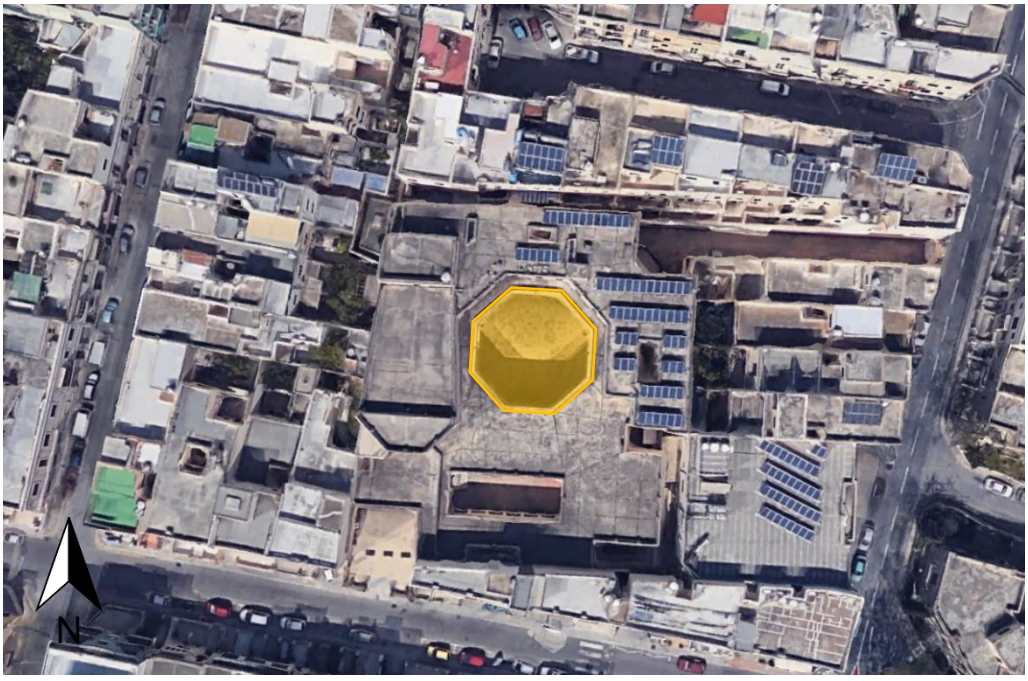

Figure 5.4: *Sheltered octagonal courtyard at St. Sebastian's Pastoral Centre in Qormi, Malta – Source: Google Maps 2020.*

Figure 5.5: *The hexacopter UAV during one of the sheltered flights.*

corners, and high surrounding walls shielding the courtyard space from atmospheric air currents. Furthermore, this site enjoys added shielding on the North, West and East sides offered by an additional storey built at rooftop level, shielding it from the prevailing *Majjistral* winds. Figure 5.5 shows the hexacopter UAV in hovering flight during one of the sheltered data collection flights.

5.1.3 Tied Down Testing Site

To complement the sheltered flights conducted at an altitude of five metres above ground, a set of UAV Tied down tests were also executed. Since these tests were ground-based, these tests also included the logging of wind data with the UAV powered down, and hence no consequent rotor influence. These tests were carried out in an open space at another site in Qormi approximately 0.5 km WNW of the site for sheltered flights. The tied down test site measured approximately 6.5 m long by 6.5 m wide and is protected by a 1 m high boundary wall on the south and east sides, a 3 m high wall on the north side and a 7 m high wall on the west side. The setup used is shown in Figure 5.6.

5.2 UAV Operations Permit

The operation of UAVs in the Maltese islands requires authorization from the relevant authorities; especially in view of the fact that all of the airspace over the Maltese islands is controlled airspace [104]. It should be noted that over the duration of this study there were substantial developments in the setting up of harmonized legislation

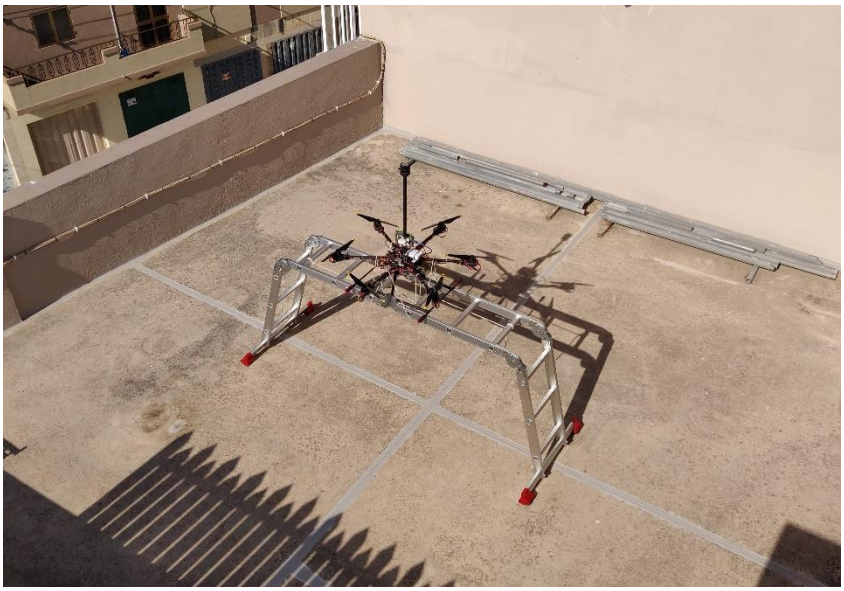

Figure 5.6: *A bird's eye view from the North East of the setup used for tied down testing. The south boundary wall and west wall of the testing site in Qormi, are also visible behind the test setup. The test was setup at a distance of 3.25 metres from the west wall.*

across the EU territory governing the sector of drone operations. Incidentally, these regulations [105, 106] were due to come into force on 1 July 2020 but their introduction was eventually postponed to 31 December 2020. Prior to this date the requirements to operate a drone were the domain of the local authority. The requirements to operate a UAV in the Maltese islands were set out in the '*Self Declaration for the Safe Operation of Drones'* [107], issued by Transport Malta – Civil Aviation Directorate (TM-CAD), as the authority responsible for such operations. Amongst other limitations that these requirements set out, this document limited the operation of such UAVs to a maximum altitude of 60 m above the ground. This altitude was too restrictive for the purposes of this study and a maximum operational altitude of 120 m was duly requested and exclusively granted by TM-CAD for the operations at the identified Ċirkewwa coastal site.

5.3 UAV Data Collection Flights

Data collection flights with the custom-built quadcopter UAV were carried out from the Ċirkewwa site on several days in April 2019. As a preliminary study, all flights were conducted at an altitude of 86 m above ground level, equivalent to 80 m above the ZephIR LiDAR measurement window (Appendix A). For this part of the study three individual 6000 mAh 6S LiPo batteries were used for these flights.

Following the incident reported in section 4.2 above, and the eventual build of the hexacopter UAV, data collection flights resumed from the Ċirkewwa site between December 2019 and March 2020 (Appendix A). The flights with the hexacopter UAV were conducted at four different altitudes, namely 40 m, 60 m, 80 m and 100 m above the ZephIR LiDAR measurement window. These altitudes were purposely selected to be coincident with four heights at which LiDAR wind measurements were being measured and logged. One of the battery packs used in the preliminary study was damaged in the quadcopter incident. A replacement battery pack was sourced and for the second phase of the study using the hexacopter UAV, a complement of three individual 6000 mAh 6S LiPo batteries were used.

Following the data collection campaign at the Ċirkewwa site, a number of control flights were conducted in sheltered locations at the Ta' Qali and Qormi sites between May 2020 and July 2020. The objective of these flights was to establish whether the readings of the ultrasonic wind sensor installed onboard the UAV were being biased or affected in any way by the induced flow field of the UAV rotors.

5.3.1 Precautionary Measures

The nature of this study entailed the operation of a UAV in the open field. As with all machinery, as well as evidently demonstrated by the quadcopter UAV incident during the course of this study, components and systems may fail in operation. Such an event may result in undesirable consequences, such as potential damage to third party property, as well as injury to the UAV operator and third parties. Being fully aware of the risks brought about by such operations, an appropriate risk assessment was drawn up giving due consideration to each of the associated risks. Any possible mitigation measures identified during the risk assessment exercise were duly implemented to maximize the operational safety of the UAV flights associated with this study.

It should also be highlighted that prior to conducting flights with the research UAVs, pilot training was carried out with a Syma X5C toy quadcopter. This particular model was selected as this has a radio control unit which is very similar in configuration and layout to the FrSky Taranis X9D plus used to operate the research multirotors built specifically for this study.

5.3.1.1 Test Flights

With both multirotors being new custom builds specifically designed for this study, each UAV was paced through a set of test flights so as to ensure its proper performance and stability while in flight. Test flights were carried out with the bare platform, as well as with dummy weights, to simulate the detachable components and subsystems of the sensor suite payload. In each case, test flights were first carried out at a low altitude of 10 m, gradually increasing the altitude to a maximum of 100 m. Once it was established that the multirotors performed satisfactorily with the full simulated payload, the remaining components and sensor suite subsystems were fitted, and a final test flight was executed.

5.3.1.2 Weather Monitoring

Although weather forecasting nowadays is continuously improving in accuracy, due to the stochastic nature of the weather, it was still a challenge to plan flights well in advance. This was further compounded by the necessity to abide with the operational restrictions imposed by the flight operations permit issuing authority and other restrictions imposed by the issuer of the insurance policy covering the UAV operations at all times. A preliminary decision to proceed with data collection flights was usually taken on the eve of the planned flights, based on the most recent weather forecast available.

The weather forecast for the day of the data collection flights at the flight operations site was checked at www.windfinder.com, and recorded a day in advance. This weather forecast is based on the Global Forecast System (GFS) model by the National Oceanic and Atmospheric Administration (NOAA). Other weather forecast models that were consulted to closely monitor the developing weather situation were the European Centre for Medium-Range Weather Forecasts (ECMWF) model, the METEOBLUE model and the ICOsahedral Nonhydrostatic-EU (ICON-EU) model by Deutscher Wetterdienst (DWD) available at www.windy.com. This procedure was once again repeated on the morning of the UAV flight operations day, prior to departing for the operational site. On arrival at the site the ZephIR LiDAR data were checked for the real-time wind speed and direction and based upon this information, a final and definitive decision on whether it was safe to proceed with the flights or not was taken. The intention was to postpone UAV operations in the eventuality that real-

time conditions showed sustained wind speeds at the operational altitude in excess of 10 m/s. Nevertheless, there were occasions when planned flights had to be cancelled on arrival at the site as the weather would have deteriorated to the point that it was unsafe to proceed with the UAV flights.

5.3.1.3 UAV Pre-flight Preparation and Checks

Due to the overall size of the UAV, the aircraft was transported with the propellers, wind sensor mast assembly and stand-alone environmental sensor removed. On arrival and confirmation that weather conditions were appropriate for flying, the multirotor UAV was fully assembled and subjected to an intensive pre-flight check, in accordance with a prepared pre-flight checklist (Appendix B).

Prior to powering-up the UAV, all critical fasteners of the UAV structure and those holding the motors in place were checked. This was followed by a check of the power distribution cabling supplying power to current sensors, ESCs, Flight Controller and Wind Sensor. Cabling from ESC connections to propeller motors, ESC signal cables to Flight controller, Radio receiver SBUS signal cable to Flight controller and Smart Port sensors cabling were eventually checked. At this stage a CoG position check was carried out to ensure that the CoG of the aircraft was at its geometric centre.

Having confirmed that all cabling was properly and securely connected, the multirotor UAV and Radio transmitter were powered-up and an LED status indicator check of the various onboard systems and components was carried out. This included the Global Navigation Satellite System (GNSS) antenna, Flight Controller, Radio Receiver, ESCs, Current Sensors, Variometer, GPS receiver and RPM sensors. The Arduino Data Logger system and iMet-XQ2 sensor were subsequently powered-up and the reception of a stable GPS signal on both systems was confirmed.

The UAV's Flight Controller compass was then calibrated and its home position set. Finally, the UAV Overall status indicator was checked and a visual check that the surrounding skies were clear carried out. At this point, the UAV was armed via the radio transmitter and each rotor checked for the correct direction of rotation, after which the UAV was throttled up for lift-off.

5.3.2 Flight Plan

5.3.2.1 Open Field Flights

As outlined in section 4.3, the study consisted of two distinct phases. During a series of test flights, it was established that the quadcopter UAV had an airborne autonomy of approximately sixteen minutes. Prior to every flight, the UAV was set up on the ground with a pre-set heading. The flight plan for each flight was to climb vertically to the desired altitude at the pre-set heading and to hover for seven minutes, The UAV was then yawed through 180° so that it was positioned heading in the opposite direction and kept in a hover at the same altitude for the remainder of the flight. When the pre-set battery low voltage threshold was reached, the DJI N3 flight controller automatically initialized the descent to an altitude of 20 m, at which altitude the UAV operator took over control of the vehicle and manually landed the aircraft.

Similarly, following a series of hexacopter UAV flight tests, it was established that the typical airborne autonomy of the research hexacopter UAV on a fully charged battery pack was of approximately eight minutes. In view of this it was considered more appropriate that for the second phase of the study, data collection with the hexacopter UAV was to be conducted at a fixed UAV heading, without executing any mid-flight yawing manoeuvres. This strategy allowed for a minimum uninterrupted data collection hover time of five minutes. As with the quadcopter UAV, the aircraft was kept in hover until the battery low voltage threshold was reached and the DJI N3 flight controller automatically initialized the descent.

5.3.2.2 Indoor Flights

Indoor flights with the hexacopter UAV were conducted at an altitude of 5 m above ground level at the Ta' Qali site. Since the UAV was operated indoors, these flights were conducted in the absence of a reliable GPS signal. Appropriate measures were therefore taken to ensure proper synchronization between data systems in the absence of a GPS timestamp.

In contrast to the open field (outdoor) flights, it transpired that maintaining a stable hover without a GPS signal for accurate positioning proved to be challenging. This was mitigated by trimming the aircraft controls during the first few indoor flights which were designated as test flights. The first such test flight was conducted with the

bare hexacopter platform (excluding the ultrasonic wind sensor and iMet-XQ2 environmental sensor) in order to gauge the UAV performance in an indoor setting. Having properly trimmed and established that the platform performed in a stable manner, a second test flight with the full sensor complement onboard was conducted whilst further fine tuning the control trims to counter for the added payload. Although hover stability was improved substantially over the duration of the initial two test flights, frequent corrections via the control inputs were necessary during the execution of the indoor flights.

As expected, since the flights were conducted in an enclosed, covered space, the UAV flight controller could not receive a stable GPS signal. Due to this limitation, during the post-processing of the flight controller data it was noticed that a series of parameters, including the UAV's horizontal speed components, were not logged. It transpired that a stable GPS signal was required for the flight controller to compute and validate an accurate estimate of the horizontal speed.

Attempts were made to extract a horizontal speed value for every data point, by integrating the accelerometer data using the trapezoidal rule. Unfortunately, the error in velocity over the duration of the flight was substantial, even when the accelerometer readings were corrected for X and Y accelerometer bias. In view of this, it was decided that it was more appropriate to execute data collection flights in a sheltered, outdoor environment when the atmospheric wind speeds were minimal. This would allow the flight controller to have access to a suitable GPS signal, and thus being able to compute and log the full parametric complement required for the data analysis.

5.3.2.3 Sheltered Flights

Outdoor sheltered flights were conducted at the Qormi site. Similar to the indoor flights, it was decided to conduct such flights at an altitude of five metres above ground level in order to minimize any ground effect phenomena as typically experienced by hovering aircraft. This was deemed to be a suitable altitude as the octagonal courtyard, shown in Figure 5.4, measuring 17.5 metres across corners, has an all-round perimeter wall nine metres high.

Initially the flight plan was to climb to the test altitude, hover in place without any heading changes until the low battery threshold was reached, and to eventually land the aircraft at the same spot used for take-off. During the execution of these flights, it

was found that a stable GPS signal could not be received at this altitude. In order to address this issue, the flight plan was therefore modified so that the initial climb was to an altitude of ten metres above the ground. The multirotor was then maintained at this altitude for a few seconds until a stable GPS signal was engaged and to then climb down to a data collection altitude of five metres. It was found that once the GPS signal had engaged, the UAV maintained a stable signal reception even after climbing down to the designated hover altitude of five metres. The UAV was then retained at hover at this lower data collection altitude for the remainder of the flight. When the low battery voltage threshold was reached the UAV was subsequently landed.

5.3.2.4 Tied Down Testing

As expected, the execution of these tests was not as complex as the airborne data collection flights described above. However, since the UAV was to be operated under tied down conditions, particular attention was given as to how the UAV was tied down. Tying down the UAV from its landing skids could have potentially damaged the UAV frame due to the substantial thrust generated by the six rotors. It was therefore decided to secure the UAV to the test rig from the propulsion arms. This avoided having to subject the UAV centre hub and landing gear to excessive stresses.

For this set of tests, once the UAV was powered up it was ensured that a stable GPS signal was being received, at which point the UAV propulsion system was throttled up. The UAV was left running until the flight controller triggered the UAV power down due to the battery reaching the low voltage threshold.

5.3.3 UAV Preparation

In order to minimize any variability in the UAV setup between flights, rotors were individually numbered and re-assembled onto the same motor for every flight. Similarly, during routine preventive maintenance inspections of the UAVs, replacement of any components was realized with exactly identical parts, to minimize aircraft configuration variations. Special care was taken when assembling or switching batteries between flights, to ensure that the battery power pack was always mounted in the same position and with the same orientation. This ensured that the CoG of the overall aircraft was affected as little as possible, both with respect to the overall weight, as well as in terms of the position of the CoG. Prior to every flight, a CoG position check was carried out to confirm that the CoG was coincident with the geometric

centre of the UAV. Nevertheless, since more than one battery pack was used, slight variations between batteries may still have been present.

5.3.4 Battery Preparation

As outlined in section 4.3.6, LiPo batteries are usually the most preferred battery technology used for powering UAVs. Unfortunately, this type of battery technology is very sensitive to charge levels, and leaving the batteries fully charged over long periods severely affects their lifetime. In order to preserve the battery packs as much as possible, the batteries were maintained at the optimal storage charge level of 40 % when not in use. In view of this, the batteries were only fully charged the day before any planned tests or data collection flights; a process which took approximately two hours for every battery power pack to charge from its storage charge level to fully charged. The power packs were not charged unless there was a sound possibility of conducting the flights. The reason was that the number of charging cycles also has an adverse effect on the power pack's capacity retention.

As soon as the flights were completed, the depleted batteries were immediately charged to the optimal storage charge level of about 40 %. Furthermore, the batteries were never discharged below the 25 % charge level as this potentially damages the battery cells irreversibly. This safeguard was accomplished via a voltage setting in the flight controller which triggered the landing of the aircraft when a minimum pre-set battery voltage was reached. In the event that flights were called off for any reason, the batteries were immediately discharged to the optimal storage charge level.

5.3.4.1 Battery Power Settings

Since the multirotor UAVs were being operated in relatively demanding conditions of above average wind speeds for such vehicle operations, the battery minimum voltage that triggered a landing of the UAV was set at a value higher than usual, in order to ensure that enough charge remained to accomplish a safe landing.

5.4 Data Synchronization

During the data collection flights, four independent systems discussed in section 4.4, logged data from an array of sensors. Each of these systems had a GPS timestamp. The GPS timestamp was used to synchronize the data from the different systems. Where possible the different systems were set to log data at a rate of 5 Hz. Unfortunately, the

DJI N3 Flight Controller and the iMet-XQ2 Environmental sensor ran proprietary scripts and the data logging frequency of these two systems could not be user-modified.

The Arduino-based data logging system specifically developed for this study, as well as the FrSky Taranis x9D PLUS integrated data logger, were both set to log data at the desired frequency of 5 Hz. The iMet-XQ2 Environmental sensor had a logging frequency of 1 Hz. In order to facilitate the synchronization of the data from this latter sensor with the data from the other systems during the post-processing phase, the original logs were expanded and four sets of readings between each of the logged readings were inserted. The inserted readings were linearly interpolated between the two logged readings bounding the set.

It was found that the GPS modules of the various systems used different data refresh frequencies and it transpired that on occasions, the GPS timestamp was not the most accurate method to synchronize the data. Incidentally, it was established that the most accurate way to synchronize the data from all the systems was to first synchronize the ultrasonic wind sensor and flight controller data using the GPS timestamp of the two systems. Since the DJI N3 Flight Controller logging frequency was approximately 30 Hz, the ultrasonic wind sensor data log was expanded such that the GPS timestamps of the wind sensor and flight controller data logs matched. Flight controller record entries that were missing a corresponding wind sensor record were omitted, which eventually resulted in a wind sensor-flight controller synchronized data log at a frequency of 5 Hz. The Radio System data logs were then synchronized to the flight controller data logs by matching the radio system throttle inputs, which were logged on both the radio system and flight controller data sets. This parameter proved to be accurate enough, and was cross-checked by also matching the Roll, Yaw and Pitch inputs. The iMet-XQ2 data log, which was expanded a priori to 5 Hz from the original 1 Hz data log as described earlier, was then synchronized to the wind sensor data's GPS timestamp.

5.4.1 Data Point Validation

For a proper UAV performance analysis of a multirotor in a stable hover condition it was first necessary to establish whether the collected data were sourced whilst the UAV was in a stable hover. Due to fluctuations in the GPS altitude and Variometer

altitude readings, it was difficult to establish whether the UAV was in a stable hover based only on these readings. It was therefore deemed necessary that the recorded data satisfied a number of criteria to ensure that the UAV was in a stable hover at the time of measurement of the relevant parameters. In order to achieve this, apart from UAV altitude, data points were also validated by:

- ***GPS signal status*** – the Flight Controller requires a stable GPS signal to compute an accurate UAV velocity.
- ***Radio signal status*** – the radio signal status confirms that the UAV was receiving a stable signal from the remote-control unit and hence under the command of the UAV pilot.
- ***Accelerometer measurements*** – Data points were evaluated depending on the logged value of the accelerometer in the Z-direction (vertical direction) as well as the X and Y directions. Data points were considered as valid if the Z-reading was close to 1 g, and the X and Y accelerations were close to zero. Such values indicated that the UAV was not accelerating in either the vertical or any of the horizontal directions. It should be noted that the X and Y readings would usually be slightly higher than zero since when the UAV was in a tilted attitude the accelerometer detected a small vertical component along these axes.
- ***Velocity measurements*** – The velocity readings for the X, Y and Z directions were also checked to validate the data points, as the UAV would have been in a stable hover when these readings were close to zero.

It should be noted that the resolution of the above parameters with respect to the azimuthal plane was not considered to be necessary as attitude angles throughout the study were minimal. In view of this the consequent difference between the absolute and the resolved values would therefore also be minimal.

A constant velocity in any of the X, Y and Z directions implies that the forces acting on the UAV are in equilibrium and that theoretically no extra power is demanded by the UAV. Nonetheless, any significant UAV velocity would have affected the wind speed readings of the onboard sensor which would therefore affect the wind data correlation study with the ground-based LiDAR unit.

5.5 Geomagnetic Declination

When a magnetic compass is held horizontally, it aligns itself with the horizontal component of the Earth's magnetic flux lines at the location at which it is being utilized. Due to the phenomenon that Earth's magnetic North Pole and the geographic North Pole are not coincident, all magnetic compass readings need to be adjusted to read with reference to Earth's geographic North Pole, more commonly referred to as True North. Furthermore, Earth's Magnetic North is in constant movement with respect to Earth's True North. The adjustment between magnetic North and True North is referred to as Geomagnetic Declination and is dependent on the calendar date, location on the globe and altitude above mean sea level.

The International Geomagnetic Reference Field (IGRF) model was used to establish the declination values for the purposes of this study. Since the UAV was operated at varying altitudes, it was also confirmed that the variation in altitudes, namely between 60 m and 120 m above mean sea level at which the UAV was operated, does not give rise to changes in the magnetic declination. Declination values were checked for all the days on which the UAV data collection flights were executed. The respective values have been provided in Appendix A.

5.5.1 Magnetic Compass Heading Adjustment

The research UAVs' sensor suites logged compass headings from two independent systems, namely the flight controller and the ultrasonic wind sensor, whilst another compass heading was logged by the ZephIR LiDAR wind measurement unit. The ZephIR LiDAR wind direction readings were recorded with respect to the unit's orientation. At post-processing stage the unit's bearing was adjusted to True North, which was subsequently used to adjust the wind direction measurements to True North.

The flight controller heading readings were automatically adjusted for geomagnetic declination between Magnetic North and True North by the flight controller itself. Unfortunately, these were adjusted with an arbitrary declination value of 2.96°. It is evident from the values provided in Appendix A that the declination values over the duration of the open field data collection campaign varied from 3.222 45° East to 3.329 09° East. Therefore, the yaw angles for the flight controller data set were re-adjusted using the more accurate declination values obtained from the IGRF model.

The ultrasonic sensor wind direction readings recorded during the quadcopter phase were recorded with respect to Magnetic North. These were consequently adjusted to read with respect to True North. During the hexacopter phase of the study the ultrasonic wind sensor was configured such that wind direction readings were measured and logged with respect to the sensor's datum, which was aligned with the aircraft's nose. Consequently, the wind direction with respect to True North was obtained by using the flight controller-logged aircraft heading, which had been previously adjusted to True North as described above.

6 Results and Analysis

The analyses detailed in this chapter includes a Wind Data Correlation study between the ground-based LiDAR measurement unit data and the multirotor onboard ultrasonic wind sensor data. This is followed by a multirotor performance analysis which includes a study on the battery voltage drop and the effect of wind speed on the UAV attitude angle. The scatter in UAV attitude records with respect to incident wind speed is also presented. An analysis of the relation between PWM-Voltage weighted duty cycle and the power delivered is then carried out. The chapter concludes with a study of the effect of wind speed and air density on the power consumption of the multirotor and on the power differential between diagonally opposite rotors of a multirotor UAV.

After each session of data collection flights, the data collected were downloaded and post-processed in preparation for an eventual in-depth analysis. At this stage it is important to highlight that the UAV performance parameters during the climb and descent phases of each data collection flight, to and from the hover altitude, were not considered in this analysis as these are beyond the scope of this study. Nevertheless, data for these phases of flight were nonetheless recorded in the same detail as that collected during the hover phase.

As detailed earlier, the first phase of the study was conducted using a quadcopter UAV platform. During this phase of the study the LiDAR was not operational, consequently LiDAR data for the quadcopter phase of the study are not available, and hence a wind correlation analysis was conducted solely for the hexacopter phase.

Furthermore, it should also be highlighted that wind measurements collected by the quadcopter-mounted ultrasonic wind sensor were a moving average of the preceding sixteen wind measurement readings, equivalent to a three-second moving average. This constitutes a significant difference in the way that wind measurements were collected by the ultrasonic wind sensors onboard the quadcopter and hexacopter multirotor UAVs. On the other hand, the hexacopter-mounted ultrasonic wind sensor measurements were instantaneous measurements of the wind conditions at the time.

6.1 Regression Tools

During the analysis of the gathered data from the open field data collection flights, it was noticed that a number of 'outlier' data points were present. This was to be expected especially, due to the stochastic nature of both the parameters being recorded as well as the environment under which the operations were carried out in the open field. It was deemed beneficial to use techniques such that these outlier data points did not negatively affect the data analysis being carried out.

A standard least squares approach was adopted for the regression analysis pertaining to the wind correlation studies. This approach was used for both the wind speed and wind direction regression analysis.

For the multirotor performance regression analysis detailed in this chapter, it was deemed more appropriate to use the Bi-Square weighting technique [108]. When a curve or surface is being fitted to an experimental data set the method minimizes the weighted sum of squares of the differences between the logged data points and the fitted function, or residuals [109]. As the residual value increases, indicating that the data point is further away from the fitted function, it is assigned a lesser weight. For points which are deemed to be substantially distant from the fitted function, these are assigned a weight of zero, thereby resulting in such outlier data points being completely eliminated from the regression exercise.

It should also be emphasized that prior to the regression exercise utilizing the bi-square weighting method, the data sets for this study would have already been subjected to a data validation process in order to establish the validity of each data point as described in section 5.4.1.

6.2 Incident Wind during Flight Operations

As outlined in sections 4.4.3.1 and 4.6, two independent instruments were used to collect the wind data at the operations site. The LiDAR unit, which is a ground-based remote wind measurement device, was installed on the rooftop of the WSC premises and the unit logged wind data continuously. This unit was operational during the hexacopter phase of the study. The ultrasonic wind sensors mounted on each of the multirotor UAVs, logged wind data whilst the UAV was in flight. Wind rose plots of the incident horizontal wind as measured by the ultrasonic wind sensors, during the

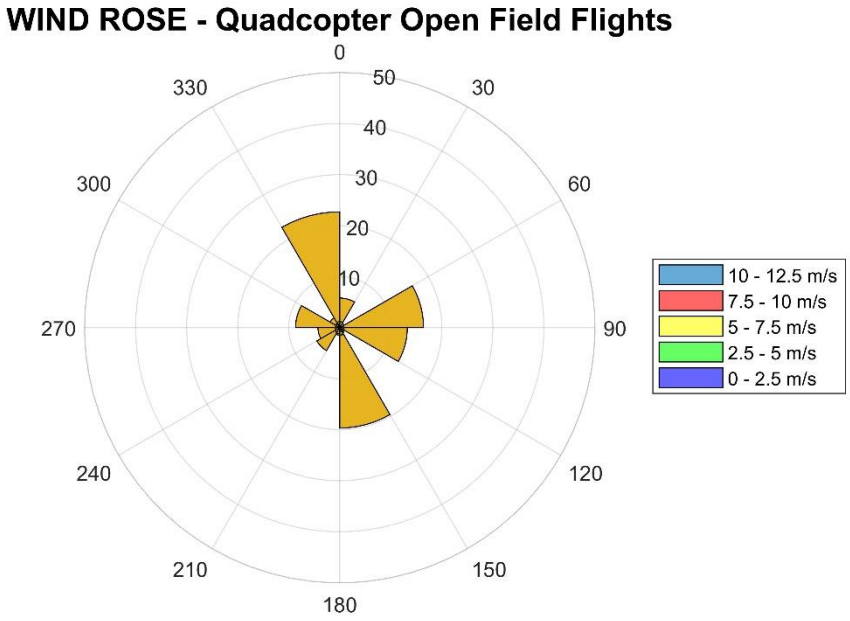

Figure 6.1: *Wind rose plot for incident horizontal wind WRT UAV heading as measured by the quadcopter UAV-mounted ultrasonic wind sensor during hover operations.*

execution of the quadcopter and hexacopter UAVs' data collection flights are shown in Figure 6.1 and Figure 6.2 respectively.

Due to the different nature of the two instruments, the wind data from each unit were logged at a different frequency. The ultrasonic wind sensor logged data at a consistent frequency of 5 Hz, whilst the ZephIR LiDAR wind measurement unit logged wind data at the operational altitude, at an approximate rate of two readings per minute. Due to the substantial discrepancy between the logging frequencies, it was impractical to study the correlation between individual wind data readings. In view of this, for a correlation study of the data from the two instruments, each LiDAR reading was compared to the average of the corresponding logged data from the ultrasonic wind sensor over the time interval between the concurrent LiDAR reading and the reading preceding it.

The wind direction averaging computation was weighted with the respective wind speeds using Eq. (6.1). This led to the value of wind direction computed over the averaging range to be the equivalent of the wind direction at the averaged wind speed.

$$\bar{\theta} = \arctan\left(\sum_{i=1}^{N} V_{\infty_i} \sin\theta_i \Big/ \sum_{i=1}^{N} V_{\infty_i} \cos\theta_i\right) \tag{6.1}$$

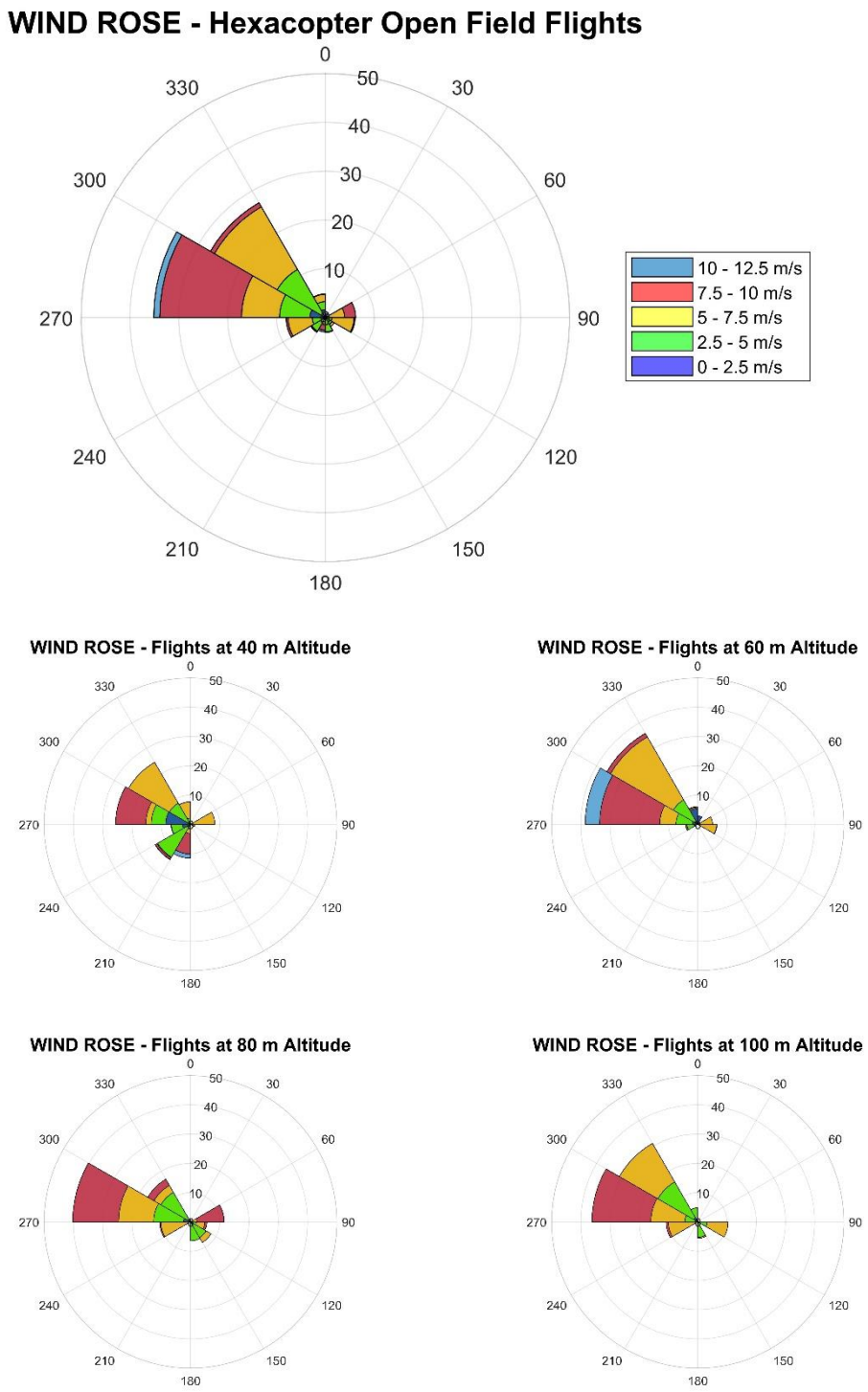

Figure 6.2: *Wind rose plots for incident horizontal wind WRT UAV heading as measured by the hexacopter UAV-mounted ultrasonic wind sensor during hover operations.*

It should also be noted that as a convention, for this study, all wind direction readings quoted throughout this dissertation have been adjusted to read with respect to True (geographical) North, as described in section 5.5.1, unless specified otherwise.

6.3 Wind Measurement Correlation

As already highlighted in section 1.4.1, one of the objectives of this study was to establish whether the wind data measured and collected by a UAV mounted wind sensor can be reliably considered as a true measure of the actual wind conditions at the location of the sensor. To establish whether this hypothesis holds true, plots of the wind speed and respective wind direction from both the LiDAR measurements and the onboard ultrasonic wind sensor were prepared. The correlation between the two sets of readings for the hexacopter phase of the study could then be determined.

6.3.1 Wind Speed Correlation

A plot for the wind speed measured by the UAV mounted ultrasonic wind sensor with respect to the LiDAR wind measurement unit readings for wind speed is shown in Figure 6.3. The plot indicates that there exists a relatively strong correlation between the two independently logged data sets, as indicated by the R-squared value shown in the accompanying table.

After having segregated the collected data points by flight altitude it was found that the strong wind speed correlation was consistent across the four different flight

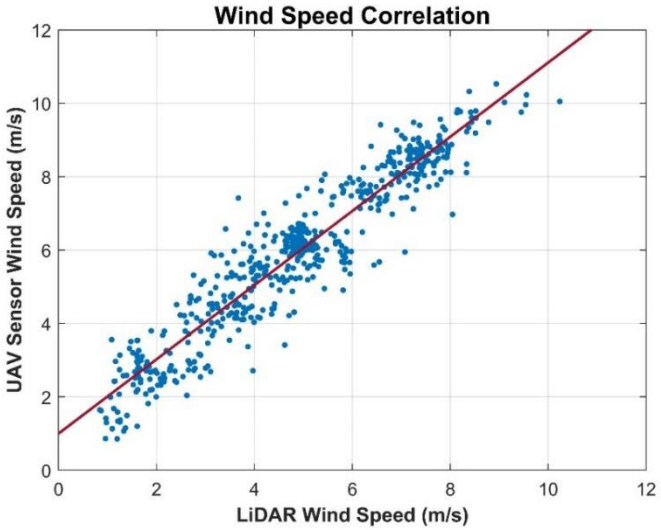

Data set	Model	No. of Data Points	R^2	RMSE *(m/s)*
All	$V_{UAV} = 1.01V_{LID} + 1.00$	573	0.896	0.702

Figure 6.3: *Hexacopter UAV-mounted ultrasonic sensor wind speed measurements with respect to LiDAR wind speed measurements.*

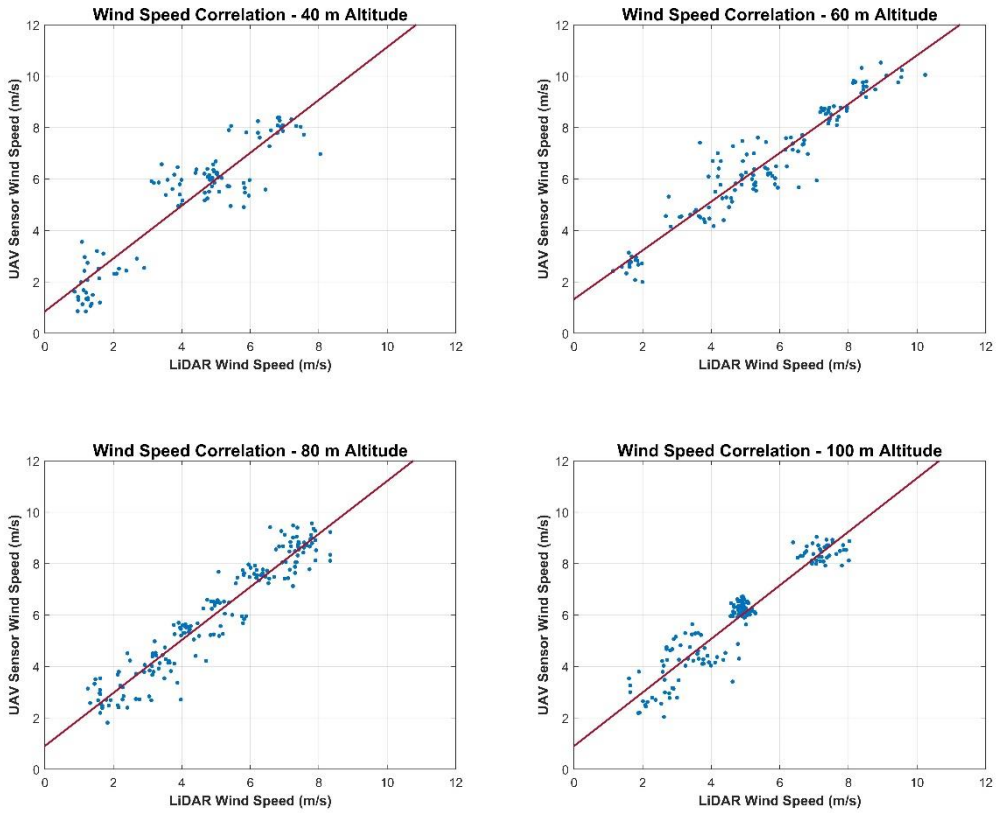

Data set	Model	No. of Data Points	R^2	RMSE *(m/s)*
40 m	$V_{UAV} = 1.03V_{LID} + 0.85$	105	0.852	0.890
60 m	$V_{UAV} = 0.95V_{LID} + 1.33$	134	0.907	0.677
80 m	$V_{UAV} = 1.03V_{LID} + 0.91$	176	0.912	0.657
100 m	$V_{UAV} = 1.04V_{LID} + 0.90$	158	0.892	0.623

Figure 6.4: *Hexacopter UAV-mounted ultrasonic sensor wind speed measurements with respect to LiDAR wind speed measurements, segregated by operational altitude.*

altitudes at which wind speed measurements were taken. This is demonstrated in the plots for the segregated data by flight altitude shown in Figure 6.4. It is interesting to observe that the RMSE decreases progressively as the altitude increases. This is indicative of an increasingly homogenous wind flow field as the altitude increases, potentially due to the decreasing influence of the different ground topography between the LiDAR site and the UAV hovering site.

6.3.2 Wind Direction Correlation

Similar to the wind speed correlation analysis, in order to establish the correlation strength between the wind direction readings from the two independent instruments, a

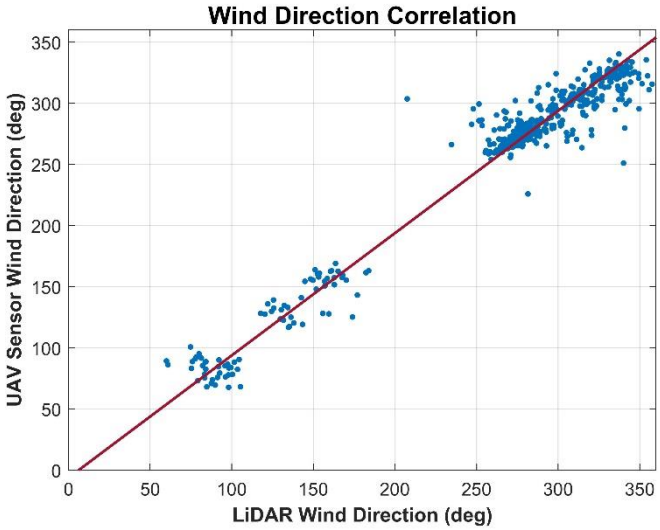

Data set	Model	No. of Data Points	R^2	RMSE (°)
All	$\theta_{UAV} = \theta_{LID} - 6.16$	573	0.951	14.19

Figure 6.5: *Hexacopter UAV-mounted ultrasonic sensor wind direction readings with respect to LiDAR wind direction readings.*

plot for the ultrasonic wind sensor wind direction readings with respect to LiDAR wind direction readings is shown in Figure 6.5 for data across all hovering altitudes. A series of plots for wind direction data segregated by hovering altitude was also prepared and has been provided in Figure 6.6. These plots indicate that the strong and consistent correlation found in the wind speed data from the two instruments is also present in the wind direction data across the four different flight altitudes at which data were collected, as demonstrated by the consistently high R^2 values shown in Figure 6.6.

As observed during the wind speed correlation analysis it has been noticed that the RMSE follows the same pattern and decreases progressively as the UAV operational altitude increases, potentially due to the ground topography influence as highlighted earlier.

Having established the correlation between the wind direction recorded by the LiDAR wind measurement unit and the hexacopter UAV mounted ultrasonic wind sensor, it was interesting to analyse whether the correlation is consistent across the full range of wind speeds. A plot of wind direction delta as the wind speed increases was prepared and presented in Figure 6.7, to enable analysis of the variation in the wind direction correlation across wind speeds. The generated scatter plot indicates that as the wind

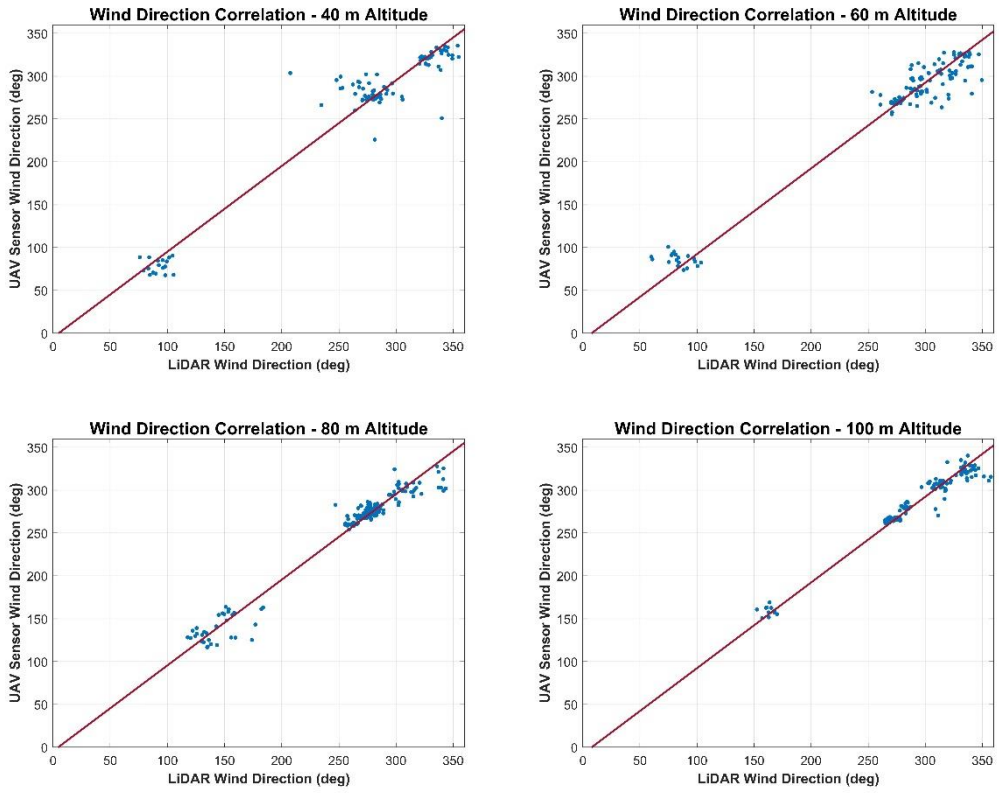

Data set	Model	No. of Data Points	R^2	RMSE *(°)*
40 m	$\theta_{UAV} = \theta_{LID} - 4.84$	105	0.937	20.96
60 m	$\theta_{UAV} = \theta_{LID} - 7.57$	134	0.957	15.44
80 m	$\theta_{UAV} = \theta_{LID} - 4.5$	176	0.960	11.34
100 m	$\theta_{UAV} = \theta_{LID} - 7.69$	158	0.949	9.46

Figure 6.6: *Hexacopter UAV-mounted ultrasonic sensor wind direction readings with respect to LiDAR wind direction readings, segregated by operational altitude.*

speed increases, the wind direction readings of the two measuring instruments align closer to each other.

It was observed during the wind speed correlation analysis that the ultrasonic wind sensor readings are characterized by a positive bias. A minor discrepancy between the wind direction readings of the two instruments was also observed. The ideal method to establish whether the discrepancies in instrument readings were partially or fully caused by the UAV rotor-induced velocity, would have been to fly the UAV indoors in stable hovering conditions. As described in section 5.3.2.2, although this approach was indeed attempted, it was found that this was not a viable solution due to the lack of a GPS signal reception by the UAV systems.

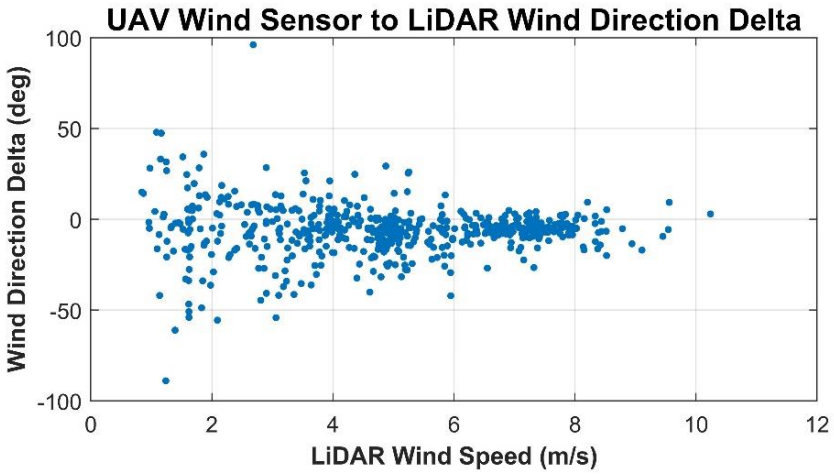

Figure 6.7: *Hexacopter UAV-mounted ultrasonic wind sensor to LiDAR wind direction delta with respect to LiDAR wind speed reading.*

An attempt to identify this bias was therefore made by making use of sheltered locations for flying the UAV as well as running the UAV under tied down conditions. In both scenarios tests were conducted on relatively windless days, so as to minimize as much as possible the influence of any external airflows on these bias identification tests.

6.3.3 Sheltered Testing

The objective of conducting UAV data collection flights in a sheltered location was to establish whether the wind measurements recorded by the onboard ultrasonic wind sensor were biased in any way by the rotor induced airflow during flight. In order to ensure that the UAV was not under the influence of the 'ground effect', these flights were conducted at an altitude of five metres above the ground. Wind rose plots for wind data measured by the hexacopter UAV mounted ultrasonic wind sensor across all flights, as well as segregated by individual flights are presented in Figure 6.8.

An analytical review of the wind rose plots, makes it apparent that the onboard ultrasonic wind sensor does indeed record an airflow during the course of each flight, although the lack of consistency in the wind direction between flights gives rise to the possibility that the recorded wind data may not be fully caused by the rotor induced airflow. Had this been the case a consistent wind direction would be expected. Potentially, the recorded wind data may be partially due to atmospheric wind conditions at the time of the tests. On the other hand, the mean recorded wind speed for each individual sheltered flight is relatively consistent as shown in Table 6.1.

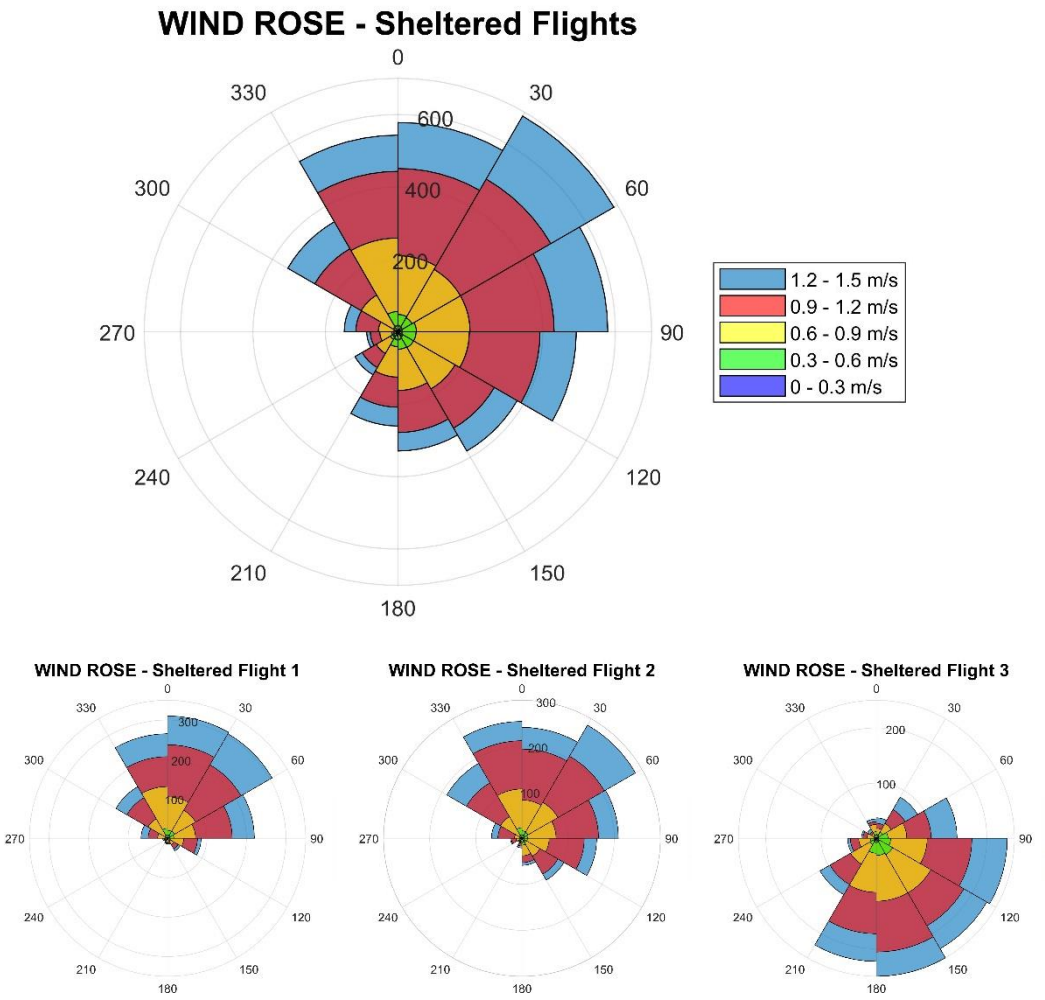

Figure 6.8: *Wind rose plots for flights conducted at an altitude of five metres above ground at the Qormi sheltered site. Wind direction readings are WRT to the hexacopter UAV.*

Due to the hovering altitude at which this flight set was carried out, it was not possible to record wind measurement readings at the five-metre hover altitude with rotors powered down.

Table 6.1: *Mean recorded wind speed for hexacopter UAV flights in sheltered location.*

Test Number	Mean Wind Speed *(m/s)*	Standard Deviation *(m/s)*
1	0.984	0.325
2	0.981	0.336
3	1.109	0.505
Combined	1.029	0.408

6.3.4 Tied Down Testing

Testing the UAV under tied down conditions potentially exposes the UAV-mounted ultrasonic wind sensor, to the most extreme UAV rotor induced airflow, as the rotors operate at almost maximum throttle. The UAV was tied down to a rig with its rotors sitting 1.2 m above the ground. The configuration of each test carried out in the tied down test sequence is described hereunder.

- ***Test 1*** **–** The UAV was powered up and the rotors were run at full power.
- ***Test 2*** **–** A second test was conducted with rotor 3 (coincident with a UAV bearing of 270°) disconnected, such that an airflow imbalance was created around the ultrasonic wind sensor.
- ***Test 3*** **–** The UAV ultrasonic wind sensor was powered up and data for a three-minute interval with the rotors powered down were logged to establish the wind conditions at the time.
- ***Test 4*** **–** Another test with the two adjacent rotors 3 and 4 (coincident with UAV bearings 270° and 210° respectively) disconnected was conducted, with the intention of generating a stronger airflow imbalance.
- ***Test 5*** **–** A second three-minute interval for the wind conditions at the time was then recorded, with all rotors powered down.

The ultrasonic wind sensor recorded data, obtained during each of the above tests are graphically presented in Figure 6.9 and Figure 6.10.

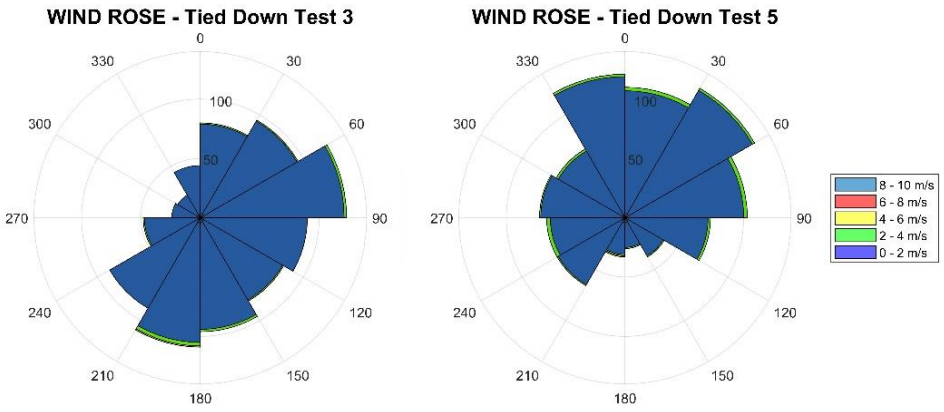

Figure 6.9: *Wind rose plots for two three-minute interval recordings of wind conditions during Test 3 (left) and Test 5 (right) of the tied down test sequence for the hexacopter UAV. Wind direction readings are WRT to the hexacopter UAV.*

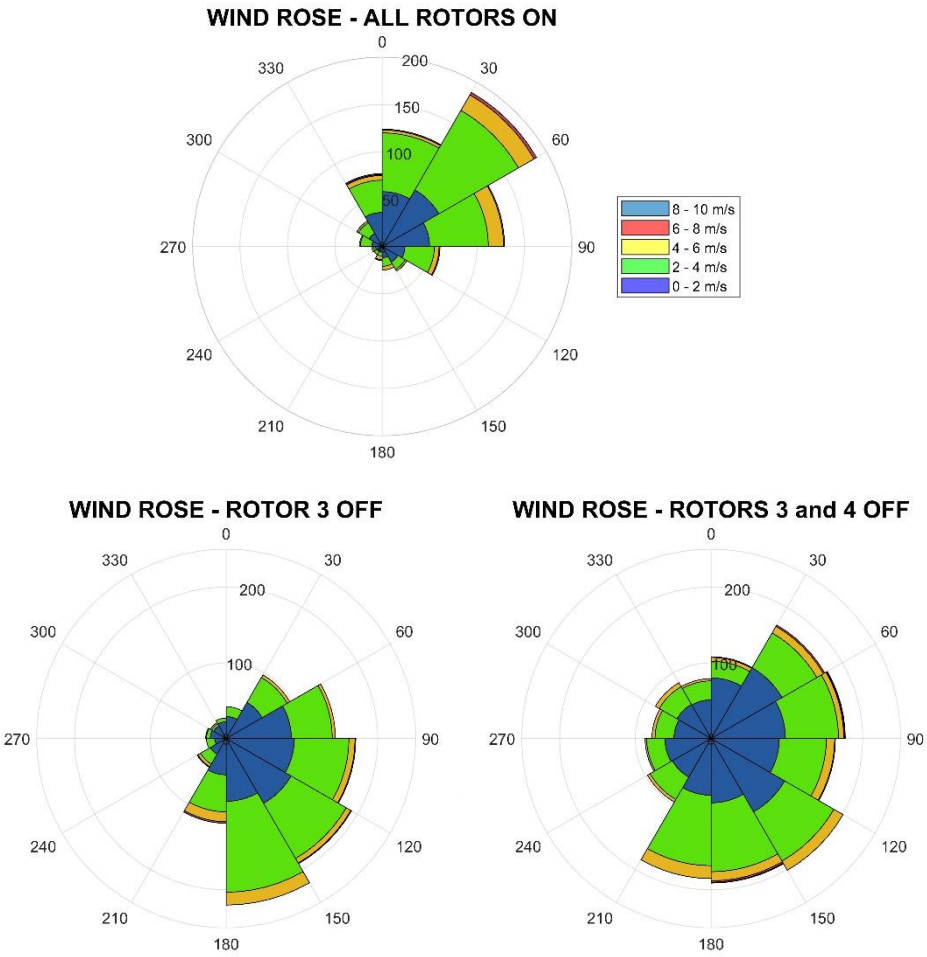

Figure 6.10: *Wind rose plots for hexacopter UAV tied down tests with all rotors powered up (Test 1) and with rotor 3 (Test 2) and rotors 3 and 4 (Test 4) disconnected. Wind direction readings are WRT to the hexacopter UAV.*

The data recorded during the two three-minute intervals with the UAV rotors powered down (Figure 6.9) indicate that the wind speed is relatively consistent, whilst the wind direction profile was different when comparing both tests.

When comparing the wind rose plots in Figure 6.9 for UAV tests with powered down rotors, with those in Figure 6.10, for UAV tests with rotors powered up, the recorded wind speed is evidently higher when the UAV rotors were powered up. This indicates that the induced airflow of the UAV rotors does have an effect on the UAV-mounted wind sensor measurements, when the UAV is in close proximity to the ground. From Table 6.2 the mean recorded wind speed with the UAV powered down was approximately 0.5 m/s, whilst the mean recorded wind speed with spinning rotors is closer to 2 m/s.

Table 6.2: *Mean recorded wind speed during hexacopter UAV tied down testing.*

Test Number	Flight Setup	Mean Wind Speed *(m/s)*	Standard Deviation *(m/s)*
1	All Rotors ON	2.350	1.271
2	Rotor 3 OFF	2.027	1.127
3	All Rotors OFF	0.474	0.446
4	Rotors 3 and 4 OFF	1.944	1.176
5	All Rotors OFF	0.506	0.527

There is also an initial indication that as more rotors are disconnected, the wind speed bias also decreases. Extra caution should be exercised in interpreting this observation as the available data are limited to just three instances, thereby demanding a more detailed analysis based on extended testing and data collection.

While analysing the wind direction recorded during these test flights, it was noticed that the recorded wind direction did not align with the powered down rotors. Incidentally, the wind direction profiles for test 2 and test 3, which were executed in rapid succession, seem to be substantially similar. This similarity, although potentially coincidental, indicates that the wind direction may have been affected by the atmospheric wind direction at the time.

It was expected that in test 2, more occurrences with a wind direction of approximately 270°, and in test 4, more occurrences of approximately 240° (midway between 210° and 270°) would have been recorded. The lack of proper alignment with the powered down rotors may indicate, as stated earlier in this section, that the recorded wind direction may have been influenced by the atmospheric wind conditions at the time.

Based on the above data, it may be confidently claimed that the recorded wind speed by the onboard ultrasonic wind sensor, does indeed possess a bias caused by the UAV's rotor-induced airflow when in close proximity to the ground. Nonetheless, it is considered that further research and dedicated testing are necessary to accurately establish such bias, under these conditions. On the other hand, indications are that the recorded wind direction may be less affected by the potential airflow imbalance, and more dependent on the incident atmospheric wind direction.

6.4 Multirotor Performance

The effect that incident horizontal winds have on the performance of the multirotor UAVs in hovering flight conditions was of primary interest for this study, as stated in section 1.4.1. An in-depth analysis of such performance has been detailed hereunder, utilizing a number of key parameters from the logged data. The main parameters used in this study and outlined in this dissertation are the following:

1. Wind Speed and Direction;
2. Air Density;
3. PWM Signal Average (average duty cycle of the motor PWM signals);
4. UAV Tilt Angle;
5. Power Consumption.

The values for wind speed and wind direction were sourced from the data logs of the FT205EV Ultrasonic wind sensors. The air density was calculated using the approximation given in Eq. (3.61), as described in section 3.4. The PWM signal average was calculated from the values of the PWM signals of each of the multirotor UAV motors as logged in the N3 flight controller data logs, whilst the UAV tilt angle was sourced from the same N3 flight controller data logs. The power consumption was calculated from the electrical current drawn by each motor and the potential difference across power pack terminals as recorded by the flight controller.

6.4.1 The Quadcopter Phase

The data for the quadcopter phase of the study were collected during five data collection flights, all of which were conducted at an altitude of 80 m above the LiDAR reference window (details provided in Appendix A). Following the trimming of data pertaining to the climb and descent phases of flight, and any other data pertaining to UAV manoeuvres outside the scope of this study, the data set contained a total of 20 075 data points. After each of these data points was validated as detailed in section 5.4.1, the valid ones were used for the in-depth analysis totalling 19 562 data points; equivalent to more than 65 minutes of quadcopter hovering time.

As highlighted earlier in this chapter, the quadcopter-mounted ultrasonic wind sensor measurements recorded during this phase of the study were based on a moving average of the preceding sixteen readings. Since data from this sensor were being logged at a

Table 6.3: *Data points for the analysis of the hexacopter UAV in hovering flight.*

Altitude *(m)*	No. of Raw Data Points	No. of Validated Data Points	Validated to Raw Data point ratio *(%)*	Equivalent Time *(min)*
40	18 175	17 638	97.0	58.8
60	18 350	17 986	98.0	60.0
80	17 825	16 752	94.0	55.8
100	19 075	19 053	99.9	63.5
Total	**73 425**	**71 429**	**97.3**	**238.1**

frequency of 5 Hz, this translated into the recorded data being an average of readings covering the preceding three-second interval. The use of a moving average recording technique resulted in the smoothing of the wind data from the quadcopter phase. In order to carry out a proper analysis, whenever other parametric data were to be analysed in conjunction with the ultrasonic wind sensor measurements, the data were first converted to a moving average covering an equivalent three-second interval.

A preliminary study based on an analysis of the data collected during the quadcopter phase was carried out by Scicluna et al. [110], which served as a precursor for the hexacopter phase of the study, and which established preliminary trends for the relationships between the various relevant parameters.

6.4.2 The Hexacopter Phase

The data used for the analysis of the hexacopter phase of the study have been sourced from an array of flights which have also been detailed in Appendix A. Ten data collection flights for each of the 40 m, 60 m, 80 m and 100 m altitudes above the LiDAR reference window have been conducted at the Ċirkewwa site. As was done with the quadcopter data, after the data were trimmed from data pertaining to any aircraft manoeuvres outside the scope of this study, including the climb and descent phases of flight, the remaining data points totalled 73 425. These data points were eventually validated as described in section 5.4.1. This yielded a total of 71 429 data points, equivalent to almost four hours of continuous hexacopter UAV hovering flight. The validated data points were distributed across the four operational altitudes as detailed in Table 6.3.

Since the ultrasonic wind sensor measurements from the hexacopter UAV-mounted sensor were real-time instantaneous readings, unlike those from the quadcopter UAV-mounted sensor, the following analysis of all the parameters from the hexacopter phase is based on instantaneous measurements from the 5 Hz data logs of the harmonized data set. This translates to logged measurements at regular intervals of 0.2 seconds.

6.5 Battery Voltage

The multirotor UAV performance analysis was commenced by observing how the battery voltage of the battery power pack fluctuated during the execution of the data collection flights.

The battery voltage of a LiPo battery is also used as a measure of the charge level remaining in the battery power pack. As the charge level of such a battery decreases, the battery voltage decreases commensurately. Figure 6.11 is a plot of the battery voltage for a typical quadcopter UAV data collection flight as it progresses through the various flight phases, namely arming of the UAV, take-off, climb, hover, descent and touchdown followed by the eventual power pack disconnection once the UAV is back on the ground.

The plots of battery voltage fluctuations for typical hexacopter UAV data collection flights conducted at different altitudes as the flights progress through the different flight phases are shown in Figure 6.12.

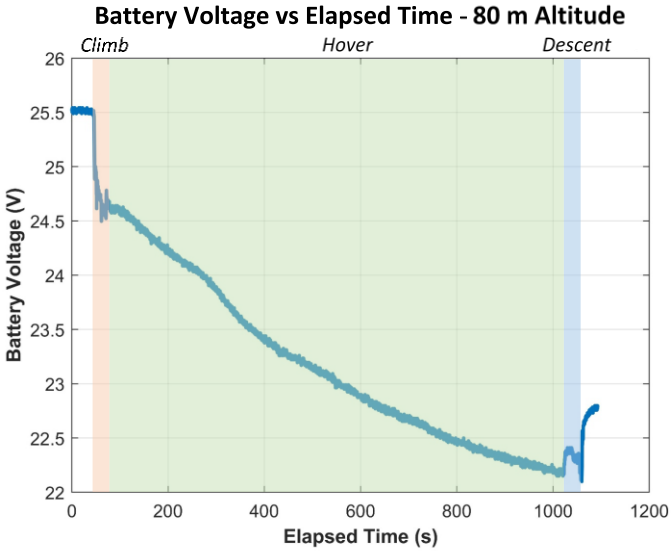

Figure 6.11: *Battery voltage decline versus time for a typical quadcopter UAV flight as the flight progresses through the 'Climb', 'Hover' and 'Descent' phases.*

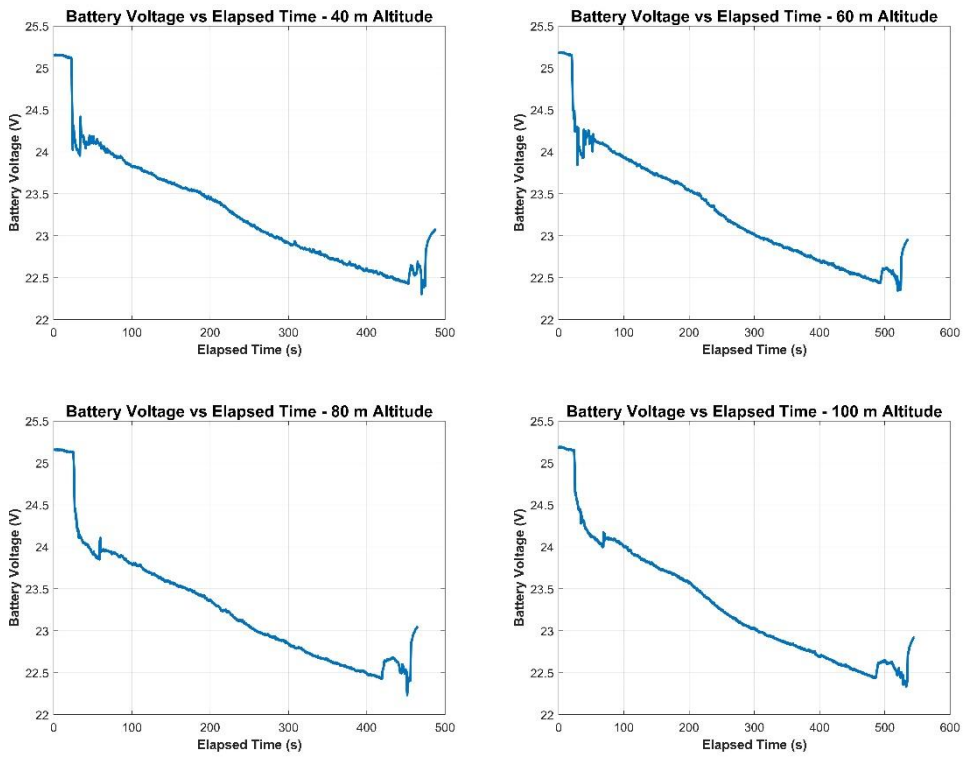

Figure 6.12: *Battery voltage decline versus time for typical hexacopter UAV flights at altitudes of 40 m, 60 m, 80 m and 100 m, as the flights progress through the various flight phases.*

It is evident from the quadcopter and hexacopter battery voltage plots that the drop in power pack voltage is very similar in all the cases being considered. One particular difference between the quadcopter and hexacopter flights is the slower voltage drop in the quadcopter battery voltage plots, which manifests itself as a difference in the time lapse between the commencement of the flight and the eventual touchdown of the aircraft. As expected, the hexacopter flights were shorter for the same battery power pack due to the increased power demand caused by the higher AUW of the hexacopter aircraft.

Starting with a fully charged battery when the UAV is armed, it is evident that the battery's voltage drops significantly during the climb phase of the flight. Once the aircraft reaches the designated altitude, the plots show a short period of irregular battery voltage fluctuations, brought about by a series of UAV operator correction inputs, whilst stabilizing the aircraft at the designated altitude. This is followed by a relatively smoother quasi-linear drop during the hover phase of the flight, which comprises most of the flight duration. During the descent phase, an increase in voltage is witnessed, brought about by a reduction in power demand, and consequently a

reduced current draw on the power pack. This induces a voltage bounce-back, which is typical of LiPo battery power packs. This is followed by a notable drop in pack voltage, coinciding with the increased power demand required to halt the descent just before touchdown. This is then followed by a large pack voltage bounce-back, triggered by the complete shutdown of the UAV propulsion system after the UAV touches the ground.

A comparison between the typical power pack discharge during a quadcopter flight and that of a hexacopter flight, shows a relatively higher bounce-back during hexacopter operations. This phenomenon is caused by a consistently higher current draw experienced by the power pack during hexacopter operations, which results in a lower power pack effective capacity. Incidentally, a lower current draw during the quadcopter operations results in the power pack being discharged more for the same set minimum voltage threshold, as the power pack maintains a higher voltage under load at the terminals, for the same level of charge. Such a higher pack voltage under load triggers the flight controller to initiate a descent at a lower charge level. Consequently, since the power pack has a higher residual charge after typical hexacopter operations when compared to quadcopter operations, the power pack voltage bounce-back is higher once the power pack is relieved of its electrical load. This has an adverse impact on the UAV flight endurance of hexacopter flights.

The overall flight duration of a multirotor UAV is a measure of the level of autonomy and flight endurance of the aircraft, which is very much related to the battery power pack capacity. The actual battery power pack capacity varies between different power packs of the same type, a characteristic which may be attributed to manufacturing differences between each individual power pack. Furthermore, actual power pack capacity is also a function of the battery's State of Health (SoH), which is dependent on a number of factors including the battery age, the number of charge cycles, and the discharge depth that the pack has been subjected to. An experimental study by Abdilla et al. modelling the endurance of battery-powered rotorcraft highlights the significance of this variability in the actual capacity of a battery power pack [74]. This characteristic of capacity fluctuation was also observed during the subsequent battery charging cycles that the power packs used in this study were subjected to, as these were recharged in preparation for multirotor flight operations. As described earlier in this section, the discharge rate of the power pack also has an effect on the capacity

delivered by the battery, as was evidently seen in the case of the quadcopter and hexacopter performances. This effect in LiPo power packs is also referred to as the 'capacity effect' [111]. It was therefore deemed that due to the bespoke reasons, the overall flight duration was not a suitable enough measure for analysis and that using such a measure would have adversely impacted the certainty of the results.

6.6 PWM Signal, Wind Speed and UAV Tilt

Three key parameters in the operation of a multirotor UAV are the PWM signal, which controls the power delivered to each UAV motor, the incident wind speed and the UAV tilt angle. Analysing the fluctuations of the PWM average signal during the course of a typical data collection flight showed that as the flight progressed, the PWM signal average increased progressively. This was also observed for both the quadcopter and hexacopter UAV operations, even in conditions of relatively constant wind speed. This is graphically demonstrated in Figure 6.13 and Figure 6.14, for 300-second intervals at which the quadcopter and hexacopter UAVs respectively were in a stable hover.

As discussed in section 6.5, it was demonstrated that during the course of the flight the power pack voltage decreased steadily. The PWM increase therefore indicates that in order to maintain the required amount of thrust throughout the duration of the flight, as the voltage declines, a higher PWM duty cycle is necessary to compensate for the power pack potential drop. The increased PWM duty cycle maintains the necessary RPM values, and consequently the thrust generated by the rotors of the multirotor UAV to maintain a stable hover.

The UAV XY Tilt angle peaks visible over the period plotted are indicative of wind perturbations affecting the UAVs' hover at the operations site. It is evident that these short duration peaks are not present in the wind data plot for the quadcopter study, predominantly due to the wind sensor's moving average filtering algorithm, which averages the last sixteen wind measurements for every reading. Nevertheless, these wind speed peaks are visible in the hexacopter plot, as the sensor onboard the hexacopter was configured to record the instantaneous values of wind speed and direction, without using a moving average algorithm. This proved to be beneficial during the analysis stage, as any wind gusts which affected the UAV performance were visible on the logged wind data. It is also more evident that, as expected, the peaks in

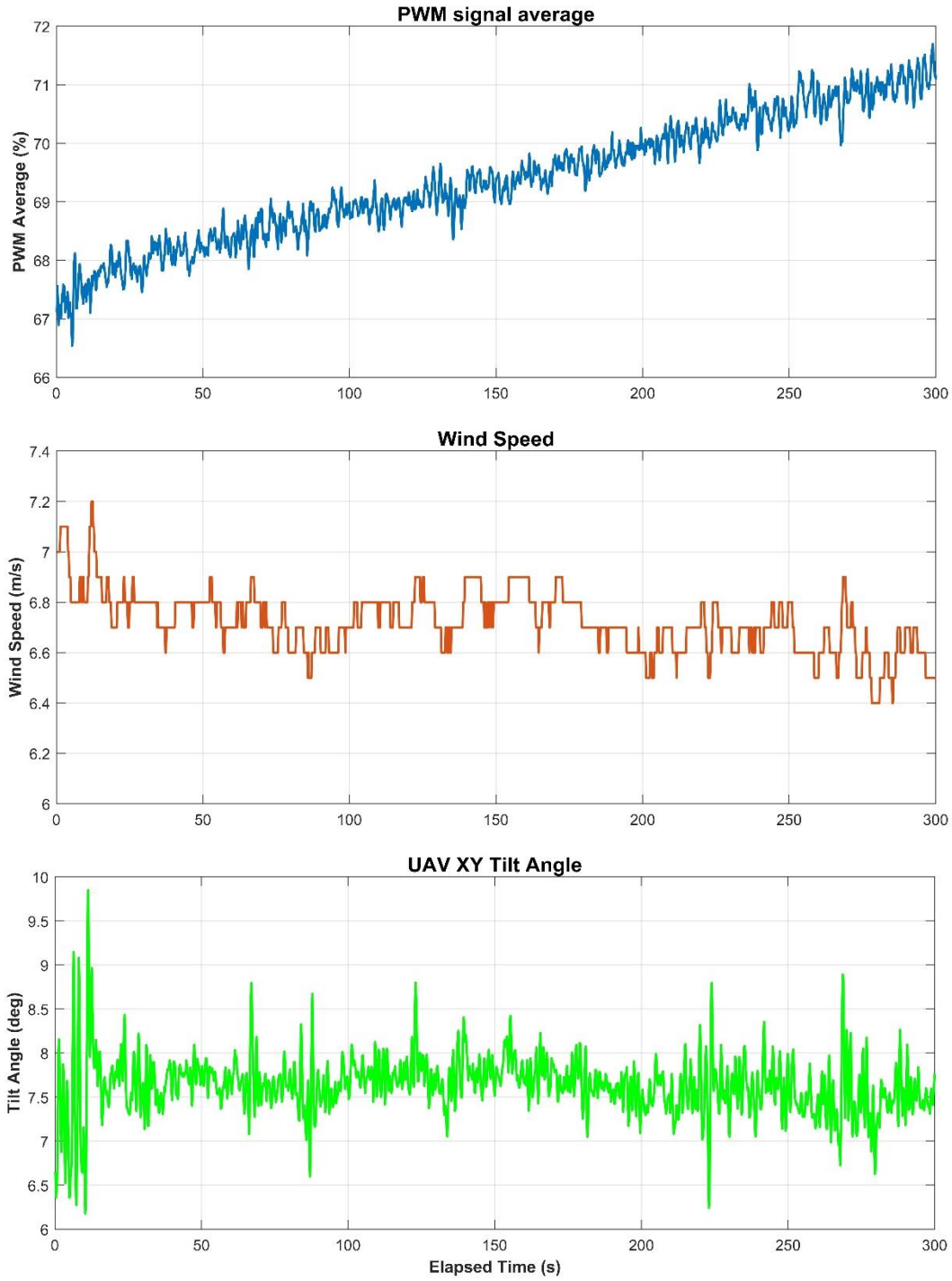

Figure 6.13: *Plots of PWM signal average, wind speed and UAV XY tilt angle versus time, over a 300-second interval during the hovering flight phase of a quadcopter flight.*

wind speed coincide closely with the peaks in UAV inclination for the hexacopter UAV plot. This is due to the UAV counteracting for the associated increases in wind speed by a commensurate increase in UAV tilt angle, required to maintain a stable hover.

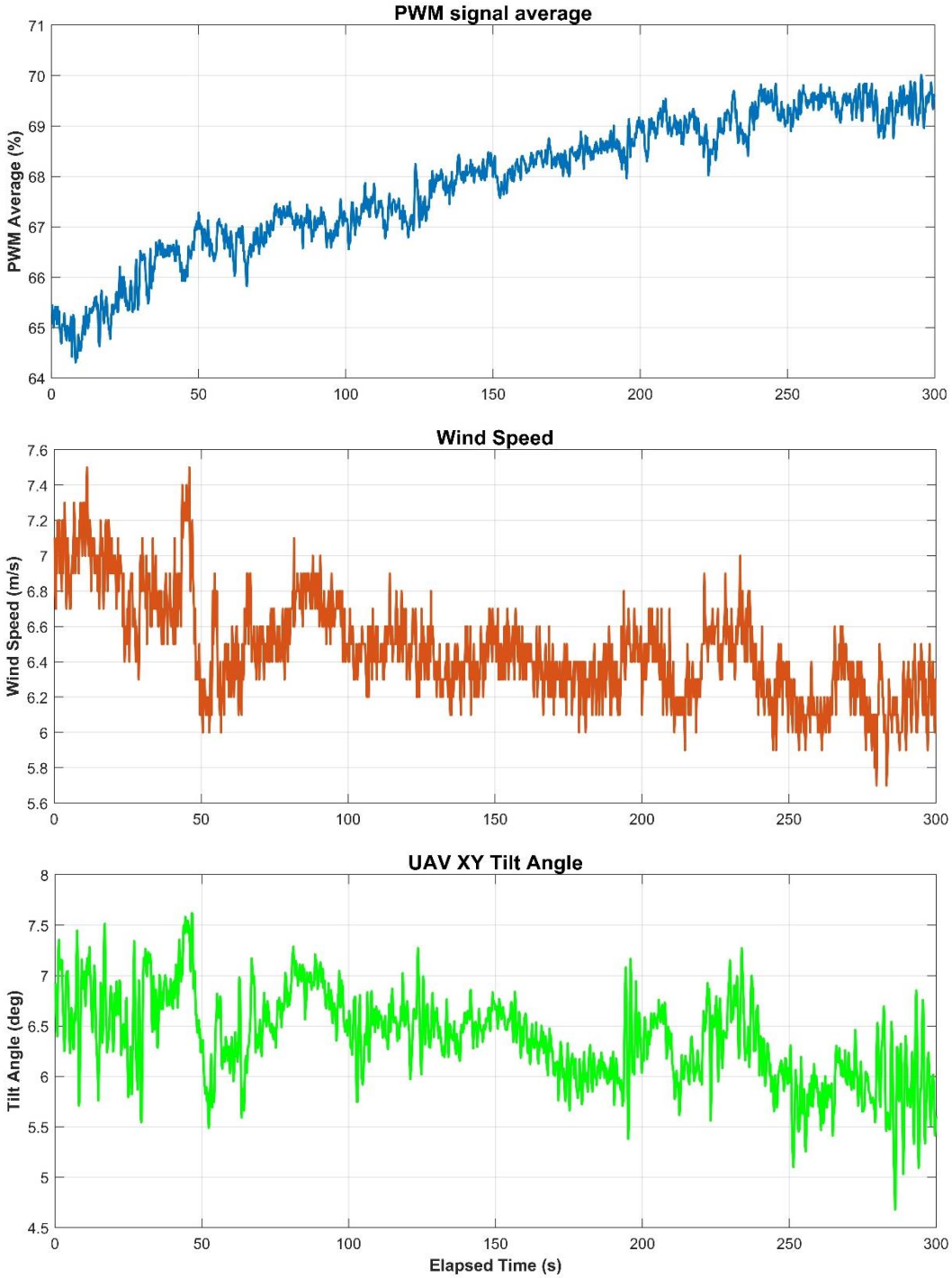

Figure 6.14: *Plots of PWM signal average, wind speed and UAV XY tilt angle versus time, over a 300-second interval during the hovering flight phase of a hexacopter flight.*

6.7 Impact of Incident Wind on UAV Attitude

As described in section 3.1 earlier in this dissertation, as a hovering multirotor UAV in incident horizontal wind conditions starts experiencing translational motion, due to the incident wind, the Flight Controller adjusts the attitude of the UAV. Consequently,

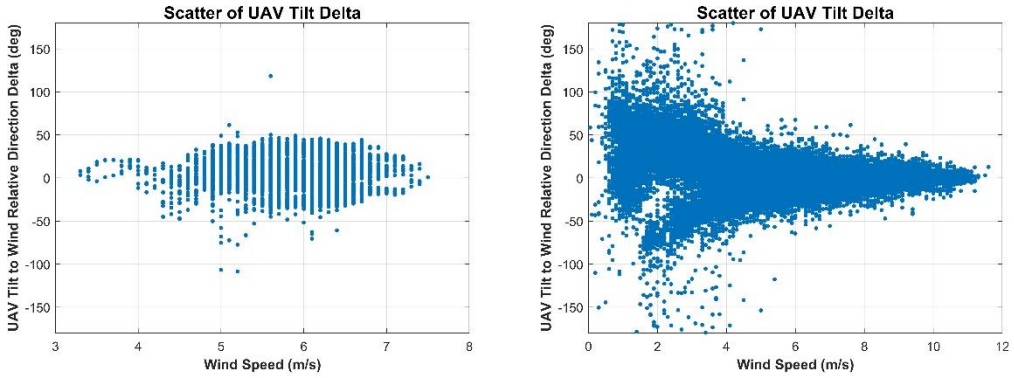

Figure 6.15: *UAV attitude bearing with respect to UAV relative wind direction as wind speed increases, for quadcopter UAV (left) and hexacopter UAV (right).*

the UAV tilts into the wind to compensate for the drag force acting on the UAV generated by the incident horizontal airflow, thus maintaining a stable hover. The UAV's tilt direction and angle are dependent on the wind direction and wind speed respectively.

6.7.1 Wind Direction and UAV Attitude

Under ideal conditions, the UAV tilt direction should be aligned with the incident wind direction. The experimental data obtained during the quadcopter and hexacopter data collection flights are presented as scatter plots, in Figure 6.15, of the angular delta between the UAV attitude bearing and wind direction as wind speed increases.

The scatter plot for the hexacopter UAV indicates that as wind speed increases, the angular delta decreases substantially, and the UAV attitude bearing aligns closer with the UAV relative wind direction. This is not as evident for the quadcopter UAV data, predominantly due to the moving average wind direction data.

6.7.2 Wind Speed and UAV Attitude

From Eq. (3.53) for the parasitic power expended by the UAV to overcome the drag force acting on the UAV generated by the incident wind speed, $\sin\alpha$ may be expressed as follows:

$$\sin\alpha = \frac{\rho S_{\text{ref}} C_D}{2T} V_\infty^2 \tag{6.2}$$

For small angles, S_{ref}, C_D, and T, may be assumed constant, whilst $\sin\alpha \approx \alpha$. For the purposes of the wind speed to UAV attitude analysis, the density of air has also been

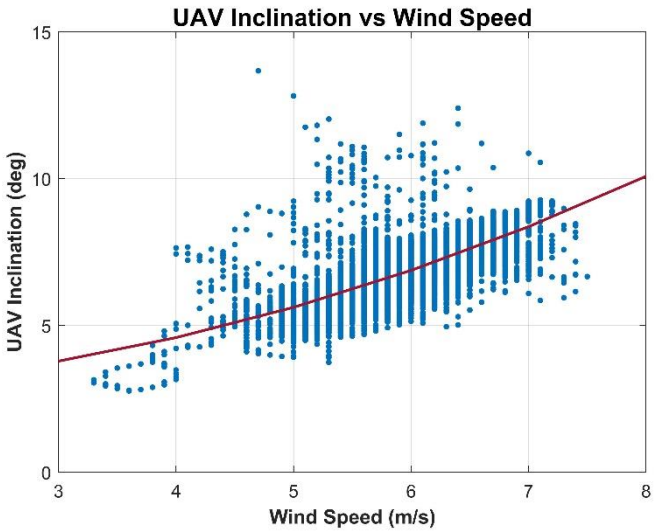

Data set	Model	No. of Data Points	R^2	RMSE *(°)*
All	$\alpha = 0.11V_\infty^2 + 2.75$	19 562	0.611	0.597

Figure 6.16: *UAV tilt angle versus wind speed for quadcopter flights.*

assumed to be constant. It therefore transpires that the UAV tilt angle is proportional to the square of the horizontal wind speed, such that $\alpha \propto V_\infty^2$ and Eq. (6.2) can be rewritten as

$$\alpha = \left(\frac{\rho S_{\text{ref}} C_D}{2T}\right) V_\infty^2 \tag{6.3}$$

Figure 6.16 shows a scatter plot of UAV inclination with respect to wind speed, for data gathered during the quadcopter flights. It should be noted that since the data used are of the moving average type and hence subsequently smoothed, the amount of scatter is minimal. This is also evidenced by the low RMSE value for this analysis. The original tilt angle logged by the quadcopter's flight controller, as expected, had a substantially larger range with the UAV inclination values spanning a wider range of between -20° and 25°, before the moving average data were calculated.

For the purposes of analysing further the UAV attitude response for the quadcopter phase of the study, the quadcopter UAV attitude data were segregated based on the incident wind direction into four equal quadrants around the quadcopter UAV. The position of each quadrant is such that its centre coincides with a UAV propulsion arm, as graphically shown in Figure 3.2. The quadcopter UAV flight data segregated by incident wind quadrant, are shown in Figure 6.17.

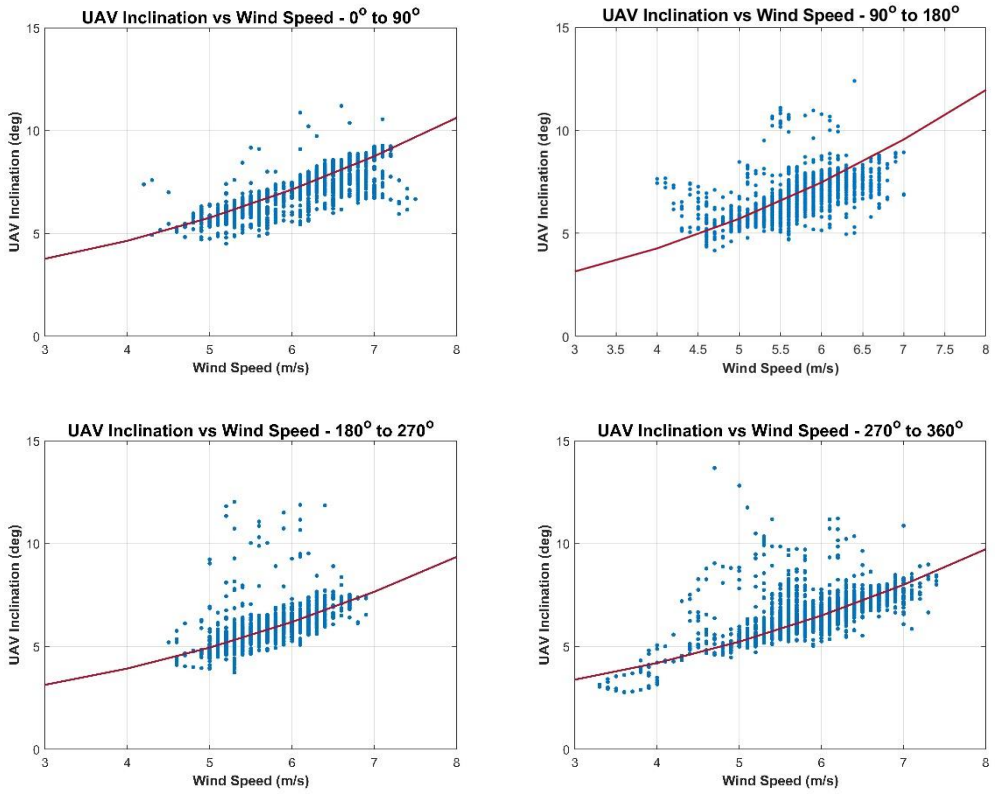

Data set	Model	No. of Data Points	R^2	RMSE *(°)*
0° – 90°	$\alpha = 0.12V_\infty^2 + 2.65$	4 396	0.820	0.396
90° – 180°	$\alpha = 0.16V_\infty^2 + 1.70$	6 560	0.732	0.379
180° – 270°	$\alpha = 0.11V_\infty^2 + 2.12$	2 057	0.814	0.374
270° – 360°	$\alpha = 0.12V_\infty^2 + 2.35$	6 549	0.898	0.239

Figure 6.17: *UAV tilt angle versus wind speed for quadcopter flights, segregated by incident wind direction quadrants around the UAV.*

The mathematical model derived earlier in this section is also evident from the plot of UAV Tilt angle with respect to wind speed for hexacopter UAV flights shown graphically in Figure 6.18. The plot shows that as the wind speed increases the multirotor tilt angle increases quadratically, in coherence with the respective mathematical expression given in Eq. (6.3). The same relationship may be observed in the scatter plots for the hexacopter UAV data subsets segregated by operational altitude, shown in Figure 6.19. It is evident that although the UAV inclination data from the hexacopter data collection flights have not been smoothed by the moving average technique applied for the quadcopter data, the hexacopter data scatter is substantially contained, with an overall RMSE value of 0.796°. This is graphically

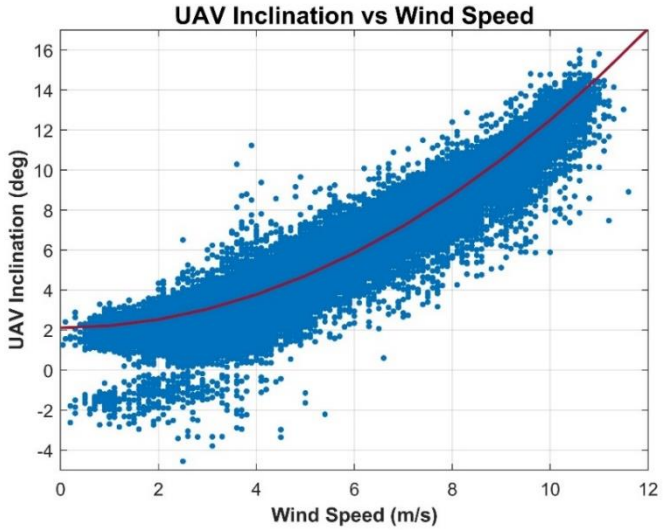

Data set	Model	No. of Data Points	R^2	RMSE *(°)*
All	$\alpha = 0.10V_\infty^2 + 2.11$	71 429	0.914	0.796

Figure 6.18: *UAV tilt angle versus wind speed for hexacopter flights.*

evident across the full range of wind speeds and operational altitudes. It is also reflected in the higher R-squared values obtained for the hexacopter data analysis, which are mostly above 0.85. It was also observed that the coefficient for the square term of the wind speed was approximately 10 % higher for the quadcopter UAV performance when compared with the performance of the hexacopter UAV. This indicates that the wind speed has a stronger effect on the UAV tilt angle of the quadcopter UAV. The above detailed observations are all indicative of the stability and robustness offered by the hexacopter UAV platform even when flown in relatively demanding wind conditions with wind speeds reaching 12 m/s, when compared to the quadcopter UAV platform.

It is interesting to note that a y-intercept of approximately 2° was present across all altitudes for the hexacopter UAV (see Figure 6.19). Since the quadcopter UAV wind speed data were in the range spanning between 3 m/s and 8 m/s, the intercept for the quadcopter UAV data was established following a curve fitting exercise. Nonetheless, this was also confirmed by the hexacopter UAV data, which covers a much wider wind speed range spanning between 0 m/s and 12 m/s.

Having established that the UAV attitude demonstrated a y-intercept of approximately 2° for both the quadcopter and hexacopter UAVs, it was interesting to study whether

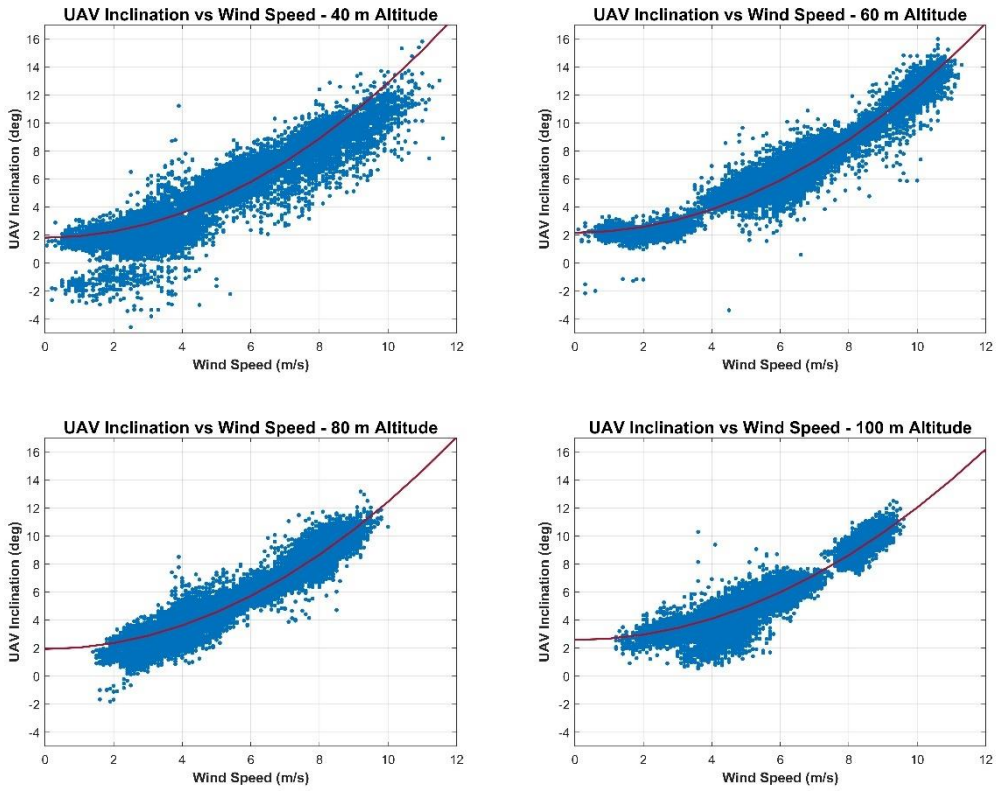

Data set	Model	No. of Data Points	R^2	RMSE *(°)*
40 m	$\alpha = 0.11V_\infty^2 + 1.81$	17 638	0.850	1.103
60 m	$\alpha = 0.10V_\infty^2 + 2.17$	17 986	0.949	0.677
80 m	$\alpha = 0.11V_\infty^2 + 1.94$	16 752	0.914	0.745
100 m	$\alpha = 0.09V_\infty^2 + 2.58$	19 053	0.922	0.612

Figure 6.19: *UAV tilt angle versus wind speed for hexacopter flights, segregated by operational altitude.*

this was manifest across the full range of UAV tilt directions, or whether this was direction specific. As was done for the quadcopter UAV data (Figure 6.17), the hexacopter UAV attitude data were segregated by the incident wind direction into six equal segments of 60° each around the hexacopter UAV, with the centre of each segment coincident with a UAV propulsion arm, as graphically shown in Figure 3.3. A series of plots for the UAV attitude with respect to wind speed segregated by each of these segments are shown in Figure 6.20.

It was observed that for both the quadcopter and the hexacopter UAVs, the intercept was positive for all wind directions, indicating that it is independent of the

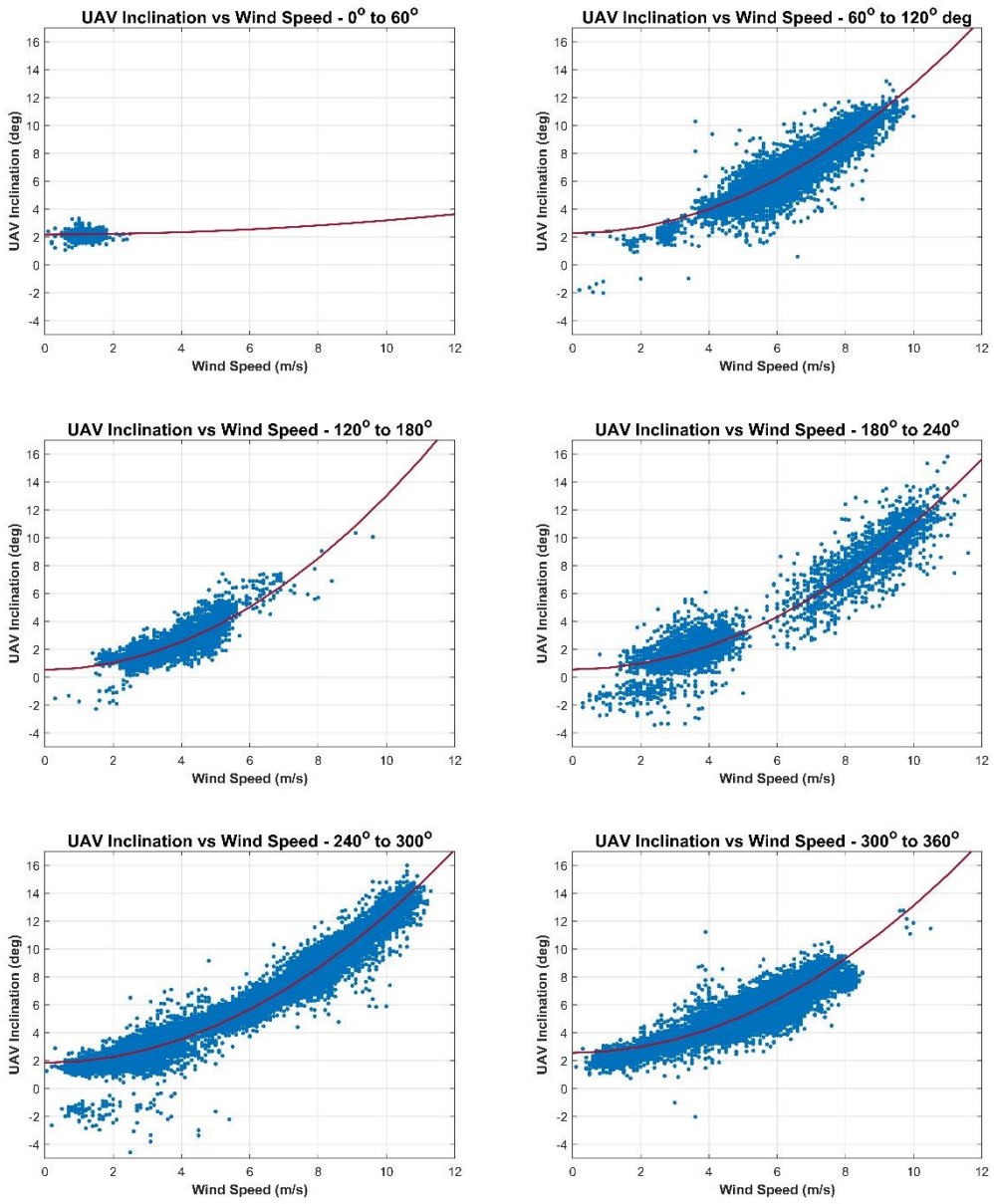

Data set	Model	No. of Data Points	R^2	RMSE (°)
0° – 60°	$\alpha = 0.01V_\infty^2 + 2.19$	653	0.216	0.238
60° – 120°	$\alpha = 0.11V_\infty^2 + 2.28$	8 957	0.859	0.726
120° – 180°	$\alpha = 0.12V_\infty^2 + 0.53$	3 729	0.722	0.632
180° – 240°	$\alpha = 0.10V_\infty^2 + 0.56$	4 253	0.932	0.954
240° – 300°	$\alpha = 0.11V_\infty^2 + 1.85$	30 954	0.972	0.515
300° – 360°	$\alpha = 0.11V_\infty^2 + 2.56$	22 830	0.864	0.567

Figure 6.20: *UAV tilt angle versus wind speed for hexacopter flights, segregated by incident wind direction 60° segments around the UAV.*

incident wind direction. Although it was observed that for the hexacopter UAV, there are some notable differences in the value of the intercept between different segments, any interpretation of such values should be done with caution. It was also observed that the number of data points for each segment, as well as the concentration of data points in relation to the wind speed range for each segment, are not consistent and vary substantially.

6.8 PWM Duty Cycle and Power Delivered

Prior to proceeding with the analysis of the power response of the multirotor UAVs as a function of wind speed and air density, it was considered beneficial to confirm using the experimental data collected whether the PWM duty cycle, weighted with the power pack voltage, was proportional to the power delivered to the motors. It should be noted that the voltage weighted PWM signal translates to the equivalent voltage being applied across the motor terminals (V_{EO}). Hence the units for this parameter are Volts.

The plot in Figure 6.21 for the quadcopter power response with respect to battery weighted voltage is indicative of a relatively linear relationship, albeit with significant data scatter. This is evidently confirmed by the considerable RMSE value and the

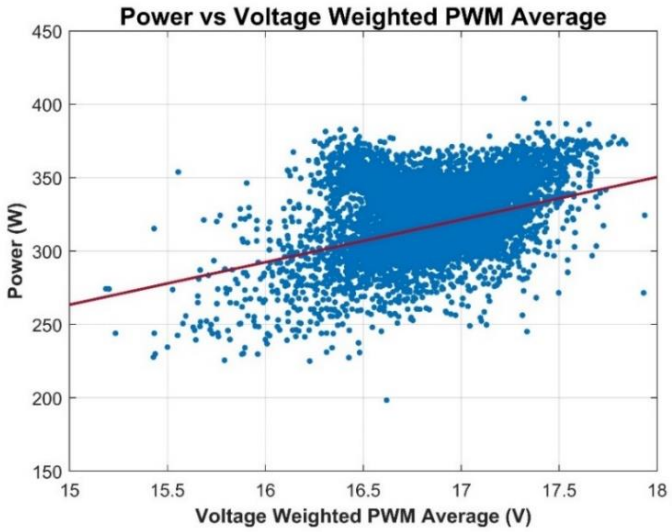

Data set	Model	No. of Data Points	R^2	RMSE *(W)*
All	$P = 28.99V_{EO} - 171.4$	19 562	0.316	14.82

Figure 6.21: *Power delivery response with respect to voltage weighted PWM signal for quadcopter UAV.*

associated low R-squared value for this relationship. In view of this, using this data set for any particular interpretation of a relationship should be done with caution.

The data for the hexacopter phase of the study confirm the proportional relationship more confidently, as demonstrated by the plot in Figure 6.22 for the full data set of Battery Voltage weighted PWM signal with respect to Power consumption. Based on this plot and the plots for hexacopter UAV data segregated by altitude (see also Figure 6.22), the relationship has a consistent gradient of approximately 76 W/V across all altitudes, with substantially high R-squared values and low RMSE values. This indicates that the power delivery response with respect to equivalent voltage is substantially linear for the operating range within which the battery power pack was utilized.

6.9 Multirotor Power Consumption

Of primary interest for this particular study is the overall power consumption of the multirotor UAV under varying wind conditions, as clearly stated in section 1.4.1. Nevertheless, it has already been established in section 3.2.5 that the air density within which the multirotor is operating also influences the power requirements of the multirotor in hovering flight. In section 3.4 it was demonstrated that the air density is a parameter dependent on atmospheric pressure, atmospheric temperature and relative humidity. These three parameters are affected by the altitude above sea level, as well as the weather conditions at the time of the UAV operations. As the data collection campaign spanned across a number of months and was conducted at different altitudes, air density was therefore considered to be another variable affecting the power response of the UAV. In view of this, the multirotor power consumption response analysis was therefore carried out with respect to both incident horizontal wind speed as well as air density.

6.9.1 Effect of Air Density on Power Demand

In an ideal hovering scenario, a multirotor UAV operates in the presence of no external disturbances. For this scenario to be more appropriately analysed, it was therefore considered that the power response of the multirotor UAVs should be analysed when the UAVs were hovering at wind speeds below a threshold of 1 m/s.

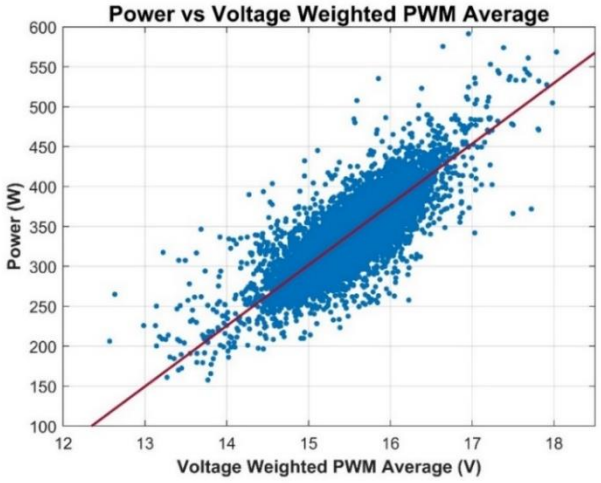

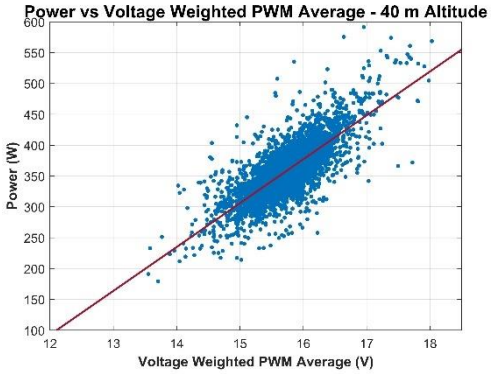

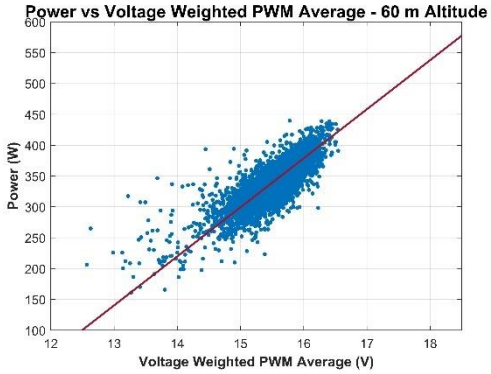

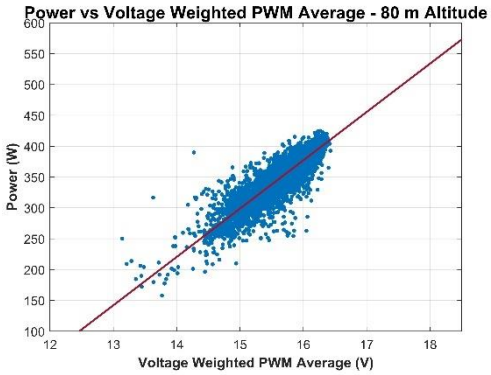

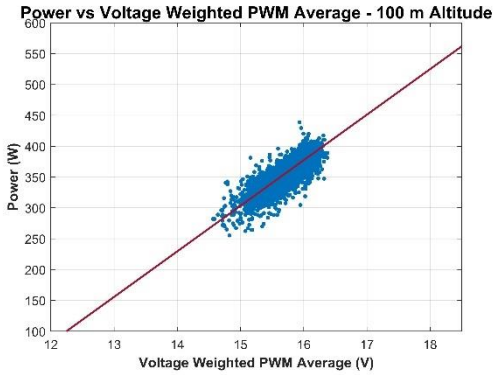

Data set	Model	No. of Data Points	R^2	RMSE *(W)*
All	$P = 76.01V_{EO} - 838.5$	71 429	0.848	9.975
40 m	$P = 71.11V_{EO} - 760.6$	17 638	0.831	10.677
60 m	$P = 79.48V_{EO} - 892.9$	17 986	0.837	11.285
80 m	$P = 78.31V_{EO} - 875.9$	16 752	0.877	10.143
100 m	$P = 73.84V_{EO} - 804.2$	19 053	0.797	7.968

Figure 6.22: *Power delivery response with respect to voltage weighted PWM signal for hexacopter UAV for the full data set as well as data subsets segregated by altitude.*

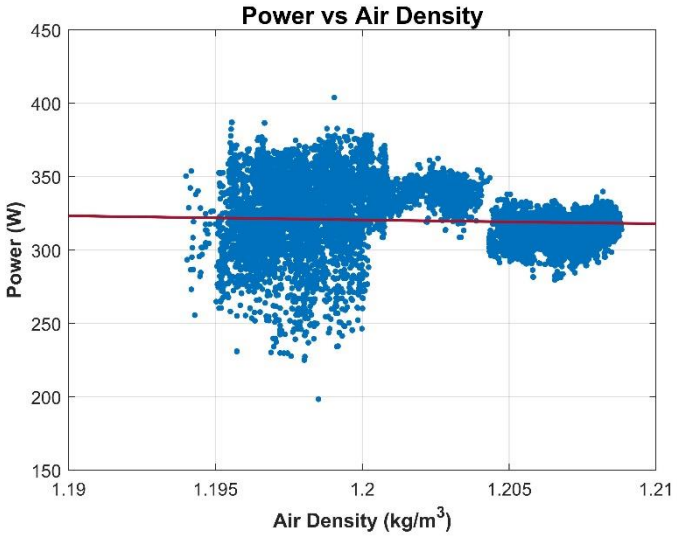

Data set	Model	No. of Data Points	R^2	RMSE *(W)*
All V_∞	$P = 384.6/\rho$	19 562	0.194	16.09

Figure 6.23: *UAV power demand versus air density for a quadcopter in hovering flight.*

Data from the quadcopter phase for wind speeds below the stated threshold were not available, hence the data analysed in Figure 6.23 are those obtained for the full range of incident wind speeds at which the quadcopter UAV was operated. Nonetheless, the data do indicate a trend coherent with the respective mathematical model.

The data set for the hexacopter UAV operations covered a much wider range of wind speeds as already highlighted in previous sections. Nonetheless it transpired that few data points were available within the wind speed range being considered for the analysis of the effect of air density on the power consumption of the hexacopter UAV. This was predominantly due to the relatively exposed UAV operations site. Nonetheless, from the data available and as correctly predicted by the respective mathematical model it was observed that as the air density drops, more power is required to maintain a stable hover, as illustrated in Figure 6.24.

It was observed that the data points at a wind speed below 1 m/s coincided with the upper portion of the air density range. Due to the concentrated nature of the data points pertinent to the data subset for wind speeds below the 1 m/s threshold, the coefficient (23.23) for the second term of the mathematical model was fixed based on the value obtained in the regression exercise of the data subset with an incident wind speed range between 1.5 m/s and 2.5 m/s. This wind speed range contained data points across a

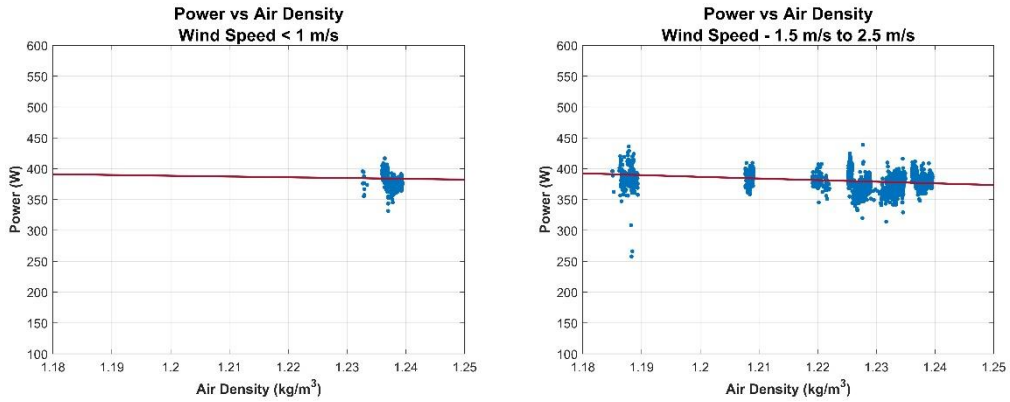

Data set	Model	No. of Data Points	R^2	RMSE *(W)*
$V_\infty < 1\,m/s$	$P = \left(395/\sqrt{\rho}\right) + 23.23\rho$	1 099	-0.021	10.38
$1.5m/s < V_\infty < 2.5m/s$	$P = (431/\rho) + 23.23\rho$	3 816	0.214	11.72

Figure 6.24: *UAV power demand versus air density for a hexacopter in hovering flight in horizontal wind speeds below 1 m/s (left) and for incident wind speeds between 1.5 m/s and 2.5 m/s (right).*

wider range of air densities, as shown in Figure 6.24. Nonetheless, such a tight wind speed range permitted that the wind speed may be assumed as constant, whilst the low wind speed value range ensured that the parasitic drag component of the power model was still negligible. When considering the 1.5 m/s to 2.5 m/s wind speed data subset, the trend of increasing power demand with a decrease in air density was further reinforced.

The observed trend explains why as rotary wing aircraft gain altitude and therefore operate in lower air densities, they require more power to maintain a stable hover [112]. Such an increase in power demand continues until the aircraft reach their respective service ceiling, at which altitude the aircraft utilize their maximum engine power capabilities to maintain hovering flight.

It should be noted that the data are significantly scattered and rather fragmented as shown in the plots in Figure 6.24. This was also the case for the data set involving the full wind speed range. This data fragmentation is further evidenced by the associated R-squared and RMSE values for the regression analysis. The availability of such a data set highlights the necessity for a more comprehensive and dedicated study for more robust and reliable relationships to be established with significant confidence.

It was therefore considered that a better approach would be to analyse the data in conjunction with the incident wind speed (section 6.9.3) which, according to the mathematical model discussed in section 3.2.5, has a significant influence on the power demand to air density relationship.

6.9.2 Effect of Wind Speed on Power Consumption

In this approach the air density is assumed to be constant and the relationship between power demand for a hovering multirotor and the incident horizontal wind speed is analysed independently of other affecting variables. The data sets generated during the data collection flights for both the quadcopter and hexacopter UAVs were duly analysed.

The effect of wind speed on the power consumption of the research quadcopter UAV is graphically shown in Figure 6.25. For this analysis, a sixteen-point moving average data set for the power consumption was used in order to match the moving mean wind speed data logs recorded by the wind speed sensor during this phase of the study. The regression analysis on the quadcopter UAV data demonstrates a trend indicating that as the wind speed increases, the power demand on the multirotor UAV's propulsion system decreases. This despite the fact that the analysis was carried out over a

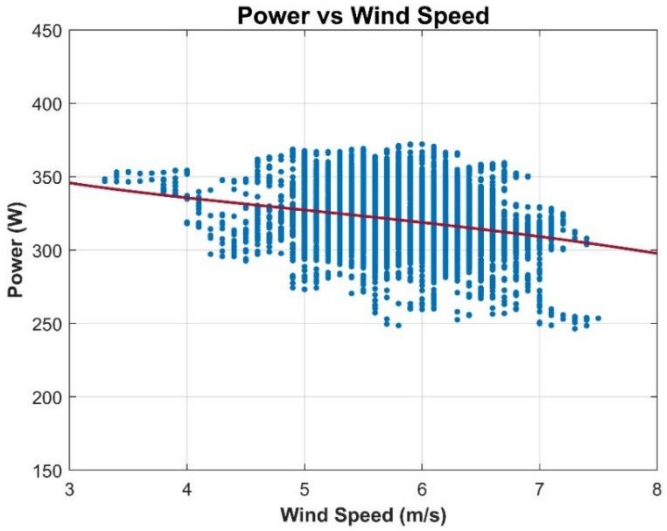

Data set	Model	No. of Data Points	R^2	RMSE *(W)*
All	$P = (95.98/V_\infty) - 0.06V_\infty^3 + 315.3$	19 562	0.164	14.60

Figure 6.25: *UAV power demand versus wind speed for a quadcopter in hovering flight.*

relatively restricted wind speed range, predominantly due to the limited number of data collection flights operated and the moving average algorithm applied to the wind speed data. It should however be highlighted that the R-squared value obtained indicates a weak correlation for the measured power demand and incident wind speed during quadcopter UAV operations. Nonetheless the observed trend of a decrease in power demand with increasing wind speed is consistent with the predictions of the respective mathematical model discussed in section 3.2.5.

Following the analysis of the quadcopter UAV power consumption data, a similar study was conducted on the hexacopter UAV data collected during the respective data collection campaign. In this case since the ultrasonic sensor wind speed readings were instantaneous readings, as opposed to the data set available for the quadcopter UAV, the regression analysis was done using instantaneous data for both power consumption and wind speed. Furthermore, it should also be highlighted that the data used for this analysis were for incident wind speeds above a threshold of 1 m/s. This approach was deemed necessary to minimize the distorting effect of the wind speed reciprocal within the induced power term on the regression function for the low wind speed data range. The resulting scatter plot for the power consumption of the hexacopter UAV in hovering flight for incident wind speeds above 1 m/s is shown in Figure 6.26.

As observed during the quadcopter UAV power response study, the resulting regression function for the hexacopter UAV power response, indicates that as the wind speed increases, the power consumption for a hovering hexacopter UAV decreases, as predicted by the mathematical model in section 3.2.5. This is accompanied by a substantially higher R-squared value of 0.490, indicating a stronger relationship. It was also observed that the RMSE value is also significantly higher when compared to the quadcopter UAV power response analysis, potentially due to the fact that the hexacopter UAV data utilized are not of the moving average type, and hence have not been smoothed. Another significant observation is the evident increase in data scatter as the wind speed increases beyond 8 m/s.

A further set of scatter plots with accompanying best fit curves is shown in Figure 6.27 for the hexacopter UAV data segregated by flight altitude. Analysing the respective plots in detail, as well as the fitted functions and their respective R-squared values, it is seen that the decrease in power demand on the hexacopter UAV's propulsion system

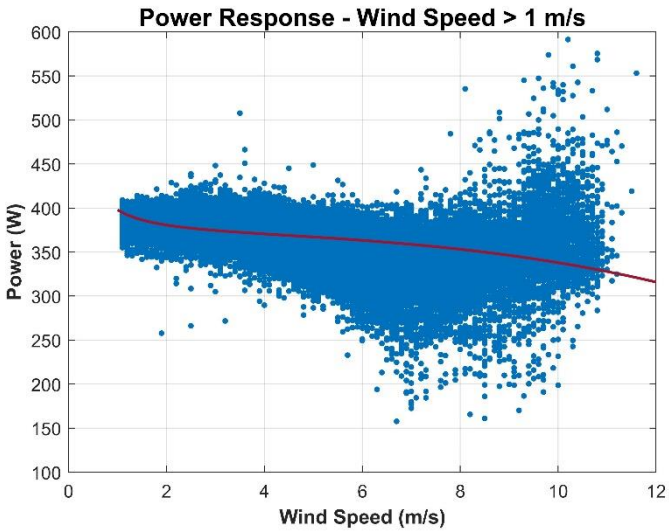

Data set	Model	No. of Data Points	R^2	RMSE *(W)*
All	$P = (33.85/V_\infty) - 0.03V_\infty^3 + 364$	71 429	0.490	18.310

Figure 6.26: *UAV power demand versus wind speed for a hexacopter in hovering flight.*

as wind speed increases is observed for all the altitude-segregated data subsets of the hexacopter UAV. As already stated, this is consistent with the predictions of the respective mathematical model. It emerges that the most significant contribution to the data scatter in the power consumption at wind speeds beyond 8 m/s observed in Figure 6.26 is the power consumption at a hovering altitude of 40 m, and to a lesser extent the power consumption at a hovering altitude of 60 m, as evidently shown by the respective plots in Figure 6.27. Such scatter is less evident in the plots for hovering altitudes at 80 m and 100 m. It was also observed that data for these altitudes were available for wind speeds of up to approximately 10 m/s.

It should be noted that during further analysis of the hexacopter UAV data discussed in section 7.4.1.1, it was established that the minimum power demand experienced by the hexacopter UAV in hovering flight coincides with an incident wind speed of 8.0 m/s. This happens to be the approximate wind speed beyond which this data scatter was observed, potentially indicating that as the incident wind speed reaches this threshold, the hexacopter UAV starts experiencing an increase in power demand depending on its relative orientation to the incident wind direction.

As already observed for the full hexacopter UAV power response data set, the R-squared values obtained for power response data subsets segregated by hovering

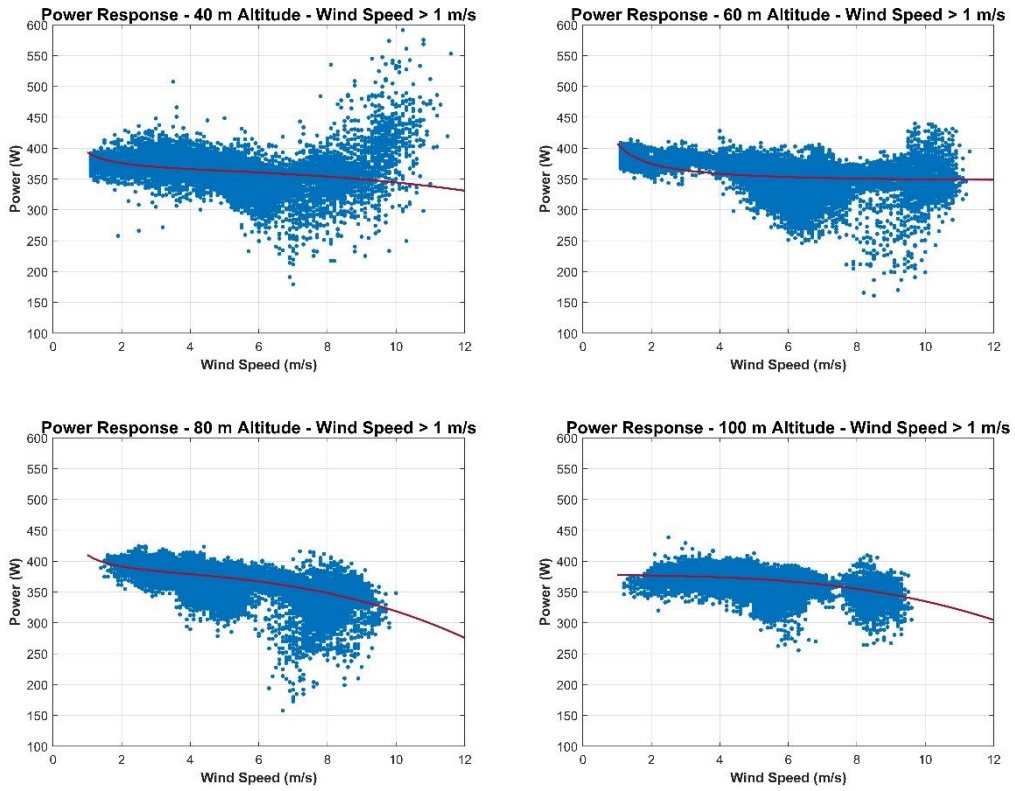

Data set	Model	No. of Data Points	R^2	RMSE *(W)*
40 m	$P = (34.49/V_\infty) - 0.02V_\infty^3 + 358.6$	17 638	0.514	18.267
60 m	$P = (64.94/V_\infty) - 0.001V_\infty^3 + 342.3$	17 986	0.383	21.695
80 m	$P = (36.46/V_\infty) - 0.06V_\infty^3 + 373.6$	16 752	0.634	17.511
100 m	$P = (1.87/V_\infty) - 0.04V_\infty^3 + 376.1$	19 053	0.389	13.812

Figure 6.27: *UAV power demand versus wind speed for a hexacopter in hovering flight, segregated by altitude.*

altitude are significantly higher than those obtained for the quadcopter UAV. An especially high R-squared value of 0.634 was obtained for the data subset at a hexacopter UAV hovering altitude corresponding to 80 m above the LiDAR reference window.

6.9.3 Effects of Wind Speed and Air Density on Power Demand

In sections 6.9.1 and 6.9.2 the impact of the atmospheric air density and incident horizontal wind speed respectively were analysed individually for potential impact on the power consumption of a hovering multirotor UAV. Nonetheless, as demonstrated by the mathematical model for the power demand of a multirotor UAV, power demand

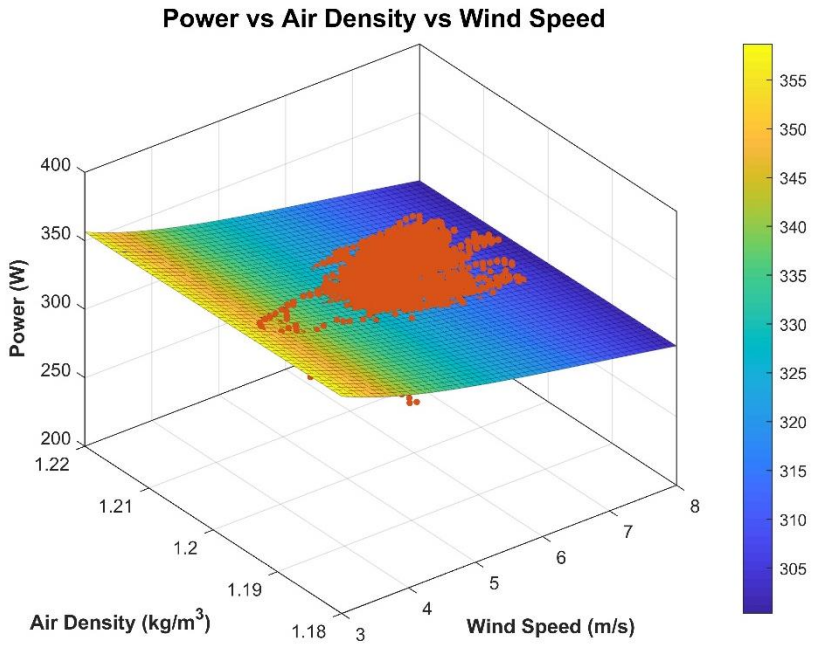

Data set	Model	No. of Data Points	R^2	RMSE *(W)*
All	$P = (526.6/\rho V_\infty) + 0.02\rho V_\infty^3 + 198.4\rho$	19 562	0.147	14.75

Figure 6.28: *UAV power demand versus air density and wind speed for a quadcopter in hovering flight.*

is dependent on both air density and horizontal wind speed. It was therefore considered appropriate to analyse the power demand of the UAV as a function of the bespoke two parameters concurrently.

The power consumption of the research quadcopter UAV as a function of air density and wind speed using a moving average data set is shown in Figure 6.28. Although the trend of decreasing power demand with an increase in wind speed is visually evident from the fitted surface, the effect of the air density on the power demand is substantially less evident when compared to the wind speed effect. Furthermore, the R-squared value for the fitted surface is relatively low. Nonetheless the R-squared value obtained was close to the values obtained for the independent analysis of the effect of the air density and wind speed on the power response of the quadcopter UAV. The significant difference in impact between the changes in air density and wind speed, highlight the dominant effect of the wind speed on the power demand of the quadcopter UAV when compared to the effect of the air density on the multirotor UAV power consumption.

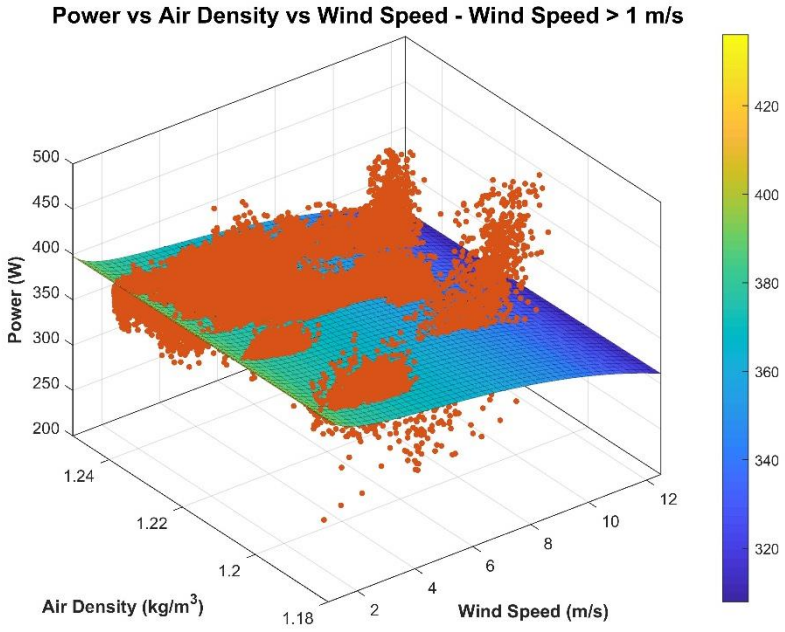

Data set	Model	No. of Data Points	R^2	RMSE *(W)*
$V_\infty > 1\ m/s$	$P = (44.9/\rho V_\infty) - 0.02\rho V_\infty^3 + 295.3\rho$	70 330	0.392	20.00

Figure 6.29: *UAV power demand versus air density and wind speed for a hexacopter in hovering flight at wind speeds above 1 m/s.*

A similar regression analysis was also carried out for the hexacopter UAV power response, for the data set with a minimum wind speed threshold of 1 m/s as was done in section 6.9.2. Figure 6.29 presents the resulting regression plot of the power consumption as a function of wind speed and air density for the hexacopter UAV in hovering flight. It was clearly evident that the power response for the hexacopter UAV was similar to that observed for the quadcopter UAV. From the plot for the full power response data set it therefore transpires that the hexacopter UAV also experiences a reduction in power consumption as the incident horizontal wind speed increases, as predicted by the mathematical model in section 3.2.5. However, the regression results for the hexacopter UAV power response have a substantially higher R-squared value, as already witnessed in section 6.9.2. Substantially less evident is the power demand response with respect to air density, as also observed for the quadcopter UAV data. Nevertheless, this was independently confirmed in section 6.9.1, whereby it was observed that as the air density increased, the hexacopter UAV power consumption decreased.

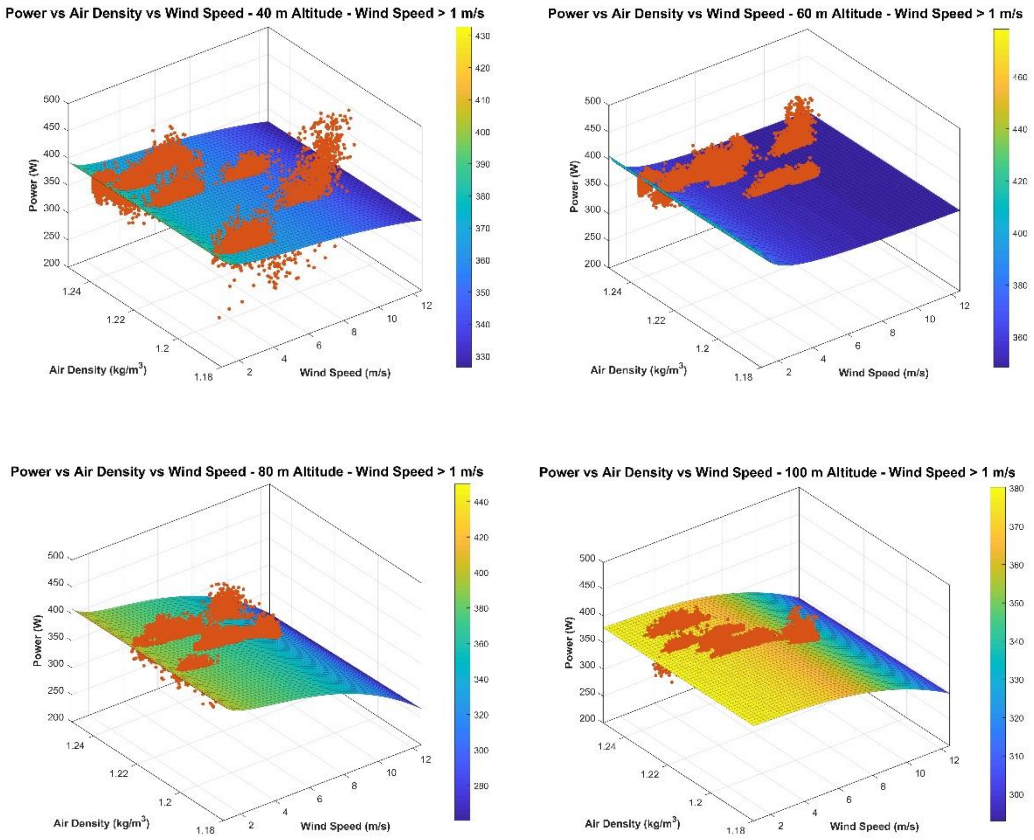

Data set	Model	No. of Data Points	R^2	RMSE *(W)*
40 m	$P = (50.62/\rho V_\infty) - 0.01\rho V_\infty^3 + 289\rho$	17 206	0.339	21.29
60 m	$P = (78.5/\rho V_\infty) - 0.002\rho V_\infty^3 + 277.8\rho$	17 319	0.368	21.97
80 m	$P = (63.16/\rho V_\infty) - 0.05\rho V_\infty^3 + 302.2\rho$	16 752	0.590	18.53
100 m	$P = (0.02/\rho V_\infty) - 0.03\rho V_\infty^3 + 306\rho$	19 053	0.337	14.38

Figure 6.30: *UAV power demand versus air density and wind speed for a hexacopter in hovering flight at wind speeds above 1 m/s, segregated by operational altitude.*

The hexacopter UAV analysis was further extended by analysing the impact of the atmospheric air density and incident horizontal wind speed on the power consumption of a hovering multirotor UAV segregated by operational altitude. From the plots for such altitude-segregated data subsets (graphically shown in Figure 6.30), it is evident that this relationship is consistent across all altitudes, but it seemingly becomes more evident as the altitude increases. Although this may potentially be due to less turbulent wind conditions as altitude increases, it has already been observed that data at these operational altitudes were available for wind speeds of up to approximately 10 m/s. It is also noteworthy that even for the altitude-segregated hexacopter UAV data subsets,

the impact of wind speed on power demand is substantially more pronounced than the effect of changes in air density on the power response of the multirotor UAV.

6.9.4 Diagonal Power Differential

As described in section 3.1, for the UAV to achieve an attitude such that the multirotor UAV tilts into the wind, the upwind rotors spin less than the downwind rotors, so that the upwind rotors generate less thrust, with the resulting thrust imbalance causing the UAV to tilt. This results in the upwind rotors consequently consuming less power than the downwind rotors. It was therefore considered reasonable to analyse the diagonal power differential between diagonally opposite rotors of the multirotor UAVs.

In the case of the quadcopter UAV the data were segregated into the four distinct quadrants as shown in Figure 3.2, on the basis of incident wind direction, as was done for the analysis in section 6.7.2 for the UAV inclination analysis. For each of the segregated data subsets, the diagonal power differential was plotted, as shown in Figure 6.31. It was observed that the power differential was minimal. In the third quadrant as the wind speed increased the power differential increased, whilst in the first and fourth quadrants a marginal decline was demonstrated. In the second quadrant the trend indicated that as the wind speed increases, the power differential decreases. Furthermore, the R-squared values for the respective quadrant analysis were very low indeed indicating that the data for the diagonal power differential and the incident wind speed were loosely correlated.

This was unexpected and could possibly be caused by multiple factors, including the very tight range of wind speeds, the limited number of data points available, differences in characteristics between electric motors, as well as measurement errors, given that the power differentials recorded are relatively small. Another potentially influencing factor is the moving average wind speed data. This results in the smoothing of any short-term wind speed and direction spikes which undoubtedly demand the multirotor to compensate for. As previously stated, although the power demand adjustment would have been recorded by the respective data logging system, this unfortunately could not be matched with the corresponding wind event causing it.

Similarly, for the hexacopter setup, the data were segregated into the six distinct wind direction segments graphically shown in Figure 3.3. For each of the wind direction segregated data subsets, the power differential was plotted, as shown in Figure 6.32.

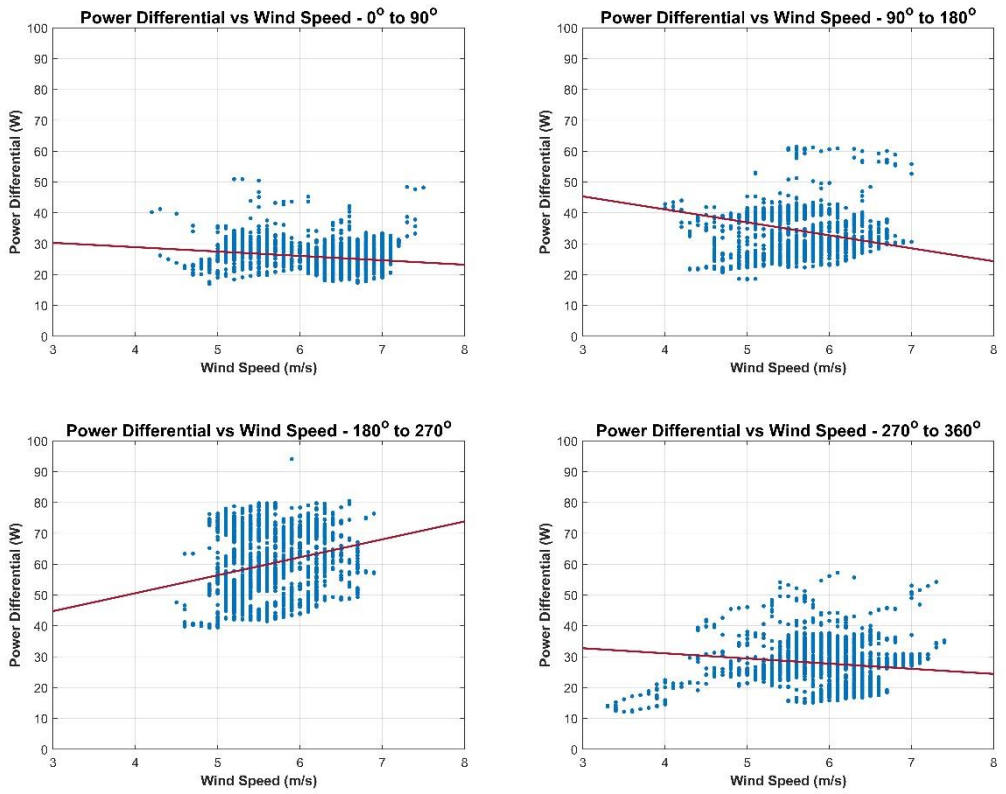

Data set	Model	No. of Data Points	R^2	RMSE *(W)*
0° – 90°	$P_{Diff} = -1.42V_{\infty} + 34.56$	4 396	0.047	3.576
90° – 180°	$P_{Diff} = -4.20V_{\infty} + 57.93$	6 560	0.058	5.918
180° – 270°	$P_{Diff} = 5.82V_{\infty} + 27.33$	2 057	0.056	10.31
270° – 360°	$P_{Diff} = -1.67V_{\infty} + 37.76$	6 549	0.016	6.417

Figure 6.31: *Diagonal Power Differential versus wind speed for quadcopter UAV.*

The power differentials for the hexacopter UAV indicate that an increase in wind speed is coupled with a commensurate increase in diagonal power differential, which eventually results in an increase in the UAV tilt angle. This relationship was found to be consistent for all the hexacopter UAV segments that were independently analysed. It was also observed that the R-squared values obtained were reasonable and in segments 1, 4 and 5 the R-squared value was greater than 0.6.

It should be noted that intercepts and gradients are very much dependent on the individual motor characteristics and their respective differences. Furthermore ESC-motor pair inefficiencies may vary between assemblies giving rise to different power demands for similar thrust differentials.

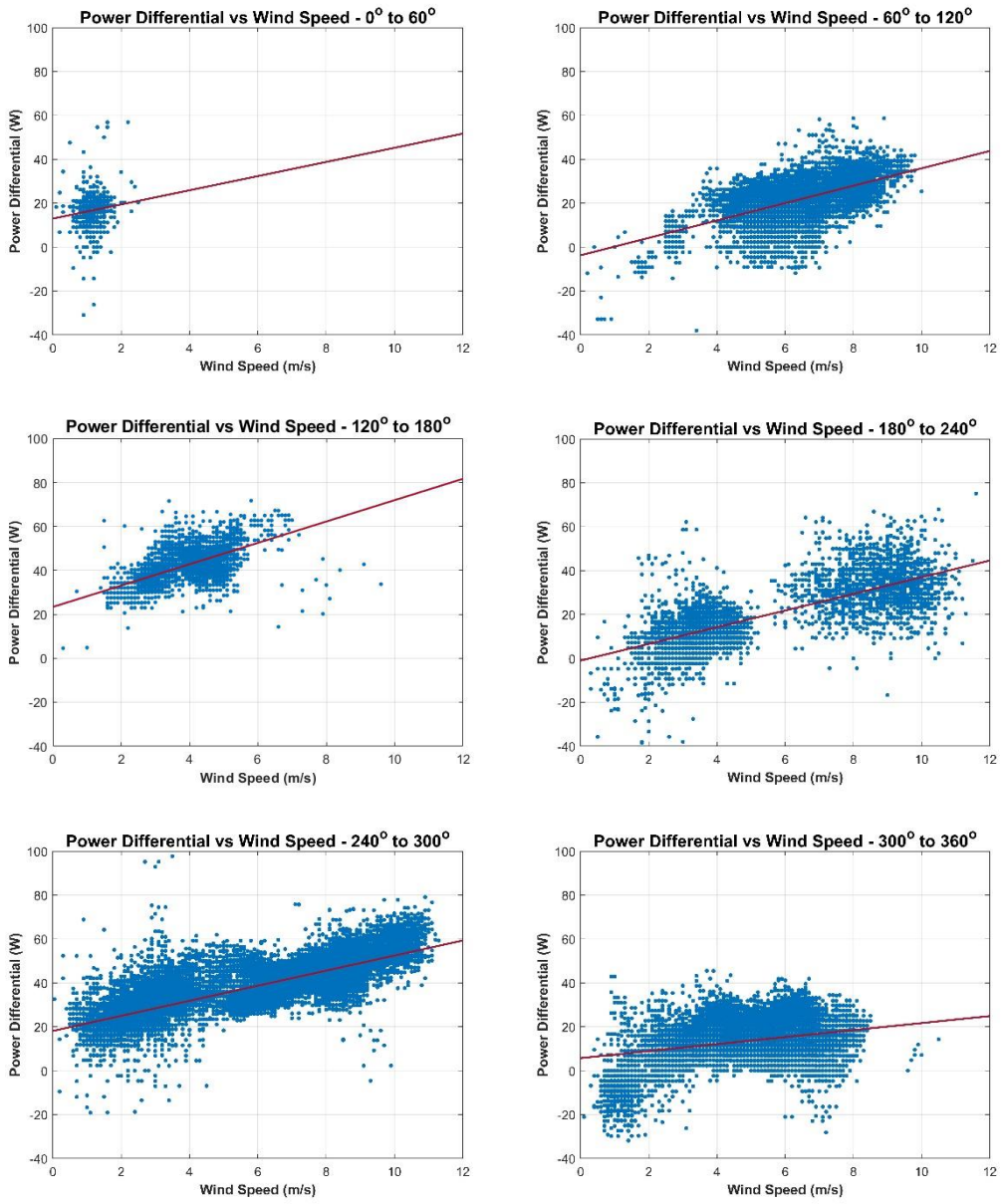

Data set	Model	No. of Data Points	R^2	RMSE *(W)*
0° – 60°	$P_{Diff} = 3.23V_{\infty} + 12.98$	653	0.615	4.707
60° – 120°	$P_{Diff} = 3.96V_{\infty} - 3.73$	8 957	0.372	7.624
120° – 180°	$P_{Diff} = 4.86V_{\infty} + 23.34$	3 729	0.421	5.658
180° – 240°	$P_{Diff} = 3.80V_{\infty} - 1.00$	4 253	0.673	8.412
240° – 300°	$P_{Diff} = 3.43V_{\infty} + 18.11$	30 954	0.702	5.720
300° – 360°	$P_{Diff} = 1.60V_{\infty} + 5.74$	22 830	0.204	7.578

Figure 6.32: *Diagonal Power Differential versus wind speed for hexacopter UAV.*

The experimental data indicate that this research study hexacopter's total power requirement for maintaining a hover is in the region of 360 W, or approximately 60 W per rotor. The power differentials obtained from the experimental data result in a power delta gradient of approximately 3.5 W s/m. In other words, the difference in power between diagonally opposite motors increases by approximately 3.5 W for every 1 m/s increase in the incident wind speed.

7 Discussion

Following an in-depth analysis of the data gathered during the data collection campaign, and an initial interpretation of the results obtained, this chapter discusses the findings presented in Chapter 6. It first discusses the wind data correlation between the onboard ultrasonic wind sensor and the ground-based LiDAR measurement unit. This is then followed by a discussion on the multirotor UAVs' performance, as they were operated in various wind conditions for data collection purposes.

Throughout the analysis carried out and described in Chapter 6, it was observed that in general, the data collected during the hexacopter phase seem to be more coherent than those collected during the quadcopter phase having significantly less data scatter. This is predominantly attributed to a more stable aircraft for the operating conditions it was subjected to. The stability of the hexacopter UAV when compared to the quadcopter UAV is also evidenced by the tighter hexacopter UAV tilt range when compared to the quadcopter UAV tilt range, despite the hexacopter having been operated in much stronger winds of up to 12 m/s.

Furthermore, it was evident during the analysis of the collected data, that the reduced number of data points for the first phase of the study using the quadcopter UAV resulted in limitations as to the depth of analysis that could be achieved. This reinforced the necessity of conducting extensive data collection campaigns, especially in research areas dealing with open field studies.

7.1 LiDAR to Ultrasonic Wind Sensing

It should be noted that the UAVs were operated at a distance of approximately 75 metres South East of the LiDAR site, as graphically shown in Figure 5.2. As previously explained in section 5.1.1, this hovering location was selected due to its being downwind of the LiDAR unit (WRT the prevalent NW winds). Nevertheless, this strategy comes with a downside; namely that the localized wind fields at the UAV operations site might have differed from those immediately within the LiDAR's scanning cone, this giving rise to slight discrepancies in the readings. This was also highlighted by the LiDAR unit's manufacturer [113]. Such differing localized wind fields could also potentially be due to the difference in topography, surface roughness

and obstacles between the two sites. This effect was also attributed to the discrepancies in the readings observed by Shimura et al. [51] in their wind correlation study.

The ZephIR LiDAR's manual for the siting of the bespoke instrument clearly warns that as the separation between the points at which measurements are taken increases, the correlation between the measurements of such instruments is subject to deterioration, 'even in flat terrain' [113]. Although the manual refers to instances when LiDAR wind measurements are to be compared against a meteorological mast, this also applies to instances when the LiDAR unit is used as a reference for other wind measuring instruments, such as the UAV-mounted ultrasonic wind sensor used in this study.

7.1.1 Wind Speed

The wind speed correlation results presented in section 6.3.1, for the wind speed readings of the LiDAR unit and the hexacopter UAV-mounted ultrasonic wind sensor indicate that the latter sensor's readings generally differ from the LiDAR wind speed measurements by a positive offset of 1 m/s. The regression line gradient for the full data set across all flight altitudes was found to be 1.01, which is very close to unity. It was also observed that a consistent regression line gradient close to unity and an offset of 1 m/s were present for the wind speed data segregated by operational altitude, as demonstrated in Figure 6.4. Such a regression line gradient of unity indicates that the offset of 1 m/s does not change with increasing wind speed and therefore remains constant irrespective of the incident wind speed.

The wind speed offset observed may be caused by the different topography at the two wind measurement points. Nonetheless, it may also have been potentially caused by the incident horizontal wind disturbing the inflow field of the UAV rotors at the wind sensor level above the UAV centre hub, causing it to skew in the wind direction. This may have resulted in the mounted wind sensor reading a higher horizontal wind speed than the actual atmospheric wind speed. Shimura et al. [51] and Palomaki et al. [52] both identified a wind speed bias of 0.5 m/s in their respective studies with hexacopter UAVs, which they attributed to rotor-induced wind flow. Palomaki et al. [52] identified a further wind speed bias during open field testing to which the authors could not confidently pinpoint an exact cause. The obtained results therefore further justify a proper investigation into the cause of the 1 m/s offset to establish whether this was a

topographically induced offset, a UAV rotor airflow-induced offset, or potentially a combination of both of these causes.

Nonetheless, an attempt to establish the cause of this offset was made during this study by running sheltered tests, under both airborne and tied down conditions. The results for such tests have been presented in sections 6.3.3 and 6.3.4, and discussed further in section 7.1.3. Due to the limited control on the environment in which these tests were carried out, the cause of the wind speed offset could not be established with substantial certainty. Although the results obtained do provide an indication that a portion of this offset may be caused by the rotor-induced airflow.

7.1.2 Wind Direction

The wind speed data analysis was followed by a similar analysis of the wind direction data detailed in section 6.3.2. To analyse the relationship, it was deemed suitable to use a Cartesian plot thereby plotting the reference LiDAR wind measurements on the x-axis and the UAV mounted wind sensor measurements on the y-axis. On a Cartesian plot a perfect correlation would yield a linear regression line having a gradient of unity and a y-intercept of zero. This made it more adapt to properly compare the readings from the two different instruments, and the correlation between the two data sets. For the wind direction correlation study, it was also deemed appropriate to fix the regression coefficient at unity. Although the data values fall in the range 0° to 360°, this is a circular data range and it therefore transpires that the offset at the 0° and 360° positions should be equal. This was achieved by fixing the gradient of the fitted regression line at unity.

It should also be noted that the LiDAR unit was installed on the rooftop of an RO plant. Consequently, the unit was placed on top of a concrete structure which also contained a reinforcing steel mesh. Furthermore, the hall beneath the unit housed high voltage power transformer units required to power the RO plant, potentially generating substantial magnetic fields. This could potentially lead to anomalies in the compass readings of the LiDAR unit, and to a lesser extent the compass readings of the UAV-mounted instruments. Notwithstanding the magnetic environment, the data indicate a relatively strong correlation between the two sensing instruments.

The correlation for wind direction readings between the two instruments, based on the Cartesian plot shown in Figure 6.5, resulted in a negative wind direction offset of 6.16°

for the ultrasonic sensor wind direction reading with respect to the LiDAR wind direction measurement. The offsets for the wind data segregated by flight altitude, shown in Figure 6.6, fall within a relatively tight angular range of less than 3°, more specifically between -4.84° and -7.69°. This indicates a reliable wind direction reading which is further reinforced by the high R-squared values which exceed 0.93 for each of the wind direction correlation studies. It should be highlighted that such a consistent discrepancy could be caused by various factors. Two main factors that may have a significant contribution to this offset could be a slightly altered wind profile from the LiDAR reading cone to the UAV hovering site, as well as any minor misalignment in the mounting references of the two instruments. A third cause that may also have a minor influence on the resulting offset may be the difference in localized electromagnetic fields as a result of the electrical plant at the LiDAR installation site. The resulting offset may potentially be a combination of the above factors with each cause only providing a minor contribution to the overall offset.

It was also observed that when incident wind speeds were in the lower range, a wider discrepancy was noticed in the wind direction readings between LiDAR and ultrasonic wind sensor readings. This was confirmed from the plot in Figure 6.7. This phenomenon was to some extent to be expected, as lower wind speed conditions tend to give rise to relatively more independent localized wind eddy currents. These easily differ between the different measurement locations of the UAV hovering position and the LiDAR reading cone.

7.1.3 Sheltered Test Flights and Tied Down Testing

Having established that the wind speed data between the two sensors showed a 1 m/s offset, it was interesting to establish whether there may have been any particular UAV-induced signature wind profile contributing towards this wind measurement offset. Should this have been the case, such signature wind profiles could be established for the various operating conditions of the UAV and the various rotor speed profiles of the UAV. Once these have been established, such profiles could be superimposed onto the wind readings from the open field tests to further enhance the accuracy of the open field wind measurements. The purpose of conducting sheltered UAV flights as well as tied down tests was to identify whether such signature wind profiles were indeed present.

The recorded average wind speed measurements for the sheltered set of flights, were very consistent with an overall average of 1.03 m/s and falling within a very tight range of between 0.98 m/s and 1.11 m/s, as detailed in Table 6.1. Although this could very well be partially or completely caused by an incident wind at the time of the flights, it is also equivalent to the correlation offset between the UAV onboard sensor and the LiDAR wind speed measurements. Furthermore, the wind rose plots shown in Figure ***6.8***, for the wind data during the airborne sheltered flights, indicate a relatively wide wind direction spread, both within each flight as well as across flights, with a relatively consistent wind speed spread in all wind directions. It should also be noted that the three airborne sheltered flights were conducted within a tight 50-minute window, giving little time for the open field atmospheric wind conditions to change between flights.

When the hexacopter UAV was operated under tied down conditions, the UAV flight controller continued to demand close to maximum thrust (85 % PWM duty cycle). Under these conditions, as the battery voltage drops so too does the RPM of the UAV's rotors. This makes testing under these conditions more challenging due to a diminishing RPM, as the test progresses.

Nonetheless, it was evident that a significantly lower wind speed was measured during the sheltered flights than when tests were run under outdoor tied down conditions. This suggests that although the UAV was setup with the rotor hubs at 1.2 m above the ground, the proximity of the ground influenced the wind speeds measured. Unfortunately elevating the UAV further during outdoor testing would have exposed the wind sensor to stronger incident atmospheric wind currents, defying the scope of the tied down tests; namely carried out to independently measure the effect of the UAV rotors on the wind sensor measurements.

A substantially noticeable difference between the tied down tests and the sheltered flights data sets is in the average recorded wind speeds. Whilst the sheltered flights recorded a wind speed average of 1.03 m/s, the tied down test with all rotors running at full throttle recorded an average recorded wind speed of 2.35 m/s. The recorded background wind speed average was approximately 0.5 m/s, as evidenced in Table 6.2 by the average wind speeds for the two powered down tests conducted. Although this substantial difference could have been caused by the proximity of the UAV to the

ground during tied down testing, it should also be highlighted that the tied down tests were run with rotors spinning at an average of 5740 rpm, whilst the sheltered flights were run with rotors spinning at an average 4560 rpm. In the latter case this was just enough to maintain the hexacopter UAV in a stable hover.

Another particular observation is that although for both the sheltered flights and the tied down test with all rotors powered-up there is a significant spread in data, a higher occurrence of incident wind is found in the 30° to 60° relative wind direction. Although this could possibly be an indication of a particular UAV signature wind profile, this may warrant a more extensive study focusing specifically on establishing any such signature wind profiles, as discussed hereunder in section 7.1.4.

7.1.4 Proposed Testing Scenario

Collecting experimental data in open field conditions has many advantages: predominantly that such an operating scenario is fully representative of the real-life environment in which any deployed multirotor UAV will operate. Nevertheless, using such a scenario for research purposes comes with its inherent challenges. Most notably it is a relatively uncontrolled environment and hence very stochastic in nature. Isolating individual factors which potentially have an adverse effect on the UAV-based wind sensor measurements is difficult to achieve in such uncontrolled environments. To better understand the effects of individual factors on the onboard wind sensor measurements it is best to operate in a relatively more controlled environment.

In view of this, for data collection under no wind conditions it is suggested that such measurements are to be carried out at an indoor location having a relatively high ceiling. Such an enclosure should typically have a 25-metre-high ceiling or above, whilst the enclosure side walls should be adequately distant from the operating UAV. Furthermore, the UAV is to be tied down to an elevated structure approximately five metres to eight metres above the ground to eliminate any ‘ground effect’ phenomena. It is also proposed that in order to attain a deeper understanding of the influence of the rotors on the wind sensor, the UAV is to be connected to a constant voltage supply so that the motors’ RPM can be properly controlled and stabilized. Such an experimental setup also offers the possibility of carrying out tests for RPM profiles with unequal rotor speeds. For the purposes of establishing further potential UAV signature wind profiles when operating under different wind conditions, further testing may be carried

out in the controlled environment of a suitably sized wind tunnel for a range of simulated wind speeds.

7.2 UAV Power Pack Management

The importance of the accurate measurement of wind data using a multirotor UAV platform was highlighted in section 2.1.1. Nonetheless, the effectiveness of such wind monitoring techniques may only be appreciated if the platforms used offer a reasonable flight endurance as stated in section 2.2. The flight endurance of a multirotor UAV is not dependent only on the capacity of the battery pack that it is equipped with, but is also very much a function of the battery management strategy adopted. When using typical recommended battery voltages that trigger a landing upon a cell reaching 3.8 V the endurance is relatively limited. This type of battery management is usually adopted to maximize battery life and the number of recharge cycles. At these values, batteries are only utilized down to a residual charge of approximately 50 %, depending on the intensity of the current drawn. If, on the other hand, the drone is operated for maximum endurance, such as in cases of emergency, then the residual charge in the battery before forcing a landing can easily be allowed to drop to 20 % of the battery's capacity and possibly beyond, extending the UAV's endurance substantially.

It should also be noted that LiPo batteries of the type used for multirotor aircraft experience a voltage bounce-back as soon as there is a drop in power demand. This is clearly evident from the experimental data shown in Figure 6.11 and Figure 6.12. In these plots a minor voltage rise may be observed during the descent phase of the UAV, before the UAV lands and shuts down completely. A more substantial bounce-back occurs over the following few hours, whereby the battery voltage climbs steadily by approximately 0.8 V. Incidentally as the voltage drops, more current is drawn to compensate for the decrease in voltage, causing the battery voltage to drop further triggering the UAV to execute a landing.

Since one of this study's main focus areas was the impact of the wind on the flight performance of the UAV, it was opted to preserve the battery as much as possible. A battery management regime to protect battery lifetime was therefore adopted throughout the study, whereby a landing was triggered once the battery reached a voltage of 22.5 V, which is equivalent to a cell voltage of 3.75 V.

7.3 Multirotor UAV Attitude

In section 6.7 of this dissertation an analysis of the UAV attitude response to the incident wind speed and wind direction was carried out.

7.3.1 Wind Direction and UAV Attitude

It is observed in section 6.7.1 that for the hexacopter phase of the study for wind speeds in excess of 5 m/s, the data points converge to within ± 50°, indicating a substantial alignment between the UAV attitude direction and the incident wind direction. It was also observed that some residual scatter is still visible at these wind speeds and this could potentially be caused by the non-uniform lateral profile of the UAV as the relative wind direction changes. This was also identified in a modelling study by Schiano et al. [54] as well as in another study by Neumann et al. [61]. Although a multirotor UAV is inherently symmetrical its lateral aerodynamic profile is not uniform. Due to this, the incident wind has a different effect on the UAV attitude response depending on whether it is incident along a UAV propulsion arm or incident in between propulsion arms. Another non-uniformity is the Arduino data logger orientation with respect to the incident wind direction which may have also contributed to the observed scatter.

At lower wind speeds a more substantial scatter is observed to the extent that some data points indicate a UAV attitude opposite to the incident wind direction (points falling outside the ± 90° direction delta range). This is indicative of a relatively more turbulent wind field as the wind speed drops. Such negative UAV attitude readings could also be caused by UAV delayed response to wind speed fluctuations, especially abrupt changes in wind speed.

Although a similar phenomenon is observed in the quadcopter phase wind data, a proper analysis is limited by the fact that in this case, the data points are averaged and therefore any instantaneous wind and attitude measurements have been smoothed out.

7.3.2 Wind Speed and UAV Attitude

It should be noted that the mathematical model presented in Eq. (6.2) from which the approximation for the UAV inclination angle in Eq. (6.3) is derived, assumes absolute rigidity of the UAV frame. Nonetheless this is not the case and the UAV flexes under

the different loads that it is subjected to during flight. Even though the UAV arms are identical, there would still be slight differences in rigidity between each arm.

It was expected that the UAV attitude y-intercept would be 0°, indicating that at a wind speed of 0 m/s, the UAVs would hover with rotors level. It transpired that a y-intercept of 2° across all wind directions for both quadcopter and hexacopter UAVs was identified following the respective data analyses. Although marginal, its consistency for both UAVs and for all incident wind directions indicated that there may be an underlying cause for its presence. Amongst other factors, it was considered that such an intercept may have been caused by sensor error, misalignment in the assembly of the UAV arms or the motor mountings onto the propulsion arms, as well as rotor and UAV imbalance. Furthermore, the upward flexing of the UAV propulsion arms under the UAV's weight as well as mathematical model inaccuracies may also contribute to the observed intercept. Nevertheless, since the intercept is consistent and positive in all relative wind directions with only slight variations between segments, it was hypothesized that this intercept is potentially not caused by sensor error but could be a combination of a number of factors encountered in the open field.

When a UAV operates in 'no wind' conditions, the angle of attack (AOA) at which the rotors operate is the same for all rotors, irrespective of the amount of flexing of the UAV propulsion arms. It transpires that when operating in an incident wind, since the UAV departs from a level attitude each rotor operates at its own AOA, due to the upward flexing of the propulsion arms. This gives rise to the rotors generating different thrusts for the same RPM. Moreover, the aerodynamic profile and the associated drag force acting on the UAV also change due to the UAV's new attitude. It should also be noted that in such conditions, the operation of the downwind rotors may potentially be adversely affected by the turbulent wakes of the upwind rotors, as established by Prudden at al. [94], thereby necessitating the UAV to adjust its attitude angle to rebalance the forces acting on the aircraft. It therefore transpires that as the UAV transitions from operating in ideal 'no wind' conditions to operating in the presence of an incident wind, the aerodynamic conditions within which the UAV operates change substantially, potentially giving rise to the observed 2° intercept.

In the expression for the approximation of the UAV inclination given in Eq. (6.3) it is assumed that the coefficient of drag (C_D) and the reference surface area (S_{ref}), remain

constant for all UAV attitudes. Nonetheless, it is understood that these two parameters are not independent of the UAV attitude and therefore have an effect on the approximation accuracy. These inherent inaccuracies in the assumptions made in deriving the mathematical approximation used to model the UAV response to the incident horizontal wind speed may also contribute to the intercept observed.

As already highlighted, it was also observed that at very low wind speeds, negative angles of tilt were occasionally registered. This indicates that the UAV was tilted away from the incident wind direction. It is interesting to note that most of the negative inclination readings are encountered at an operational altitude of 40 m above the LiDAR reference window which is the operations altitude closest to the ground and at wind speeds below 3 m/s. This might be indicative that a more turbulent wind field is present at these hover altitudes and that wind conditions become less turbulent as altitude increases. This is evidenced by the decrease in negative inclinations as the UAV's operational altitude increases.

7.4 Multirotor Power Consumption

The study of UAV power consumption with respect to air density and wind speed was analysed independently with respect to the air density and wind speed, and then in conjunction with both parameters. For the study with respect to air density, it was intended that only data for wind speeds below 1 m/s would be utilized. Such an approach permitted the use of a mathematical model which was independent of wind speed. Hence the only remaining variable in the model would have been the density of air. Unfortunately, such data were very limited for the hexacopter phase, as discussed in section 6.9.1, and completely absent for the quadcopter phase of the study.

The analysis of power demand with respect to incident wind speed was carried out utilizing data for wind speeds above 1 m/s. This approach was adopted as the mathematical approximation for power demand in relation to wind speed is most suited for elevated wind speeds, and it performs relatively poorly at very low wind speeds, as explained in section 6.9.2.

The above two independent analysis were followed by a combined analysis of power demand with respect to atmospheric air density and wind speed for data with incident wind speeds above 1 m/s.

7.4.1 UAV Power Response

The research UAVs utilized were not equipped with onboard load cells to monitor the thrust generated by each rotor in real time. In the absence of individual rotor thrust data and since the UAV tilt angles that were experienced during open field operations were relatively small, it will be assumed that the thrust was the same for each rotor and the mathematical model in Eq. (3.57) may therefore be rewritten to represent a multirotor in open field hovering flight as

$$P = N_r\left(\frac{\kappa T^2}{2\rho A V_\infty}\right) + N_r\left(\rho A(\Omega r)^3\left(\frac{\sigma C_{d_0}}{8}\right)(1+K\mu^2)\right) + \frac{1}{2}\rho V_\infty^3 S_{\text{ref}} C_D \quad (7.1)$$

where N_r is the number of rotors powering the UAV.

From Eq. (7.1), the coefficient for the induced power term which is the first term in Eq. (7.1), is

$$C_{P_i} = \frac{N_r \kappa T^2}{2A} \quad (7.2)$$

The coefficient for the profile power term, the second term in Eq. (7.1), is

$$C_{P_0} = N_r A(\Omega r)^3\left(\frac{\sigma C_{d_0}}{8}\right)(1+K\mu^2) \quad (7.3)$$

and the coefficient for the parasitic power term, the third term in Eq. (7.1), is

$$C_{P_p} = \frac{1}{2} S_{\text{ref}} C_D \quad (7.4)$$

During the development of the mathematical model described in Chapter 3, it was known in advance that the induced power coefficient C_{P_i} varies with increasing wind speed. The increase was to be expected as the wind speed increased from very low values, through wind speeds equivalent to the rotor induced velocity, to substantially higher wind speeds. From the experimental data gathered during the course of this study it was established that C_{P_i} increased progressively as the wind speed increased.

The *Intermediate Speed approximation* proposed in section 3.2.4.3 is an attempt at providing a more accurate approximation of the coefficient for wind speeds close to the rotor-induced speed. Comparing Eq. (3.47) for the induced power under high speed flight conditions to Eq. (3.48) for intermediate speed flight conditions makes it evident

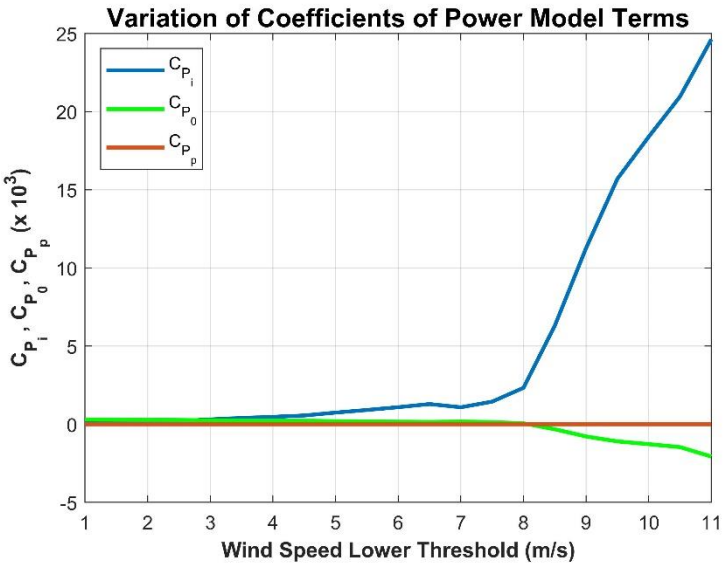

Figure 7.1: *Variation of the three coefficients of the power terms constituting the hexacopter UAV mathematical model, as the lower wind speed threshold is increased.*

that the coefficient of the induced power model for high speed flight is higher than that for intermediate speed flight. This is in agreement with the induced power coefficients obtained experimentally in this study and graphically represented in the plot of C_{P_i} against an increasing wind speed lower threshold shown in Figure 7.1.

The variation of the coefficient for the profile drag term, C_{P_0}, as the lower wind speed threshold increases unexpectedly drifts into negative territory at a wind speed lower threshold of approximately 8 m/s. This term should, in practice be positive and remain relatively constant as profile drag is dependent on rotor angular velocity, which remains relatively constant over the range of wind speeds at which the UAV was operated.

According to the regression analysis of the experimental data, the coefficient for parasitic drag, C_{P_p}, remains relatively constant across all wind speed thresholds. As expected, it is also various orders of magnitude smaller than C_{P_i}. Theoretically, this power term increases as wind speed increases due to the larger drag force acting on the UAV in flight. It also transpires that its coefficient should potentially vary with increasing wind speed as both S_{ref} and C_D vary with a change in UAV attitude. From Figure 7.1 it was observed that both C_{P_i} and C_{P_0} undergo a substantial change in gradient at approximately an 8 m/s lower wind speed threshold, which coincides with

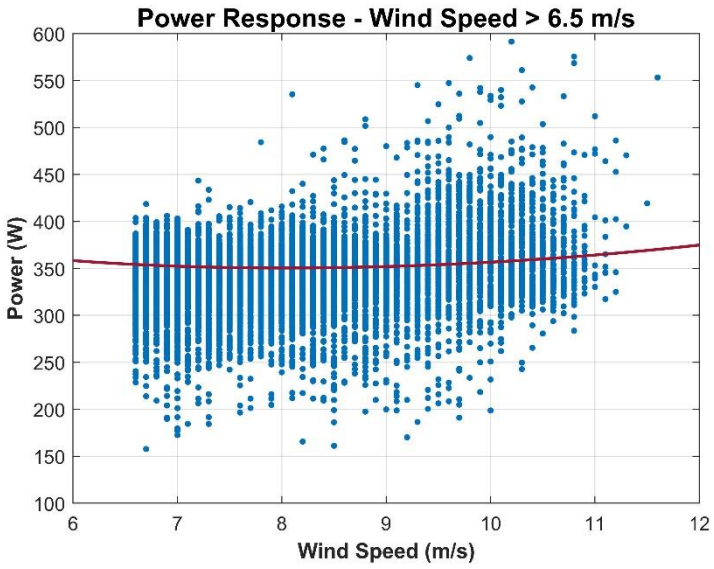

Data set	Model	No. of Data Points	R^2	RMSE *(W)*
$V_\infty > 6.5\ m/s$	$P = (437.4/V_\infty) + 0.035V_\infty^3 + 277.8$	21 545	0.489	21.00

Figure 7.2: *UAV power demand versus wind speed for a hexacopter in hovering flight for wind speeds above 6.5 m/s.*

the minimum power demand experienced by the hexacopter UAV during open field operations, as shown in Figure 7.2 and Figure 7.3.

Since the approximation for the power demand of a multirotor UAV was derived from a mathematical model that was developed based on the momentum theory for an individual rotor, the model does not cater for the effect of rotors operating in close proximity to each other, both in ideal hover conditions as well as in rotor wake interference situations brought about by the operation of tandem rotors in incident horizontal winds. It has been established by Prudden et al. [94] that rotor wake interference has an adverse effect on the thrust generation of the operating rotors. Evidently the approximation used to model the open field performance of the UAV requires further development. The study also highlights how challenging it is to realistically model a multirotor in the open field.

7.4.1.1 Wind Speed at Minimum UAV Hovering Power Demand

It has already been established that the Glauert's High speed approximation discussed in section 3.2.4.2 and upon which the power demand model was developed, is most accurate at higher wind speed ranges. It was therefore considered appropriate that for

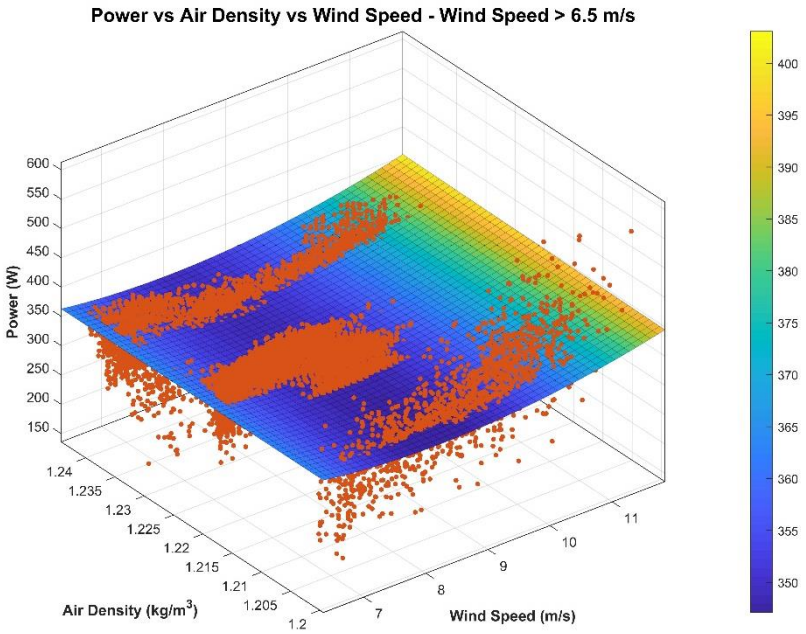

Data set	Model	No. of Data Points	R^2	RMSE *(W)*
$V_\infty > 6.5\ m/s$	$P = (1\,290/\rho V_\infty) + 0.07\rho V_\infty^3 + 143.6\ \rho$	21 545	0.472	21.35

Figure 7.3: *UAV power demand versus air density and wind speed for a hexacopter in hovering flight for wind speeds above 6.5 m/s.*

a more accurate estimate of the wind speed at which the least power demand is experienced by the hexacopter UAV, data points pertaining to wind speeds above 6.5 m/s would be used. The choice of 6.5 m/s as the low wind speed threshold ensured that a substantial number of validated data points were considered for estimating the wind speed for minimum hovering power demand. The regression analysis for the power demand model as a function of wind speed (given in Figure 7.2), was used as a basis for determining the wind speed at which the research hexacopter UAV experienced the minimum power demand under open field wind conditions. The calculated power for each data point used for the development of the regression model has an uncertainty of ± 2.68 % as established in section C.6 in Appendix C. The first derivative of the bespoke function is

$$\frac{dP}{dV_\infty} = -(437.4/V_\infty^2) + 0.105V_\infty^2 \tag{7.5}$$

Solving Eq. (7.5) when the expression is equal to zero, and therefore with minimum power consumption, yields an incident wind speed (V_∞) equal to 8.0 m/s. The resulting minimum power consumption works out to 350.4 W with an RMSE of 21 W. From

the hexacopter UAV data set it was established that the mean density of air at which the minimum hover power was achieved was 1.222 kg/m^3 (mean air density for data points collected at wind speeds of 8.0 m/s ± 0.5 m/s).

The hexacopter UAV power demand when operating in incident wind speeds below 1 m/s and at an air density of 1.222 kg/m^3 was calculated using the regression model given in Figure 6.24. The power was calculated as 385.7 W with an RMSE of 10 W. It transpires that the minimum UAV hover power demand represents a power demand reduction of 9 % when compared to the quasi-pure hover power requirements.

It is evident that the optimal wind speed for minimum power consumption by the hexacopter UAV remains unchanged when the lower wind speed threshold is varied between 5.0 m/s and 6.5 m/s. Table 7.1 presents the optimal wind speeds obtained following an analysis using the regression functions of the respective data subsets. It should also be noted that the actual minimum power consumption also remains unchanged. Furthermore, the R-squared value for the regression functions increases as the lower wind speed threshold increases.

It should be highlighted that the value for the wind speed at minimum UAV hover power demand is UAV dependent due to the different design characteristics between different UAV models. This is mainly attributed to the difference in the aerodynamic profiles of the different multirotor aircraft.

7.4.2 Multirotor UAV Power Demand Reduction

Overall, the data indicate that as the incident wind speed increases, the total power demand decreases, before starting to increase as demonstrated by the regression analyses in Figure 7.2 and Figure 7.3 on the data with a higher lower wind speed

Table 7.1: *Estimated wind speeds at minimum hover power consumption for the hexacopter UAV using data subsets with different lower wind speed thresholds.*

Lower Wind Speed Threshold *(m/s)*	No. of Data Points	R^2	RMSE *(W)*	Minimum Hover Power *(W)*	Wind Speed at Minimum Hover Power *(m/s)*
5.0	42 908	0.352	21.21	350.4	7.95
5.5	37 278	0.385	20.99	350.6	7.97
6.0	30 001	0.425	21.00	350.5	8.00
6.5	21 545	0.489	21.00	350.4	8.03

threshold. The initial decrease in power demand was also witnessed in studies by Abeywickrama et al. [77], Hwang et al. [75], and Liu et al. [79]. The subsequent increase in power demand after a relative wind speed threshold has been reached was also observed in the studies by Hwang et al. [75] and Liu et al. [79]. Although this is evidenced in the open field data, its applicability in the open field depends heavily on a number of other factors, including the aerodynamic profile which is represented mathematically by the drag coefficient, C_D, of the UAV. This highlights the importance of a reduced aerodynamic profile for longer duration deployments, even when these consist of a predominantly long hovering portion. A reduced aerodynamic profile delays the onset of the parasitic component of the power demand mathematical model, which is proportional to the cube of the incident wind speed.

Furthermore, using a larger propeller reduces the disk loading of the rotors, thereby lowering the profile drag component. UAV propellers are operated using fixed pitch propellers which utilize adjustments to the RPM in order to adjust the generated lift. Increasing propeller size results in a reduction in angular velocity, which in turn reduces profile drag. Unlike single rotor aircraft, for multirotor UAVs this approach would require a larger, consequently heavier frame, due to the need to increase the rotor centre-to-centre distance for the larger rotors to fit. Such an approach would therefore demand caution to ensure that the larger heavier frame does not offset the benefit of a lower propeller angular velocity.

8 Conclusions and Further Research

This chapter summarizes the major findings that have been identified during the course of this research. It also establishes what limitations were encountered as the research progressed and how these may form the basis for future research in this field.

The objectives of this study were outlined in section 1.4.1 and the following summarizes how these have been met.

The knowledge amassed during the initial stages of the literature review exercise was eventually utilized to design and develop two multirotor UAVs – the first having a quadcopter configuration and the second having a hexacopter configuration – both with the capabilities necessary to operate over a range of wind conditions. An ultrasonic wind sensor was integrated onto each of the UAV platforms, together with a custom developed Arduino-based data logger for logging of atmospheric and wind data measurements.

The developed multirotor UAV platforms were rigged with the necessary onboard sensors necessary for the power performance analysis. The custom designed UAVs were used to collect data in an extensive measurement campaign with the UAVs in hovering flight whilst being kept stationary with respect to the ground and at fixed pre-set altitudes above ground.

The data collected during the bespoke campaign from the ground-based LiDAR unit and the UAV-mounted wind sensor were eventually analysed to evaluate the viability of utilizing a multirotor UAV with a mounted ultrasonic wind sensor as an accurate means of wind measurement.

The collected UAV platform and parametric data were analysed in conjunction with the atmospheric and wind data measurements to analyse the effects of the operating environment on the performance and power demand of the multirotor UAV platforms in open field operating conditions. Following an in-depth analysis of the collected data, the main conclusions that may be drawn from this study are the following:

1. The wind speed measured using the ultrasonic wind sensor mounted on the hexacopter UAV demonstrated a strong correlation with the recorded LiDAR

readings, although the UAV-based readings have a positive offset of 1 m/s. (section 6.3.1)

2. The wind direction readings measured by the UAV-mounted ultrasonic wind sensor are strongly correlated to the LiDAR wind direction readings with a negative offset of 6.16° (section 6.3.2).

3. The power demand of the quadcopter UAV whilst maintaining a stable hover demonstrates a trend of a reduction in power demand with an increase in wind speed (section 6.9.2). Due to the limited wind speed range at which the quadcopter UAV was operated, it was not possible to establish the wind speed at which the quadcopter UAV achieves the minimum power demand.

4. The power demand of the hexacopter UAV required to maintain a stable hover was found to decrease as the wind speed increased (section 6.9.2) up to an incident horizontal wind speed of 8.0 m/s (section 7.4.1.1). Above this value power demand increased as the wind speed increased. This demonstrates that for the hexacopter UAV used in this study, the UAV flight endurance potentially increases as the incident horizontal wind speed increased from 0 m/s up to 8.0 m/s. Beyond this wind speed threshold the effects of parasitic drag become more pronounced and hence the power demand increases, consequently reducing the UAV's flight endurance as the wind speed continues to rise.

5. A power demand reduction of 9 % was observed for the hexacopter UAV at an incident horizontal wind speed of 8.0 m/s when compared to quasi-pure hover power requirements (section 7.4.1.1).

6. The UAV diagonal power differential increases with increasing wind speed incident along the differential diagonal axis (section 6.9.4).

The consistently strong correlation observed across all operational altitudes between the UAV-based ultrasonic wind sensor readings and LiDAR unit wind measurements demonstrates the potential for using the UAV as an instrument for wind monitoring applications at high altitudes without the need for deploying expensive instrument platforms.

The phenomenon of a decrease in power demand with increasing wind speed for relatively low wind speeds is usually attributed to the onset of translational lift [112], also witnessed in the work of Abeywickrama et al. [77] and stated by Thibbotuwawa et al. [76]. This lift is generated due to a higher mass flow rate of air passing through the rotor disks as a consequence of the relative horizontal movement of air over the rotors of the aircraft caused by the prevailing wind conditions. This effect has the potential of translating into longer UAV flight times, resulting in an increase in the UAV flight endurance. For further understanding and potentially quantifying the impact on UAV flight endurance, more extensive testing potentially under the controlled conditions of a wind tunnel is necessary.

The data analyses of the various parameters, especially those connected with the power demand of the multirotor UAVs, are characterized by relatively low R-squared values, especially for the quadcopter phase of the study. Nonetheless, the trends observed from the graphical plots generated from the collected data do indicate coherence between the experimental data and the predictions of the mathematical models that have been developed. This further confirms two aspects of studies in this field: Primarily, it highlights the challenging task of accurately modelling the conditions in the open field; Secondly it also highlights the need to carry out research in relatively controlled environments to develop improved mathematical models further and hence bridge the gap between the existing techniques for UAV performance modelling and open field conditions.

8.1 Recommendations for Further Research

Notwithstanding the increased understanding of the performance of UAVs as platforms for wind monitoring applications, the challenges encountered during this study served as a basis for the identification of potential areas for further research in the field of multirotor UAVs.

It is suggested that further studies on this matter stand to benefit from using one fully integrated and synchronized data collection system, as opposed to the use of independent logging systems which are then synchronized at the post-processing stage. Such an improved approach eliminates potential clock differences in logging instances across platforms as well as removes the possibility of drift in logging frequencies which make synchronization less accurate.

The substantial difference in logging frequencies between the UAV-based onboard wind sensor data and the ground-based LiDAR unit's wind data, together with the fluctuating logging frequency of the LiDAR wind data, proved to be an obstacle for carrying out an accurate correlation analysis between the two data sets. Future studies may benefit from the use of consistent, matched and ideally synchronized logging frequencies between the types of wind measuring instruments.

Although the findings of this project indicate that the influence of the air density on a UAV's power demand is of a lesser significance than that of other parameters, it is suggested that a detailed study be carried out to investigate further the effect of air density. Any such experimental studies should ideally be conducted in an enclosed environment, to eliminate any potential undesirable wind drafts that may mask the weaker effects of air density on UAV performance. This would undoubtedly entail the use of alternative stabilizing systems, other than a GPS unit. These could be stereo vision-based navigation [114] or the use of laser range finders [115]. This study has brought to light the necessity of a stable GPS signal for the UAV to maintain an autonomous stable hover, even when subjected to minor external disturbances.

The mathematical model developed based on the simple momentum theory of a hovering rotor needs further development to reflect the open field conditions more realistically. It is suggested that the current model be validated against measurements obtained from wind tunnel experiments under controlled conditions.

Further research may focus on the further development of such a mathematical model that may be more representative of the operations of a UAV in the open field. It is understood that the developed models may be wind speed range-specific and more accurate approximations may need to be developed for low wind speeds, intermediate wind speeds as well as high wind speeds (Glauert's approximation). The operation of the UAV across the wind speed range of 0 to 12 m/s transitions through the various approximation ranges.

Future work may be undertaken to attempt the development of a universal model that is applicable to a wider and more comprehensive range of wind speeds. One such approach may be to retain the basic power demand model and develop functions for the various coefficients of the basic power demand model as a function of wind speed and potentially, of air density.

A detailed study of UAV diagonal power differential may be developed into a complementary field that may aid in providing a better understanding of the dynamics of multirotor UAV power consumption in open field conditions. Such studies may also address the development of an accompanying mathematical model necessary to establish the nature of the relationship between power differential and wind speed.

As UAV flight endurance increases, and therefore the duration of continuous operation of the BLDC motors powering the rotors increases, the operation of such motors at a maintained, elevated temperature is inevitable. It is suggested that the impact of the BLDC motors' sustained operation at such elevated temperatures on the overall efficiency of the propulsion system and the eventual impact on the flight endurance of the UAV be investigated in detail.

9 References

[1] B. Laufer, "The Prehistory of Aviation," *Anthropological Series,* vol. 18, no. 1, pp. 1-96, 1928.

[2] L. White, "Eilmer of Malmesbury, an Eleventh Century Aviator: A Case Study of Technological Innovation, Its Context and Tradition.," *Technology and Culture,* vol. 2, no. 2, pp. 97-111, 1961.

[3] F. I. Petrescu and R. V. Petrescu, The Aviation History, Norderstedt: Books on Demand GmbH, 2012.

[4] C. D. Drummond, M. D. Harley, I. L. Turner, A. N. A. Matheen and W. C. Glamore, "UAV Applications to Coastal Engineering," in *Australasian Coasts & Ports Conference,* Auckland, 2015.

[5] B. Read, "Life-saving Drones," Royal Aeronautical Society, 21 March 2017. [Online]. Available: https://www.aerosociety.com/news/life-saving-drones/. [Accessed 15 October 2020].

[6] M. A. R. Estrada and A. Ndomab, "The uses of unmanned aerial vehicles - UAV's - (or drones) in social logistic: Natural disasters response and humanitarian relief aid," *Procedia Computer Science,* vol. 149, pp. 375-383, 2019.

[7] T. Amukele, P. M. Ness, A. A. Tobian, J. Boyd and J. Street, "Drone transportation of blood products," *Transfusion,* vol. 57, no. 3, pp. 582-588, 2017.

[8] G. Xiang, A. Hardy, M. Rajeh and L. Venuthurupalli, "Design of the life-ring drone delivery system for rip current rescue," in *2016 IEEE Systems and Information Engineering Design Symposium (SIEDS),* Charlottesville, VA, 2016.

[9] U. Papa and S. Ponte, "Preliminary Design of an Unmanned Aircraft System for Aircraft General Visual Inspection," *Electronics,* vol. 7, no. 12, p. 435, 2018.

[10] C. W. Eschmann, C.-h. Kuo, C.-M. Kuo and C. Boller, "Unmanned Aircraft Systems for Remote Building Inspection and Monitoring.," in *6th European Workshop on Structural Health Monitoring,* 2012.

[11] N. Hallermann, G. Morgenthal and V. Rodehorst, "Unmanned Aerial Systems (UAS) – Case Studies of Vision Based Monitoring of Ageing Structures," in *International Symposium,* Berlin, 2015.

[12] N. Hallermann and G. Morgenthal, "Unmanned aerial vehicles (UAV) for the assessment of existing structures," in *IABSE Symposium,* Kolkata, 2013.

[13] G. Morgenthal and N. Hallermann, "Quality Assessment of Unmanned Aerial Vehicle (UAV) Based Visual Inspection of Structures," *Advances in Structural Engineering,* vol. 17, no. 3, pp. 289-302, 2014.

[14] N. Tyutyundzhiev, K. Lovchinov, F. Martínez-Moreno, J. Leloux and L. Narvarte, "Advanced PV modules inspection using multirotor UAV," in *31st European Photovoltaic Solar Energy Conference and Exhibition*, Hamburg, 2015.

[15] P. Bellezza Quater, F. Grimaccia, S. Leva, M. Mussetta and M. Aghaei, "Light Unmanned Aerial Vehicles (UAVs) for Cooperative Inspection of PV Plants," *IEEE Journal of Photovoltaics,* vol. 4, no. 4, pp. 1107-1113, July 2014.

[16] T. Ishidaa, J. Kuriharaa, F. A. Virayb, S. B. Namucoc, E. C. Paringitb, G. J. Perezc, Y. Takahashia and J. J. Marciano Jr., "A novel approach for vegetation classification using UAV-based hyperspectral imaging," *Computers and Electronics in Agriculture,* vol. 144, pp. 80-85, 2018.

[17] "Leading Edge Technology," MHI Vestas Offshore Wind A/S, [Online]. Available: https://mhivestasoffshore.com/innovations/. [Accessed 26 November 2020].

[18] "Offshore Pioneers," Siemens Gamesa Renewable Energy, S.A., [Online]. Available: https://www.siemensgamesa.com/en-int/products-and-services/offshore. [Accessed 26 November 2020].

[19] M. Stokkeland, K. Klausen and T. A. Johansen, "Autonomous visual navigation of Unmanned Aerial Vehicle for wind turbine inspection," in *2015 International Conference on Unmanned Aircraft Systems (ICUAS)*, Denver, CO, 2015.

[20] S. G. Pierce, K. Burnham, L. McDonald, C. N. MacLeod, G. Dobie, R. Summan and D. McMahon, "Quantitative inspection of wind turbine blades using UAV deployed photogrammetry," in *9th European Workshop on Structural Health Monitoring (EWSHM 2018)*, Manchester, 2018.

[21] L. Mishnaevsky Jr., K. Branner, H. N. Petersen, J. Beauson, M. McGugan and B. F. Sørensen, "Materials for Wind Turbine Blades: An Overview," *Materials,* vol. 10, no. 11, p. 1285, 2017.

[22] "DHL's Parcelcopter: Changing Shipping Forever," 20 October 2020. [Online]. Available: https://discover.dhl.com/business/business-ethics/parcelcopter-drone-technology. [Accessed 20 October 2020].

[23] L. Josephs, "CNBC," 1 October 2019. [Online]. Available: https://www.cnbc.com/2019/10/01/ups-wins-faa-approval-for-drone-delivery-airline.html. [Accessed 30 October 2019].

[24] A. Palmer, "CNBC," 31 August 2020. [Online]. Available: https://www.cnbc.com/2020/08/31/amazon-prime-now-drone-delivery-fleet-gets-faa-approval.html. [Accessed 12 November 2020].

[25] "FedEx Newsroom," 18 October 2019. [Online]. Available: https://newsroom.fedex.com/newsroom/wing-drone-deliveries-take-flight-in-first-of-its-kind-trial-with-fedex/. [Accessed 10 November 2020].

[26] A. Chaulet, "Galaxy of drones light up Guiyang night sky," 28 May 2019. [Online]. Available: https://www.euronews.com/2019/05/28/watch-galaxy-of-drones-light-up-guiyang-night-sky. [Accessed 14 August 2020].

[27] "Stunning Singapore drone lightshow illuminates new year," 6 January 2020. [Online]. Available: https://www.inavateonthenet.net/news/article/stunning-singapore-drone-lightshow-illuminates-new-year. [Accessed 14 November 2020].

[28] "Drones light up Seoul's night sky in bid to give South Koreans a boost," 13 November 2020. [Online]. Available: https://www.euronews.com/2020/11/13/drones-light-up-seoul-s-night-sky-in-bid-to-give-south-koreans-a-boost. [Accessed 14 November 2020].

[29] "Inspections using Drones," Iberdrola, [Online]. Available: https://www.iberdrola.com/innovation/drones-wind-farms. [Accessed 25 November 2020].

[30] D. J. Willis, C. Niezrecki, D. Kuchma, E. Hines, S. R. Arwade, R. J. Barthelmie, M. DiPaola, P. J. Drane, C. J. Hansen, M. Inalpolat, J. H. Mack, A. T. Myers and M. Rotea, "Wind energy research: State-of-the-art and future research directions," *Renewable Energy,* vol. 125, pp. 133-154, 2018.

[31] "Drone solutions for Wind Turbine Inspection," Aerialtronics, [Online]. Available: https://www.aerialtronics.com/en/applications/drones-for-wind-turbine-inspection#intro. [Accessed 25 November 2020].

[32] "FT205," FT Technologies, [Online]. Available: https://fttechnologies.com/wind-sensors/lightweight/ft205/. [Accessed 14 October 2019].

[33] "TriSonica™ Mini Wind and Weather Sensor," Anemoment LLC, [Online]. Available: https://anemoment.com/features/#trisonica-mini. [Accessed 10 November 2018].

[34] "iMet-XQ2 UAV Sensor," InterMet Systems, Inc., [Online]. Available: https://www.intermetsystems.com/products/imet-xq2-uav-sensor. [Accessed 14 July 2020].

[35] P. Rudol and P. Doherty, "Human Body Detection and Geolocalization for UAV Search and Rescue Missions Using Color and Thermal Imagery," in *IEEE Aerospace Conference,* 2008.

[36] S. Watkins, M. Abdulghani, S. Prudden, M. Marino, R. Clothier, A. Fisher and A. Panta, "Using MAVs for Atmospheric Wind Measurements: Opportunities and Challenges," in *International Micro Air Vehicle Conference and Flight Competition (IMAV) 2017,* Toulouse, France, 2017.

[37] V. Kumar and N. Michael, "Opportunities and Challenges with Autonomous Micro Aerial Vehicles," *Robotics Research, Springer Tracts in Advanced Robotics,* vol. 100, pp. 41-58, 2017.

[38] H. Chen and A. Khaligh, "Hybrid energy storage system for unmanned aerial vehicle (UAV)," in *IECON 2010 - 36th Annual Conference on IEEE Industrial Electronics Society,* Glendale, AZ, 2010.

[39] R. R. Glassock, J. Hung, L. González and R. A. Walker, "Multimodal Hybrid Powerplant for Unmanned Aerial Systems (UAS) Robotics," in *ICRA 2008,* 2008.

[40] C. E. Lin and T. Supsukbaworn, "Development of Dual Power Multirotor System," *International Journal of Aerospace Engineering,* vol. 2017, 2017.

[41] J. W. Langelaan, N. Alley and J. Neidhoefer, "Wind Field Estimation for Small Unmanned Aerial Vehicles," *Journal of Guidance, Control, and Dynamics,* vol. 34, no. 4, pp. 1016-1030, 2011.

[42] S. Mayer, G. Hattenberger, P. Brisset, M. O. Jonassen and J. Reuder, "A 'No-Flow-Sensor' Wind Estimation Algorithm for Unmanned Aerial Systems," *International Journal of Micro Air Vehicles,* vol. 4, no. 1, pp. 15-30, 2012.

[43] C. A. Wolf, R. P. Hardis, S. D. Woodrum, R. S. Galan, H. S. Wichelt, M. C. Metzger, N. Bezzo, G. C. Lewin and S. F. J. de Wekker, "Wind data collection techniques on a multi-rotor platform," in *2017 Systems and Information Engineering Design Symposium (SIEDS)*, Charlottesville, VA, 2017.

[44] I. de Boisblanc, N. Dodbele, L. Kussmann, R. Mukherji, D. Chestnut, S. Phelps, G. C. Lewin and S. de Wekker, "Designing a hexacopter for the collection of atmospheric flow data," in *2014 Systems and Information Engineering Design Symposium (SIEDS)*, Charlottesville, VA, 2014.

[45] D. Etts Jr., M. Rossi, R. Nzaou, R. Zhu, G. C. Lewin and S. F. J. de Wekker, "Development of an autonomous multi-rotor copter for collecting atmospheric data near the ground," in *2015 IEEE Systems and Information Engineering Design Symposium*, Charlottesville, VA, 2015.

[46] D. W. Yeo, N. Sydney, D. A. Paley and D. Sofge, "Onboard Flow Sensing for Downwash Detection and Avoidance with a Small Quadrotor Helicopter," in *AIAA Guidance, Navigation, and Control Conference*, Kissimmee, Florida, 2015.

[47] D. W. Yeo, N. Sydney and D. A. Paley, "Onboard Flow Sensing for Rotary-Wing UAV Pitch Control in Wind," in *AIAA Guidance, Navigation, and Control Conference*, San Diego, California, 2016.

[48] M. Marino, A. Fisher, R. Clothier, S. Watkins, S. Prudden and C. S. Leung, "An Evaluation of Multi-Rotor Unmanned Aircraft as Flying Wind Sensors," *International Journal of Micro Air Vehicles,* vol. 7, no. 3, pp. 285-299, September 2015.

[49] S. Prudden, A. Fisher, A. Mohamed and S. Watkins, "A Flying Anemometer Quadrotor: Part 1," in *The International Micro Air Vehicle Conference and Competition 2016*, Beijing, 2016.

[50] S. Prudden, A. Fisher, M. Marino, A. Mohamed, S. Watkins and G. Wild, "Measuring wind with Small Unmanned Aircraft Systems," *Journal of Wind Engineering and Industrial Aerodynamics,* vol. 176, pp. 197-210, May 2018.

[51] T. Shimura, M. Inoue, H. Tsujimoto, K. Sasaki and M. Iguchi, "Estimation of Wind Vector Profile Using a Hexarotor Unmanned Aerial Vehicle and Its Application to Meteorological Observation up to 1000 m above Surface," *Journal of Atmospheric and Oceanic Technology,* vol. 35, pp. 1621-1631, 2018.

[52] R. T. Palomaki, N. T. Rose, M. van den Bossche, T. J. Sherman and S. F. J. De Wekker, "Wind Estimation in the Lower Atmosphere Using Multirotor Aircraft," *Journal of Atmospheric and Oceanic Technology,* vol. 34, no. 5, pp. 1183-1191, 2017.

[53] P. Bruschi, M. Piotto, F. Dell'Agnello, J. Ware and N. Roy, "Wind Speed and Direction Detection by Means of Solid-state Anemometers Embedded on Small Quadcopters," *Procedia Engineering,* vol. 168, pp. 802-805, 2016.

[54] F. Schiano, J. Alonso-Mora, K. Rudinz, P. Beardsley, R. Siegwart and B. Siciliano, "Towards Estimation and Correction of Wind Effects on a Quadrotor UAV," in *IMAV 2014: International Micro Air Vehicle Conference and Competition 2014,* Delft, 2014.

[55] Y. Qu, Z. Xing and Y. Zhang, "Wind estimation using the position information from a hovering quadrotor," in *2016 IEEE Chinese Guidance, Navigation and Control Conference (CGNCC),* Nanjing, 2016.

[56] Y. Song, Q.-H. Meng, B. Luo, M. Zeng, S.-G. Ma and P.-F. Qi, "A wind estimation method for quadrotors using inertial measurement units," in *2016 IEEE International Conference on Robotics and Biomimetics (ROBIO),* Qingdao, 2016.

[57] J. Gonzalez-Rocha, C. A. Woolsey, C. Sultan, S. de Wekker and N. Rose, "Measuring atmospheric winds from quadrotor motion," in *AIAA Atmospheric Flight Mechanics Conference,* Grapevine, Texas, 2017.

[58] J. Gonzalez-Rocha, C. A. Woolsey, C. Sultan and S. F. De Wekker, "Model-based Wind profiling in the Lower Atmosphere with Multirotor UAS," in *AIAA Scitech 2019 Forum,* San Diego, California, 2019.

[59] J. González-Rocha, S. F. J. De Wekker, S. D. Ross and C. A. Woolsey, "Wind Profiling in the Lower Atmosphere from Wind-Induced Perturbations to Multirotor UAS," *Sensors,* vol. 20, p. 1341, 2020.

[60] L. N. C. Sikkel, G. C. H. E. de Croon, C. De Wagter and Q. P. Chu, "A novel online model-based wind estimation approach for quadrotor micro air vehicles using low cost MEMS IMUs," in *2016 IEEE/RSJ International Conference on Intelligent Robots and Systems (IROS),* Daejeon, 2016.

[61] P. P. Neumann and M. Bartholmai, "Real-time wind estimation on a micro unmanned aerial vehicle using its inertial measurement unit," *Sensors and Actuators A: Physical,* vol. 235, pp. 300-310, 1 November 2015.

[62] J.-Y. Wang, B. Luo, M. Zeng and Q.-H. Meng, "A Wind Estimation Method with an Unmanned Rotorcraft for Environmental Monitoring Tasks," *Sensors,* vol. 18, no. 12, 2018.

[63] T. Tomić, S. K. P. Lutz, A. Mathers and S. Haddadin, "The flying anemometer: Unified estimation of wind velocity from aerodynamic power and wrenches," in *2016 IEEE/RSJ International Conference on Intelligent Robots and Systems (IROS),* Daejeon, Korea, 2016.

[64] J. Winslow, M. Benedict, V. Hrishikeshavan and I. Chopra, "Design, development, and flight testing of a high endurance micro quadrotor helicopter," *International Journal of Micro Air Vehicles,* vol. 8, no. 3, pp. 155-169, 2016.

[65] D. Lundström and P. Krus, "Testing of Atmospheric Turbulence Effects on the Performance of Micro Air Vehicles," *International Journal of Micro Air Vehicles,* vol. 4, no. 2, pp. 133-149, 2012.

[66] R. Krishnakumar, A. M. Rasheed and K. S. Kumar, "Enhanced Hover Control of Quad Tilt Frame UAV under Windy Conditions," *International Journal of Advanced Robotic Systems,* vol. 12, no. 10, 2015.

[67] M. J. Cutler, T. W. McLain, R. W. Beard and B. Capozzi, "Energy Harvesting and Mission Effectiveness for Small Unmanned Aircraft," in *Proceedings of the American Institute of Aeronautics and Astronautics*, Toronto, Canada, August 2010.

[68] A. Abdilla, A. Richards and S. Burrow, "Endurance Optimisation of Battery-Powered Rotorcraft," in *Towards Autonomous Robotic Systems*, Liverpool, 2015.

[69] T. Chang and H. Yu, "Improving Electric Powered UAVs' Endurance by Incorporating Battery Dumping Concept," *Procedia Engineering,* vol. 99, pp. 168-179, 2015.

[70] R. Citroni, F. Di Paolo and P. Livreri, "A Novel Energy Harvester for Powering Small UAVs: Performance Analysis, Model Validation and Flight Results," *Sensors,* vol. 19, no. 8, p. 1771, 2019.

[71] A. S. Prasetia, R.-J. Wai, Y.-L. Wen and Y.-K. Wang, "Mission-Based Energy Consumption Prediction of Multirotor UAV," *IEEE Access,* vol. 7, pp. 33055-33063, 2019.

[72] L. W. Traub, "Range and Endurance Estimates for Battery-Powered Aircraft," *Journal of Aircraft,* vol. 48, no. 2, pp. 703-707, 2011.

[73] M. Gatti, F. Giulietti and M. Turci, "Maximum endurance for battery-powered rotary-wing aircraft," *Aerospace Science and Technology,* vol. 45, pp. 174-179, 2015.

[74] A. Abdilla, A. Richards and S. Burrow, "Power and Endurance Modelling of Battery-Powered Rotorcraft," in *2015 IEEE/RSJ International Conference on Intelligent Robots and Systems (IROS)*, Hamburg, 2015.

[75] M.-h. Hwang, H.-R. Cha and S. Y. Jung, "Practical Endurance Estimation for Minimizing Energy Consumption of Multirotor Unmanned Aerial Vehicles," *Energies,* vol. 11, no. 9, p. 2221, 2018.

[76] A. Thibbotuwawa, P. Nielsen, B. Zbigniew and G. Bocewicz, "Energy Consumption in Unmanned Aerial Vehicles: A Review of Energy Consumption Models and Their Relation to the UAV Routing," in *Information Systems Architecture and Technology: Proceedings of 39th International Conference on Information Systems Architecture and Technology – ISAT 2018.*, 2018.

[77] H. V. Abeywickrama, B. A. Jayawickram, Y. He and E. Dutkiewicz, "Comprehensive Energy Consumption Model for Unmanned Aerial Vehicles, Based on Empirical Studies of Battery Performance," *IEEE Access,* vol. 6, pp. 58383-58394, 2018.

[78] H. V. Abeywickrama, B. A. Jayawickrama, Y. He and E. Dutkiewicz, "Empirical Power Consumption Model for UAVs," in *2018 IEEE 88th Vehicular Technology Conference (VTC-Fall),* Chicago, IL, USA, 2018.

[79] Z. Liu, R. Sengupta and A. Kurzhanskiy, "A Power Consumption Model for Multi-rotor Small Unmanned Aircraft Systems," in *International Conference on Unmanned Aircraft Systems (ICUAS),* Miami, FL, USA, 2017.

[80] D. Shi, B. Yang and Q. Quan, "Reliability Analysis of Multicopter Configurations Based on Controllability Theory," in *Proceedings of the 35th Chinese Control Conference,* Chengdu, 2016.

[81] C. Pose, J. Giribet and I. Mas, "Fault tolerance analysis of a hexarotor with reconfigurable tilted rotors," in *2020 IEEE International Conference on Robotics and Automation (ICRA),* Paris, France, 2020.

[82] C. D. Pose, F. Presenza, I. Mas and J. I. Giribet, "Trajectory Following with a MAV under rotor fault conditions," *Unmanned Systems,* vol. 8, no. 4, pp. 263-268, 2020.

[83] J. G. Leishman, Principles of Helicopter Aerodynamics, Cambridge: Cambridge University Press, 2006.

[84] S. Newman, The Foundations of Helicopter Flight, Oxford: Butterworth-Heinemann, 1994.

[85] W. Johnson, Helicopter Theory, New York: Dover Publications Inc., 1994.

[86] B. Reinhardt, "Flightsafety Australia," 8 February 2018. [Online]. Available: https://www.flightsafetyaustralia.com/2018/02/a-matter-of-time-plus-speed-distance-weight-and-heat/. [Accessed 22 August 2020].

[87] P. Giacomo, "Equation for the Determination of the Density of Moist Air (1981)," *Metrologia,* vol. 18, pp. 33-40, 1982.

[88] R. S. Davis, "Equation for the Determination of the Density of Moist Air (1981/91)," *Metrologia,* vol. 29, pp. 67-70, 1992.

[89] A. Picard, R. S. Davis, M. Gläser and K. Fujii, "Revised formula for the density of moist air (CIPM-2007)," *Metrolgia,* vol. 45, pp. 149-155, 2008.

[90] G. Mandal, A. Kumar, D. C. Sharma and H. Kumar, "Comparative Analysis of Different Air Density Equations," *Journal of Metrology Society of India,* vol. 28, no. 1, pp. 51-62, 2013.

[91] M. Hassanalian and A. Abdelkefi, "Classifications, applications, and design challenges of drones: A review," *Progress in Aerospace Sciences,* vol. 91, pp. 99-131, May 2017.

[92] "Tarot Ironman 650," Tarot Rc, [Online]. Available: https://tarot-rc.com/iron-man-650-foldable-quad-copter-frame-tl65b01-p2562432.html. [Accessed 10 December 2020].

[93] "Tarot FY680," Tarot Rc, [Online]. Available: https://tarot-rc.com/fy680-six-axis-vehicle-rack-pure-carbon-tube-version-tl68b01-p2562583.html. [Accessed 10 December 2020].

[94] S. Prudden, A. Fisher, M. Marino and S. Watkins, "An investigation into the effects rotor wake interference on quadrotor UAS," in *18th Australian Aerospace Congress*, Melbourne, 2018.

[95] K. M. Thu and A. I. Gavrilov, "Modeling and design optimization for quadcopter control system using L1 adaptive control," in *2016 IEEE 7th Annual Information Technology, Electronics and Mobile Communication Conference (IEMCON)*, Vancouver, BC, 2016.

[96] DJI, "N3 User Manual," 2017. [Online]. Available: http://dl.djicdn.com/downloads/N3/20170825/N3_User_Manual_En_v1.4.pdf. [Accessed 30 July 2018].

[97] DJI, "DJI E800 Tuned Propulsion System User Manual," 2015. [Online]. Available: http://dl.djicdn.com/downloads/e800/en/E800_User_Manual_v1.0_en.pdf. [Accessed 17 June 2018].

[98] A. Raj, "What is PWM: Pulse Width Modulation," 19 September 2018. [Online]. Available: https://circuitdigest.com/tutorial/what-is-pwm-pulse-width-modulation. [Accessed 28 November 2020].

[99] "Humidity Sensor BME280," Bosch Sensortec GmbH, [Online]. Available: https://www.bosch-sensortec.com/products/environmental-sensors/humidity-sensors-bme280/. [Accessed 17 October 2018].

[100] "ZX 300 (formerly ZephIR 300) onshore wind Lidar," Zephir Ltd. / ZX Lidars, [Online]. Available: https://www.zxlidars.com/wind-lidars/zx-300/. [Accessed 5 October 2020].

[101] C. Galdies, "The Climate of Malta: statistics, trends and analysis 1951-2010," National Statistics Office, Valletta, Malta, 2011.

[102] R. N. Farrugia and T. Sant, "Wied Rini II–A Five Year Wind Survey at Malta," *Wind Engineering,* vol. 35, no. 4, pp. 419-432, 2011.

[103] R. N. Farrugia and T. Sant, "A wind resource assessment at Aħrax Point: A node for central Mediterranean offshore wind resource evaluation," *Wind Engineering,* vol. 40, no. 5, pp. 438-446, 2016.

[104] "Operational Requirements for the use of Drones in Malta," Transport Malta - Civil Aviation Directorate, [Online]. Available: https://www.transport.gov.mt/aviation/drones-2604. [Accessed 12 December 2020].

[105] "COMMISSION DELEGATED REGULATION (EU) 2019/945 of 12 March 2019 on unmanned aircraft systems and on third-country operators of unmanned aircraft systems," *Official Journal of the European Union,* 11 June 2019.

[106] "COMMISSION IMPLEMENTING REGULATION (EU) 2019/947 of 24 May 2019 on the rules and procedures for the operation of unmanned aircraft," *Official Journal of the European Union,* 11 June 2019.

[107] TM-CAD, "Self Declaration for the Safe Operation of Drones," Transport Malta, Malta, 2018.

[108] "NIST/SEMATECH e-Handbook of Statistical Methods," [Online]. Available: https://doi.org/10.18434/M32189. [Accessed 28 June 2020].

[109] "Least-Squares Fitting," Mathworks, [Online]. Available: https://www.mathworks.com/help/curvefit/least-squares-fitting.html. [Accessed 10 June 2020].

[110] L. Scicluna, T. Sant and R. N. Farrugia, "Investigation of Wind Flow Conditions on the Flight Endurance of UAVs in Hovering Flight: A Preliminary Study.," in *Proceedings of the ASME 2019 2nd International Offshore Wind Technical Conference.*, St. Julian's, Malta, 2019.

[111] Q. Zhang, N. Cui, Y. Shang, B. Duan and C. Zhan, "An improved Peukert battery model of nonlinear capacity considering temperature effect," *IFAC PapersOnLine,* vol. 51, no. 13, pp. 665-669, 2018.

[112] US Federal Aviation Administration, "Helicopter Flying Handbook," [Online]. Available: https://www.faa.gov/regulations_policies/handbooks_manuals/aviation/helicopter_flying_handbook/. [Accessed 30 March 2020].

[113] M. Harris and E. Burin des Roziers, Guidelines for Siting of ZephIR and Comparison against a Meteorological Mast, Zephir Ltd., June 2014.

[114] K. Schmid, P. Lutz, T. Tomić, E. Mair and H. Hirschmüller, "Autonomous Vision-based Micro Air Vehicle for Indoor and Outdoor Navigation," *Journal of Field Robotics,* vol. 31, no. 4, p. 537–570, 2014.

[115] Y. Song, B. Xian, Y. Zhang, X. Jiang and X. Zhang, "Towards autonomous control of quadrotor unmanned aerial vehicles in a GPS-denied urban area via laser ranger finder," *Optik,* vol. 126, no. 23, pp. 3877-3882, 2015.

Appendix A Data Collection Flights

The following tables list the respective date, time, altitude and geographic location for each data collection flight. The Geomagnetic Declination applicable on the date when the respective data collection flight was executed is also provided.

A.1 Quadcopter UAV Flights

Location : 35.985 96° N, 14.335 14° E – Ċirkewwa Open Field

Altitude : 80 m above ZephIR LiDAR Measurement Reference

Table A.1: *Details of quadcopter UAV open field flights – 80 m altitude.*

Flight	Date	UAV Arming Time	Declination *(°)*
FL008	6 April 2019	09:24:13 GMT	3.222 45
FL009	6 April 2019	09:52:22 GMT	3.222 45
FL010	10 April 2019	09:38:05 GMT	3.223 71
FL011	10 April 2019	10:15:11 GMT	3.223 71
FL012	10 April 2019	10:42:02 GMT	3.223 71

A.2 Hexacopter UAV Flights

Location : 35.985 96° N, 14.335 14° E – Ċirkewwa Open Field

Altitude : 40 m above ZephIR LiDAR Measurement Reference

Table A.2: *Details of hexacopter UAV open field flights – 40 m altitude.*

Flight	Date	UAV Arming Time	Declination *(°)*
FL027	3 December 2019	13:38:49 GMT	3.298 03
FL031	27 December 2019	08:51:42 GMT	3.305 56
FL035	2 January 2020	10:56:28 GMT	3.307 43
FL038	7 January 2020	12:35:24 GMT	3.308 98
FL041	9 January 2020	09:18:53 GMT	3.309 60
FL044	10 January 2020	09:15:54 GMT	3.309 91
FL047	16 January 2020	12:55:39 GMT	3.311 77
FL072	21 February 2020	09:03:38 GMT	3.322 90
FL078	6 March 2020	08:26:19 GMT	3.327 23
FL083	12 March 2020	12:58:50 GMT	3.329 09

Location : 35.985 96° N, 14.335 14° E – Ċirkewwa Open Field

Altitude : 60 m above ZephIR LiDAR Measurement Reference

Table A.3: *Details of hexacopter UAV open field flights – 60 m altitude.*

Flight	Date	UAV Arming Time	Declination *(°)*
FL033	27 December 2019	09:24:25 GMT	3.305 56
FL036	2 January 2020	11:14:29 GMT	3.307 43
FL039	7 January 2020	12:53:59 GMT	3.308 98
FL042	9 January 2020	09:34:32 GMT	3.309 60
FL045	10 January 2020	09:31:10 GMT	3.309 91
FL048	16 January 2020	13:11:56 GMT	3.311 77
FL050	17 January 2020	09:12:17 GMT	3.312 07
FL071	14 February 2020	08:51:52 GMT	3.320 74
FL073	21 February 2020	09:19:07 GMT	3.322 90
FL082	12 March 2020	12:38:34 GMT	3.329 09

Location : 35.985 96° N, 14.335 14° E – Ċirkewwa Open Field

Altitude : 80 m above ZephIR LiDAR Measurement Reference

Table A.4: *Details of hexacopter UAV open field flights – 80 m altitude.*

Flight	Date	UAV Arming Time	Declination *(°)*
FL030	7 December 2019	09:36:32 GMT	3.299 29
FL034	27 December 2019	10:06:14 GMT	3.305 56
FL037	2 January 2020	11:31:47 GMT	3.307 43
FL043	9 January 2020	09:51:16 GMT	3.309 60
FL053	23 January 2020	12:28:14 GMT	3.313 93
FL054	23 January 2020	12:44:57 GMT	3.313 93
FL056	30 January 2020	11:48:35 GMT	3.316 10
FL058	30 January 2020	13:49:44 GMT	3.316 10
FL060	31 January 2020	08:40:31 GMT	3.316 41
FL081	12 March 2020	12:21:26 GMT	3.329 09

Location : 35.985 96° N, 14.335 14° E – Ċirkewwa Open Field

Altitude : 100 m above ZephIR LiDAR Measurement Reference

Table A.5: *Details of hexacopter UAV open field flights – 100 m altitude.*

Flight	Date	UAV Arming Time	Declination *(°)*
FL049	16 January 2020	13:31:16 GMT	3.311 77
FL055	23 January 2020	13:05:08 GMT	3.313 93
FL059	30 January 2020	14:22:56 GMT	3.316 10
FL061	31 January 2020	09:01:08 GMT	3.316 41
FL062	31 January 2020	09:21:58 GMT	3.316 41
FL063	7 February 2020	12:03:36 GMT	3.318 57
FL064	7 February 2020	12:26:37 GMT	3.318 57
FL068	13 February 2020	08:34:11 GMT	3.320 43
FL070	14 February 2020	08:35:20 GMT	3.320 74
FL074	21 February 2020	09:39:12 GMT	3.322 90

Location : 35.876 53° N, 14.475 49° E – Qormi Sheltered Site

Altitude : 5 m above the ground

Table A.6: *Details of hexacopter UAV sheltered flights – 5 m altitude.*

Flight	Date	UAV Arming Time	Declination *(°)*
FL087	02 June 2020	07:43:46 GMT	3.366 81
FL088	02 June 2020	08:03:29 GMT	3.366 81
FL089	02 June 2020	08:24:08 GMT	3.366 81

Location : 35.877 74° N, 14.470 01° E – Qormi Tied Down

Altitude : Rotors at 1.2 m above ground

Table A.7: *Details of hexacopter UAV tied down tests.*

Flight	Date	UAV Arming Time	Declination *(°)*
TD011	10 July 2020	06:14:19 GMT	3.377 80
TD012	10 July 2020	06:23:18 GMT	3.377 80
TD013	10 July 2020	06:35:45 GMT	3.377 80
TD014	10 July 2020	06:54:19 GMT	3.377 80
TD015	10 July 2020	07:12:47 GMT	3.377 80

Appendix B UAV Pre-flight Checklist

Weather Conditions	
- Wind Intensity	
- Precipitation Risk	

Fasteners Tightness	
- Propulsion Arms to Multirotor Centre Hub – 2 screws x 6 arms	
- Motor mount safety pipe Clamps – 2 screws x 6 pipe clamps	
- Motor Mounts – 6 screws x 6 arms	
- Motor Screws – 4 screws x 6 motors	
- Anemometer screws – 6 screws	
- Sensors mount plate screws – 8 screws	
- Landing Gear Attachments – 4 screws	
- Battery Mount – Straps and 4 Butterfly Nuts	

Power Distribution Cabling	
- Power Harness to Current Sensors – 6 connectors	
- Power Harness to Flight Controller – 1 connector	
- Power Harness to Wind Sensor – 1 connector	
- Current Sensors to ESCs – 2 connectors x 6 sensors	
- ESCs to Motors – 6 connectors x 6 motors	

Signal Cabling	
- ESC signal cables to Flight Controller – 6 cables	
- Radio Receiver SBUS cable to Flight Controller – 2 connectors x 1 cable	
- Smart Port sensor cabling – 2 connectors x 14 cables	
CENTRE OF GRAVITY position check	
POWER UP Radio Transmitter and CONNECT BATTERY to Power harness	

LED Status Indicators Check	
- GNSS antenna – Flashing Green	
- Flight Controller – Flashing Green	
- Radio Receiver – Solid Green	
- ESCs – 2 Flashing Green (UAV Front Pair), 4 Flashing Red	
- Smart Port sensors (6 x Current Sensors, 1 x Variometer, 1 x GPS receiver and 6 x RPM sensors) – 14 Flashing Red	
POWER UP iMet-XQ2 sensor	
CONNECT BATTERY to Arduino Data logger system	
- Arduino GPS Reception – Flashing Red	
- iMet-XQ2 sensor GPS reception – Solid Blue	
CALIBRATE UAV's Flight Controller compass	
SET Flight Controller HOME position	
- UAV Flight Controller Overall status indicator – Flashing Green	
CHECK that AIRSPACE overhead is CLEAR	
ARM UAV	
CHECK that direction of rotation of rotors is correct	

GO for LIFT-OFF

Appendix C Error Analysis

The research carried out involved the measurement of several parameters. Invariably the measured readings incorporate measurement uncertainties predominantly due to the limitations of the measurement devices used. Due to the nature of the study the possibility of repeating readings to minimize such uncertainties was very limited as the experimental measurements were related to open field conditions, which inherently cannot be reproduced.

In this section the measurement uncertainty is estimated using error propagation techniques to establish the potential error for the calculated parameters based on the respective functions used for the bespoke computations.

C.1 Air Density

Air density is a parameter that was calculated as a function of the measured air temperature, atmospheric pressure and relative humidity, using the equation given hereunder:

$$\rho = \frac{3.48488 \cdot p - (8.0837 + 737.4 \times 10^{-3} t + 975.25 \times 10^{-6} t^3) \times RH}{(273.15 + t) \times 10^3} \quad \text{(A.1)}$$

The uncertainty in the calculated value of the density of air is calculated as a function of the partial derivatives of the variables on which the density of air is dependent.

$$\frac{\partial \rho}{\partial p} = \frac{3.48488}{(273.15 + t) \times 10^3} \quad \text{(A.2)}$$

$$\frac{\partial \rho}{\partial RH} = -\frac{(8.0837 + 737.4 \times 10^{-3} t + 975.25 \times 10^{-6} t^3)}{(273.15 + t) \times 10^3} \quad \text{(A.3)}$$

$$\frac{\partial \rho}{\partial t} = \frac{-3484.88 \cdot p - (193337.11 + 799.1686 t^2 + 1.9505 t^3) \times RH}{\left((273.15 + t) \times 10^3\right)^2} \quad \text{(A.4)}$$

The uncertainty in the calculated density of air may therefore be expressed as

$$\frac{\delta \rho}{|\rho|} = \sqrt{\left(\frac{\partial \rho}{\partial p} \delta p\right)^2 + \left(\frac{\partial \rho}{\partial RH} \delta RH\right)^2 + \left(\frac{\partial \rho}{\partial t} \delta t\right)^2} \quad \text{(A.5)}$$

The iMet-XQ2 environmental sensor manufacturer declared the accuracy of the measured parameters as ± 150 Pa for the pressure readings, ± 5 % for the relative

humidity readings and ± 0.3 °C for the temperature readings. Based on the declared parameter accuracies and the typical experimental values, of 102 500 Pa, 50 % and 15 °C for the pressure, relative humidity and temperature readings respectively, the uncertainty in the values of calculated density of air is calculated as

$$\frac{\delta\rho}{|\rho|} = \sqrt{(1.209 \times 10^{-5} \cdot 150)^2 + (-7.786 \times 10^{-5} \cdot 5)^2 + (-0.00453 \cdot 0.3)^2} \quad \text{(A.6)}$$

$$\frac{\delta\rho}{|\rho|} = \pm\, 0.230\ \% \quad \text{(A.7)}$$

C.2 Wind Speed Average

During the correlation study of the wind speed between the UAV based sensor and LiDAR measurement readings it was necessary to calculate the average of the UAV based wind speed measurements taken during the time lapse between each two wind speed readings of the LiDAR wind speed measurements. This leads to an adjustment in the error of the averaged UAV based readings.

$$\delta\overline{V_\infty} = \frac{\sqrt{\left(\delta V_{\infty_1}\right)^2 + \left(\delta V_{\infty_2}\right)^2 + \left(\delta V_{\infty_3}\right)^2 + \cdots + \left(\delta V_{\infty_N}\right)^2}}{N} \quad \text{(A.8)}$$

$$\delta\overline{V_\infty} = \frac{\delta V_\infty}{\sqrt{N}} \quad \text{(A.9)}$$

The FT205EV wind speed sensor accuracy is declared as $\pm$ 0.3 m/s, and the number of averaged readings was typically 120. It transpires that the uncertainty in the average of wind speed readings works out at

$$\delta\overline{V_\infty} = \frac{0.3}{\sqrt{120}} = \pm\, 0.0274\ m/s \quad \text{(A.10)}$$

C.3 Wind Direction Average

Similar to the wind speed correlation, the average wind direction needed to be calculated from UAV based readings logged at a higher frequency.

$$\delta\bar{\theta} = \frac{\sqrt{(\delta\theta_1)^2 + (\delta\theta_2)^2 + (\delta\theta_3)^2 + \cdots + (\delta\theta_N)^2}}{N} \quad \text{(A.11)}$$

$$\delta\bar{\theta} = \frac{\delta\theta}{\sqrt{N}} \tag{A.12}$$

The specification sheet of the FT205EV wind sensor declares the wind direction accuracy as 4° RMS, and the number of averaged readings was typically 120. The estimated uncertainty in the average of wind direction readings works out at

$$\delta\bar{\theta} = \frac{4}{\sqrt{120}} = 0.365^{o}\ \text{RMS} \tag{A.13}$$

C.4 Propulsion Arm Power Consumption

The power consumption of each individual propulsion rotor assembly was calculated by multiplying the current drawn with the battery power pack voltage. The uncertainty for the power consumption may therefore be expressed as

$$\frac{\delta P}{|P|} = \sqrt{\left(\frac{\delta I_{ARM}}{I_{ARM}}\right)^2 + \left(\frac{\delta V_{bat}}{V_{bat}}\right)^2} \tag{A.14}$$

The manufacturer of the current sensors used to measure the current drawn by each propulsion motor stated that the accuracy of the current measurements as $\pm$ 0.1 A, whilst that of the voltage measurements is estimated at $\pm$ 0.5 V. Using the typical values for the individual arm current drawn and the battery pack voltage given below, the uncertainty in the calculation of power consumption follows:

Typical Arm Current Draw during Hover : 2.5 A

Typical Battery Pack Voltage : 23.5 V

$$\frac{\delta P}{|P|} = \sqrt{\left(\frac{0.1}{2.5}\right)^2 + \left(\frac{0.5}{23.5}\right)^2} = \pm\ 4.53\ \% \tag{A.15}$$

C.5 Diagonal Power Differential

The diagonal power differential is the difference in power demand between diagonally opposite propulsion arms. It is therefore calculated as the difference between the calculated power consumption values of the respective propulsion arms. The uncertainty for each propulsion arm power calculation has already been established as $\pm$ 4.53 %. Therefore, the uncertainty in the diagonal power differential is be given by

$$\delta P_{Diff} = \sqrt{(\delta P_1)^2 + (\delta P_2)^2} \tag{A.16}$$

Considering that the typical propulsion arm power consumption was approximately 60 W, the uncertainty in the calculated Diagonal Power differential typically works out at $\pm$ 3.844 W.

C.6 Total Power Consumption

The computation of the power consumption of the UAV was achieved by adding up the individual currents of the UAV propulsion motors to obtain the total current drawn. The total current drawn was then subsequently multiplied with the battery pack voltage. The uncertainty for the sum of the total current drawn is given by

$$\delta I_{TOT} = \sqrt{(\delta I_1)^2 + (\delta I_2)^2 + (\delta I_3)^2 + \cdots + (\delta I_N)^2} \tag{A.17}$$

$$\delta I_{TOT} = \delta I \sqrt{N} \tag{A.18}$$

Based on the uncertainty of the total current drawn, the uncertainty in the calculated total power demand is estimated by

$$\frac{\delta P}{|P|} = \sqrt{\left(\frac{\delta I_{TOT}}{I_{TOT}}\right)^2 + \left(\frac{\delta V_{bat}}{V_{bat}}\right)^2} \tag{A.19}$$

Using the typical values for the Total Current drawn and the battery pack voltage given below, the uncertainty in the calculation of power demand follows:

Typical Total Current Draw : 15 A

Typical Battery Pack Voltage : 23.5 V

$$\delta I_{TOT} = 0.1\sqrt{6} = \pm 0.245\ A \tag{A.20}$$

$$\frac{\delta P}{|P|} = \sqrt{\left(\frac{0.245}{15}\right)^2 + \left(\frac{0.5}{23.5}\right)^2} = \pm 2.68\ \% \tag{A.21}$$